Advancements in sub-Kelvin Paramagnetic Refrigeration:
The Development of a Sub-Kelvin Active Magnetic Regenerative Refrigeration System
An Improved Thermodynamic Model of the Chrome-Cesium Alum

By

Chloe M. Gunderson

A dissertation submitted in partial fulfillment of

the requirements for the degree of

Doctor of Philosophy

Mechanical Engineering

at the

UNIVERSITY OF WISCONSIN-MADISON

2023

Date of final oral examination: 4/27/2023

The dissertation is approved by the following members of the Preliminary Oral Committee:
Franklin K. Miller, Professor, Mechanical Engineering
Gregory F. Nellis, Professor, Mechanical Engineering
John M. Pfotenhauer, Professor, Mechanical Engineering
Dakotah Thompson, Assistant Professor, Mechanical Engineering
Peter Timbie, Professor, Physics

Approved:

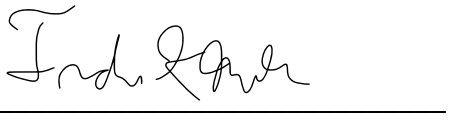

Professor Franklin K. Miller
Department of Mechanical Engineering
University of Wisconsin – Madison

Professor Greg F. Nellis
Department of Mechanical Engineering
University of Wisconsin – Madison

Advancements in sub-Kelvin Paramagnetic Refrigeration:
The Development of a Sub-Kelvin Active Magnetic Regenerative Refrigeration System
An Improved Thermodynamic Model of the Chrome-Cesium Alum

Research completed under the supervision of
Professors Franklin K. Miller and Greg F. Nellis at the University of Wisconsin – Madison

Abstract

Continuous and efficient sub-Kelvin cooling for uninterrupted operation of cutting-edge detectors, both in space and on the ground, is critical for top performance in many NASA missions. Paramagnetic refrigeration systems such as the Continuous Adiabatic Demagnetization Refrigerator (CADR) are presently used to achieve these ultra-low temperatures, but current solutions are far from ideal. More specifically, the CADR does not scale easily to provide cooling to larger surface areas or multiple detectors. Furthermore, the refrigerants used in the lowest stages of the CADR, like the Chrome-Cesium Alum (CCA), show a significant reduction in cooling capacity below the isolated paramagnetic spin model for temperatures below 100 mK.

This work addresses the aforementioned weaknesses through two distinct efforts: the development of a sub-Kelvin Active Magnetic Regenerative Refrigerator (AMRR) and an improved thermodynamic model of CCA. The AMRR developed in this work can provide distributed sub-K cooling via circulation of a ^{3}He-^{4}He mixture. With future optimization, this system could replace the upper stages of CADRs on spaceflight missions, resulting in a lower mass and scalable cooling system. Relevant to the lower CADR stages, the improved thermodynamic model of CCA has made clear the importance of Zero Field Splitting on the properties of the refrigerant. These findings are relevant to other types of refrigerants as well and could aid in material selection and design of future CADR systems.

Acknowledgments

This research would not have been possible without the endless support and guidance from my mentors, peers, and family. I am so thankful to have been surrounded by so many incredible people throughout my graduate studies.

I have so many things to thank Franklin Miller for: encouraging me to apply to grad school and to the fellowship program, teaching me about cryogenics, helping me with my lab skills, and mentoring me both professionally and personally, just to name a few. Without him, I would not be where I am today. He provided me with so many opportunities to grow as a scientist and engineer, connected me with numerous other mentors and research projects, and encouraged me to challenge myself beyond what I thought I was capable of. I am so fortunate to have had him as a mentor.

I want to thank Greg Nellis for his incredible mentorship as well, and for keeping this research on track. Between anticipating future needs, breaking down the project into appropriate step sizes, approaching problems with a new perspective, and acknowledging progress, he helped identify, outline, and enable the path forward. I have learned so much from him and am grateful to have had his guidance throughout my time at UW.

Thank you to my other committee members – John Pfotenhauer, Dakotah Thompson, and Peter Timbie – for their guidance and input during this process, and additional insights related to my research methods and results.

A big thank you to Amir Jahromi for his extraordinary mentorship. I am honored to have been entrusted with continuing his research and will be forever grateful for his generous guidance. His advice has been invaluable, and I have learned and continue to learn so much from him.

Thank you to Warren Holmes for teaching me how to think like a physicist. My work with him has helped me gain confidence in branching into new areas of research and developing and exploring my own theories. He encouraged me to pursue these ideas and continue to challenge myself and provided the guidance I needed to do so.

I'd also like to thank the NASA Goddard cryogenics branch and NASA JPL group for their support. It has been a privilege to work with such brilliant and supportive scientists, from whom I've learned so much about a wide range of cryogenic technologies and experimental methods.

A huge thank you to Josh Truchon, who was with me every step of the way. From machining integral system components, to helping me run experiments, to making sure the lab stayed organized, he played a key role in the success of this research. I am so thankful to have been able to work with someone who was just as much a mentor to me as I was to him, and I'm excited to see what's next for him.

I'd also like to thank the UW-Madison machine shop group, specifically Jay Bowe, Jeff Rappe, and Mike Hughes, for their patience and advice on my many challenging designs. They always found a way to make my visions come to life and helped build my confidence and skills as a machinist.

Allen Yingling also deserves a special thanks for his tremendous generosity and support. He did everything possible to help me, whether that be lending me various components I needed or training me on using the liquid cryogens in our lab. In more ways than one, this research absolutely would not have been possible without him.

A thank you also to the SEL lab and students for always being willing to help with research questions and making the lab an inclusive, supportive, and enjoyable place to work. Special thank yous to Jennifer and Uzo for their mentorship; many of my lab skills and much of my lab knowledge came from them. Another special thank you to my undergraduate researchers, Lucy and Payton, for their dedication and support of this project as well.

Finally, I want to thank my family and friends for always listening to me talk about my research (despite not always knowing what I am talking about) and supporting me endlessly throughout this program. I could not have done it without them.

Funding

I would like to thank NASA for funding this research through a NASA Space Technology Graduate Research Opportunity, and for providing me with invaluable opportunities throughout all four years of support.

Table of Contents

List of Figures

List of Tables

Nomenclature

B	Magnetic field strength (T)
$B_{axis,inside}$	Field along center axis solenoid (T)
B_{eff}	Effective applied filed (T)
b	Material background field (0.481 T for GGG)
C	Specific heat capacity (J/kg-K)
c	Specific heat capacity (J/mol-K)
D	Crystalline splitting factor
E	Energy (J) or (eV)
E_F	Fermi Energy
E_{max}	Maximum incident photon energy
G	Material dependent property
G(T)	Conductance (W/K)
g	Landé g-factor
H	Applied Magnetic field
h	Enthalpy
I	Current (A)
I	Nuclear spin value
J	Electronic angular momentum (7/2 for GGG)
k	Boltzmann's constant
k_{off}	Thermal conductivity in the off-state
k_{on}	Thermal conductivity in the on-state
L_{coil}	Length of coil (m)
M	Number of temporal nodes
N	Number of spatial nodes
$\dot{N}$	Molar flow rate (mol/s)
NbTi	Nioobium-Titanium
n	Number of atoms
n	Total turns per unit length (1/m)
p	Pressure
$\dot{Q}$	Heat transfer rate (W)

q_c	Critical heat flux (W/m^2)
R	Resistance (Ω)
R_{coil}	Effective coil radius (m)
S	Electronic spin value
S	Entropy (J/K)
S_e	Entropy of conduction electrons (J/K)
S_l	Lattice entropy (J/K)
S_m	Magnetic entropy (J/K)
T	Temperature (K)
T_{ad}	Adiabatic temperature (K)
T_b	Base temperatures (K)
T_λ	Lambda temperature
T_N	Neél temperature (0.38 K for GGG)
t	Time (s)
U	Internal energy (J)
V	Voltage
x	^{3}He molar concentration
Z	Partition function

Greek symbols

I, II	Phase numbers
Δ	Change in value
β	Bohr magneton
ζ	Switching ratio figure of merit
κ_T	Isothermal compressibility
λ	Lambda point (2.17 K)
μ	Chemical potential
μ_0	Permeability of free space
μ_B	Bohr magneton
ρ	Density

Superscripts

0	Initial state
3	Helium-3
4	Helium-4

Subscripts

0	Initial state
1	Final state
3	Property of ^{3}He
4	Property of ^{4}He
CHX_in	Inlet to CHX
Al	Aluminum
i	Spatial node index
j	Temporal node index
n	Normal state
max	Maximum value reached
Pb	Lead
s	Superfluid state
V	Vanadium

Acronyms

AFM	Antiferromagnetic
AMR	Active Magnetic Regenerator
AMRR	Active Magnetic Regenerative Refrigerator
ADR	Adiabatic Demagnetization Refrigerator
CADR	Continuous Adiabatic Demagnetization Refrigerator
CCA	Chrome-Cesium Alum
CHX	Cold Heat Exchanger
CPA	Chrome-Potassium Alum
CV	Control Volume
CX	Cernox

DR	Dilution Refrigerator
FAA	Ferric-Ammonium Alum
FD	Flow Demagnetization
FM	Flow Magnetization
GEP	Galaxy Evolution Probe
GGG	Gadolinium Gallium Garnet
GLF	Gadolinium Lithium Fluoride
HHX	Hot Heat Exchanger
JPL	Jet Propulsion Laboratory
KID	Kinetic Inductance Detector
LHS	Left Hand Side
NFD	No Flow Demagnetization
NFM	No Flow Magnetization
NTC	Negative Temperature Coefficient
OST	Origins Space Telescope
PICO	Probe of Inflation and Cosmic Origins
QCD	Quantum Capacitance Detector
RHS	Right hand side
SEL	Solar Energy Lab
SMP	Superfluid Magnetic Pump
STJ	Superconducting Tunnel Junctions
TES	Transition Edge Sensors
TFN	Thermodynamic Fluctuation Noise
TX	Taxonomy
ZFS	Zero Field Splitting

1. Paramagnetic Refrigeration Introduction and Motivation

1.1 Introduction

Cryogenic operating temperatures are vital to the success of numerous space science instruments used in far-IR, millimeter, and X-ray astrophysics missions. More specifically, proposed missions expected to launch in 2035 require detector cooling at 50-100 mK, with auxiliary cooling at or below 1K for various other devices such as telescope and optical components [1]. The Origins Space Telescope (OST), Probe of Inflation and Cosmic Origins (PICO), and Galaxy Evolution Probe (GEP) need detector cooling at 35- 50 mK, 100 mK, and 100 mK, respectively, with 1 K auxiliary cooling [1]. Adiabatic demagnetization of paramagnetic salt pills can be used to achieve ultra-low temperatures and provide the necessary sub-Kelvin cryogenic refrigeration for these missions [2, 3]. Existing cooling systems are far from ideal, however, and significant advances in these refrigeration technologies would have widespread impact as many high sensitivity detector applications in current and future NASA missions rely on these cryogenic temperatures for operation.

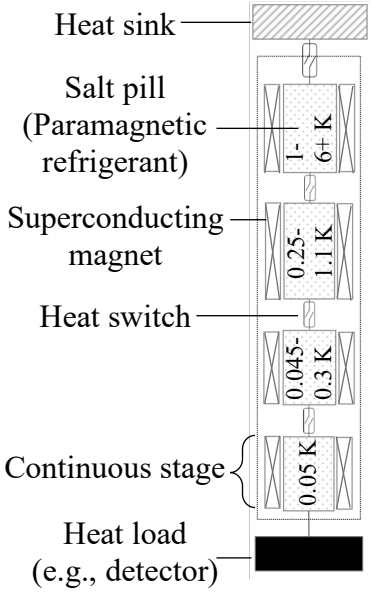

Figure 1. A diagram of the CADR system.

The Continuous Adiabatic Demagnetization Refrigerator (CADR) is presently the standard solution for reaching operating temperatures below 100 mK. As shown in Figure 1, the CADR shuttles heat through a series of paramagnetic stages from a detector to a heat sink at 1-6+ K [4]. A thorough understanding of the magnetic heat capacity of these paramagnetic salts approaching zero Kelvin is vital to designing stages that meet future, very-low temperature instrument cooling requirements. Current thermodynamic models are in poor agreement with experimental

data below a few hundred millikelvin because the magnetic behavior is complicated by energy splitting due to the crystalline electric field, spin-orbit coupling, dipole-dipole interactions, and exchange interactions [5, 6]. Additionally, substantial amounts of magnetic shielding are needed to protect the instrument due to the proximity between the detector and magnets. This distance cannot easily be extended because of the requirement for highly conductive thermal links between the stages within the system and to the detector. Heat switches throughout the remainder of the system introduce additional inefficiencies, locations for possible failure, and weight into the system, an important consideration for space technology. Consequently, scaling these systems to increase cooling power or provide cooling to multiple detectors would substantially decrease the efficiency and increase the weight as the heavier components such as the shielding and thermal links would need to scale similarly. Increased efficiency and reliability related to cooling these state-of-the-art low-noise detectors and optics would enable scientists to improve the resolution and range of data collection both in space and on the ground, allowing NASA to continue to push the bounds of human knowledge through discovery.

The development of a sub-Kelvin Active Magnetic Regenerative Refrigerator (AMRR) is discussed in this work. This novel AMRR can provide continuous and distributed sub-Kelvin cooling to multiple lower CADR stages via circulation of a ^{3}He-^{4}He mixture using a non-moving Superfluid Magnetic Pump (SMP). This approach addresses many of the challenges described above, and the improvements are made clear in Figure 2. Figure 2 (left) shows four separate CADRs cooling numerous detectors and/or large surfaces, demonstrating the onerous process associated with scaling up the current cooling option. As shown in Figure 2 (right), substituting the AMRR for the upper CADR stages results in a no-vibration, low mass, and scalable sub-Kelvin cooling solution for space instrumentation. Furthermore, the distributed cooling makes

refrigeration of larger areas or unique detector geometries possible, a significant advantage over other cryogenic refrigeration options.

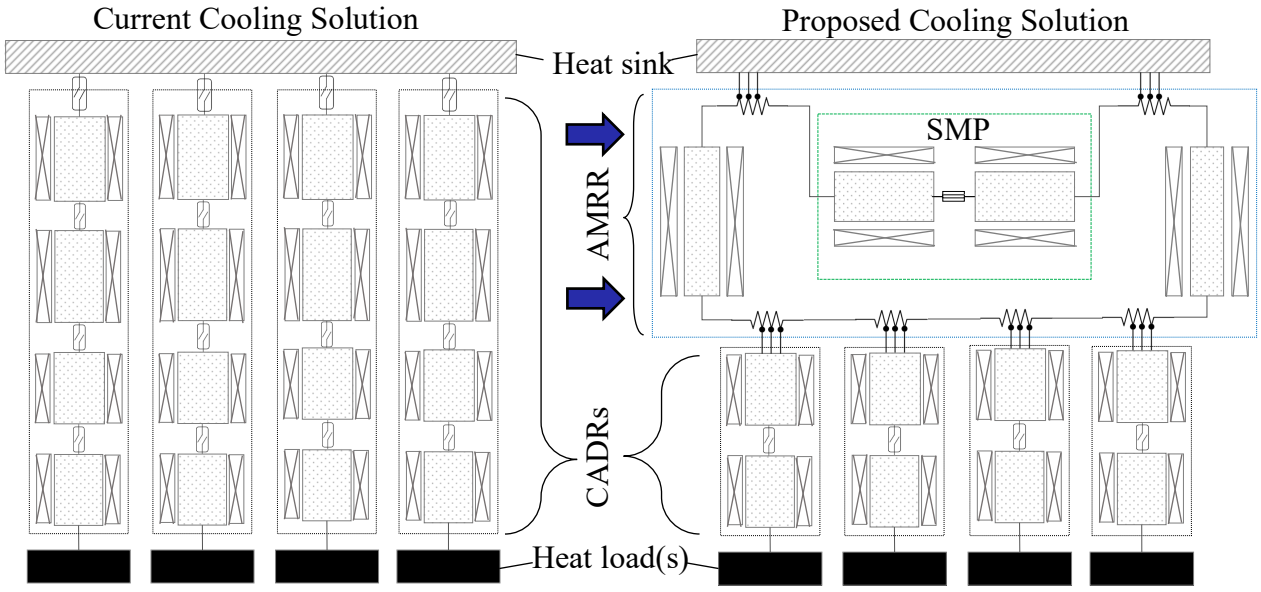

Figure 2. This diagram highlights the advantages of replacing higher temperature CADR stages (left) with the AMRR system (right) for more efficient cooling of multiple detectors or large surface areas.

Chrome-Cesium Alum (CCA), Ferric-Ammonium Alum (FAA), and Chrome-Potassium Alum (CPA) are currently used in the two lowest temperature stages of the CADR in order to achieve operating temperatures as low as 35 mK; all of these material exhibit heat capacity anomalies when approaching zero Kelvin. This work focuses particularly on the cooling capacity of CCA, which shows a specific heat capacity that is significantly below the isolated paramagnetic spin model for temperatures below 100 mK, likely due in part to omitted low temperature effects. This reduction can be seen in Figure 3 which shows specific heat capacity as a function of magnetic field at several different temperatures. Details about the heat capacity measurements shown in Figure 3 are provided in Section 3.1.2. To better understand the low-temperature behavior and the effect of various interactions on heat capacity, a magnetic spin Hamiltonian model is used to predict the paramagnetic properties of CCA. The validity of this model is investigated by comparison with experimental results from two separate salt pills with data taken between 50 mK

and 300 mK. Though the modeling effort described in this work focuses on CCA, similar energy splittings are seen in CPA and FAA. An improved understanding of the thermodynamic behavior of CCA would therefore enable enhanced modeling of other alums and provide useful insights for material selection for the two coldest stages.

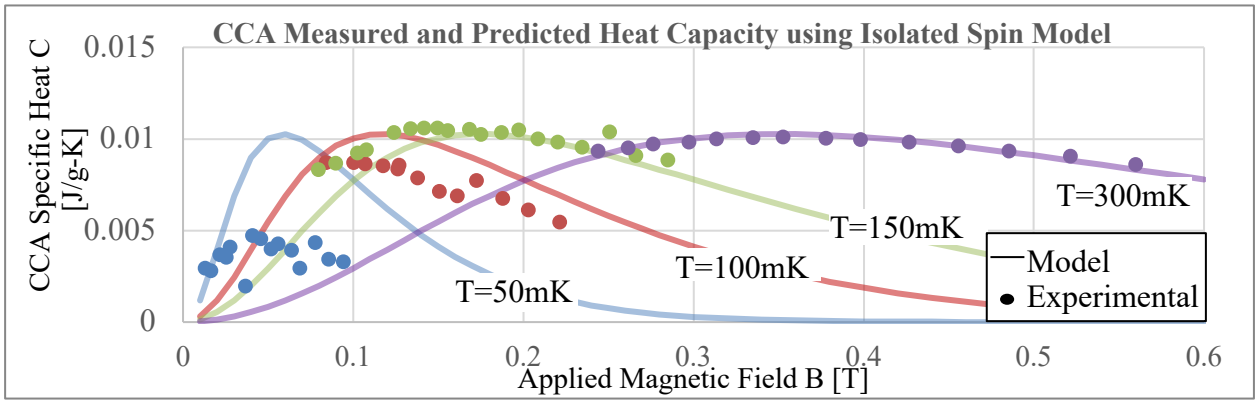

Figure 3. The measured and predicted CCA heat capacity using the isolated paramagnetic spin model.

These separate research efforts target distinct areas of weakness in the current cooling solution, providing improvement on a holistic scale. The scopes of the two main objectives are highlighted in Figure 4 and include:

- the replacement of the upper CADR stages with the AMRR system for scalable cooling, and
- the development of an improved thermodynamic model to aid in design and material selection of the lower CADR stages.

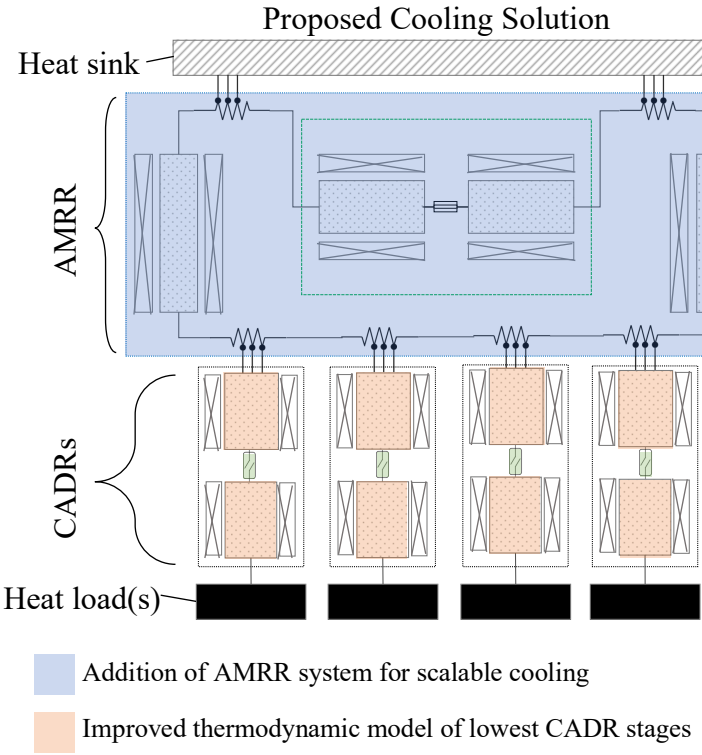

Figure 4. Scope of the three distinct research efforts described in this work.

1.2 Motivation for Active Sub-Kelvin Cooling of Space Science Instrumentation

Cryogenic detectors have higher sensitivity and better energy resolution than alternative sensors, making them an attractive option for space exploration and essential for observing low energy photons in the near- or far-IR, X-ray, and submillimeter ranges [7]. Using low energy photon detection, NASA has been able to find terrestrial planets, examine cosmic background radiation, confirm the existence of interstellar dust, and map gravitational fields, among other

Table 1. Characteristics of different photon detectors from [7]. Near and sub-Kelvin detectors are highlighted.

Detector type:	Spectral range		Temperature range (K)		Dissipation range (W)		Detector size (pixel and array)	
	Range	Wavelength (m)	Min	Max	Min	Max	Pixel (μm)	Array (n x n)
Ge crystal	Gamma / hard X-ray	$\lambda < 1E\text{-}11$ m	50	100	0	0	10000	<10
CCD	X-ray / Vis	$1E\text{-}10 < \lambda < 1E\text{-}6$ m	150-200	300	0.1	20	10-30	10^6
STJs	X-ray–UV-Vis-NIR	$1E\text{-}10 < \lambda < 5E\text{-}6$ m	0.01	1	10^{-9}	10^{-6}	20-50	$<10^3$
μ-Calorimeters	X-ray	$1E\text{-}10 < \lambda < 1E\text{-}7$ m	0.05	0.3	10^{-12}	10^{-11}	100	<100
TESs	X-ray-UV-Vis-NIR	$1E\text{-}10 < \lambda < 1E\text{-}6$ m	0.05	0.3	10^{-11}	10^{-9}	100	<100
Photo-conductors-NIR	NIR	$5E\text{-}7 < \lambda < 5E\text{-}6$ m	30	100	0.01	0.02	30-50	10^6
Photo-conductors-MIR	MIR	$5E\text{-}6 < \lambda < 5E\text{-}5$ m	2	20	0.01	0.02	50-100	$<10^4$
Photo-conductors-FIR	FIR	$5E\text{-}5 < \lambda < 1E\text{-}4$ m	1	2	0.001	0.003	50-100	$<10^3$
Sub-mm bolometers	Sub-mm	$1E\text{-}4 < \lambda < 1E\text{-}3$ m	0.1	0.3	10^{-9}	10^{-8}	100-500	$<10^2$

things [7]. Since NASA's first cryogenic missions in the early 1980s, increasingly complex space detectors have necessitated continuous advancements in cryogenic solutions [8]. Multiple current astrophysics photon detectors, such as Superconducting Tunnel Junctions (STJs), microcalorimeters, Transition Edge Sensors (TESs), Kinetic Inductance Detectors (KIDs) [9], and Quantum Capacitance Detectors (QCDs) [10], are dependent on mechanical coolers to achieve reliable and long-term cooling at the near Kelvin or sub-Kelvin operation temperatures; characteristics of many of these detector are summarized in Table 1 [7]. Alternative refrigeration options fail to meet these requirements. Radiative cooling can only achieve cooling powers around 2 W at 50 K and stored-cryogen coolers can only reach near Kelvin temperatures with limited mission duration due to boil off [8].

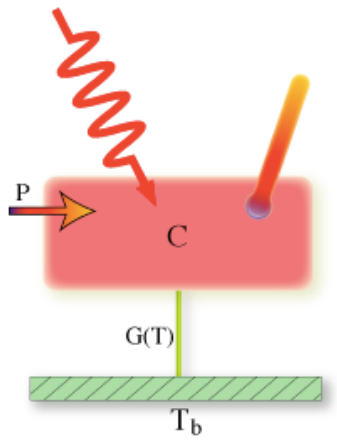

Figure 5. A visual depiction of a microcalorimeter [11].

These types of detectors rely on unique material properties existing only at cryogenic temperatures. For example, a microcalorimeter in its most elementary form consists of an absorber with C heat capacity, a thermometer, and a weak link to a cryogenically refrigerated heat sink at temperature T_b, as shown in Figure 5 [11]. The link has a conductance G, which is a function of its temperature. When an incident photon hits the absorber, the energy deposit causes the temperature of the absorber to spike, which is detected by the thermometer and converted into an energy reading. The temperature then drops back to the baseline temperature as the heat is rejected through the thermal link to the heat sink. The change in temperature from an incident photon is inversely proportional to the heat capacity of the absorber, which quickly drops off as the temperature approaches 0 K. Thus cryogenic temperatures are required as lower-temperature absorbers have larger changes in

temperature for a given photon and therefore are able to detect low energy levels with high resolution.

Similar to and sometimes in combination with microcalorimeters, TESs are thermometers that rely on cryogenic refrigeration, as they operate at the transition temperature of the superconducting films which comprise them [11]. These films are tuned to transition at the desired detector operating temperature, amplifying the change in resistance for small changes in temperature, as shown in Figure 6 [11]. Higher resistance changes for a given temperature change due to an incident photon increases the resolution of the energy reading even further.

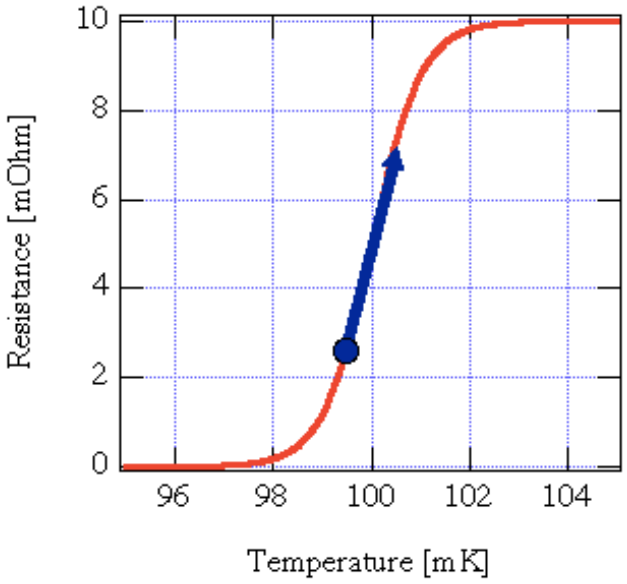

Figure 6. TES resistance as a function of temperature [11].

Perhaps more compelling, though, is the reduction of noise at cryogenic temperatures, which allows for more accurate measurements and smaller resolvable energy levels. The major sources of noise include thermodynamic fluctuation noise (TFN), thermometer Johnson or Nyquist noise, load resistor Johnson noise, amplifier noise, and photon background noise [12]. TFN appears in microcalorimeters and bolometers as energy exchanges between the absorber and the heat sink, resulting in energy fluctuations in the absorber [12]. The total error associated with this type of noise is proportional to the temperature. Likewise, thermometer and load resistor Johnson noises are temperature dependent and capture the thermal noise associated with thermal agitation of electrons within the thermometry circuit. These major thermal noise sources can be limited through cryogenic refrigeration. It is possible to reduce the remaining sources of noise to negligible levels through careful engineering of the amplifiers and optical components [12]. Figure 7 shows the effects of removing thermal sources of noise from a microcalorimeter, with c) showing the signal, TFN, and Johnson noise, b) removing the Johnson noise, and a) removing TFN [12].

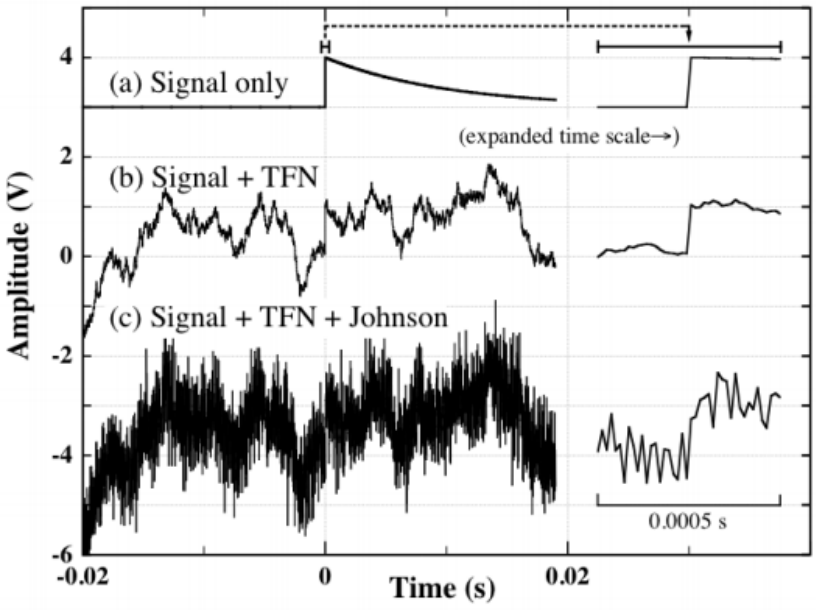

Figure 7. The signal from an ideal microcalorimeter with different types of noise [12].

Eliminating thermal noise sources increases the signal to noise ratio, ultimately enabling the detection of finer energy differences between photons and enhancing the resolution of the detector, as demonstrated in Figure 8. This graph is based on the theoretical energy resolution of a microcalorimeter, which is given as $\Delta E \cong 2.35\sqrt{4kTE_{max}}$ where k is Boltzmann's constant, T is temperature, and E_{max} is the maximum incident photon energy [11]. For an incident photon with 10 keV of energy, lowering the operating temperature from 2 K to 0.5 K halves the minimum resolvable energy.

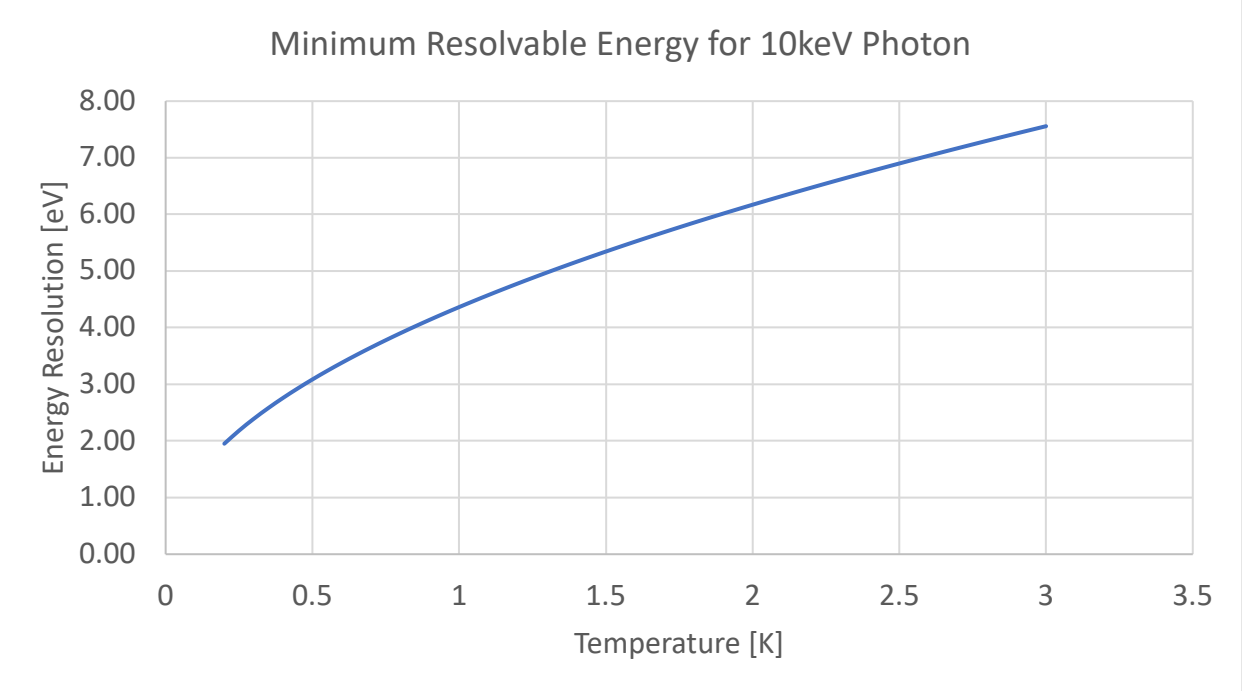

Figure 8. Theoretical minimum energy resolution in a microcalorimeter as a function of temperature for an incident photon with 10keV of energy.

1.3 Cryogenic Refrigeration Requirements for Current and Future NASA Missions

Numerous current and future NASA astrophysics missions have needs for cryogenic refrigeration as they are based on observations that are made possible with these low energy space instruments. LiteBird, ATHENA, and SPICA are all current or near-future missions which require

sub-Kelvin cooling of their detectors [1]. Among SPICA's several instruments, SAFARI and BLISS both require sub-Kelvin cooling as they use TES bolometers for far-IR spectroscopy [13]. Chains of cryogenic systems must be creatively coupled to minimize mass and provide the required cooling power at each instrument's operating temperature [13]. Efforts to advance cryogenic refrigeration systems will have a widespread impact on these missions as improved solutions could allow for increased efficiency, reduced mass, and, in some cases, continuous data collection. These capabilities will expand NASA's current limits for exploration and discovery, creating new possibilities for future missions. As previously noted, numerous proposed missions expected to launch in 2035 include multiple detectors requiring millikelvin cooling with near Kelvin auxiliary cooling, could directly benefit from current research efforts [1].

It is evident that cryogenic refrigeration does and will continue to play a critical role in many NASA astrophysics missions. Therefore, to inform the direction of future research NASA has created guidelines outlining the requirements for advancements in this area. Two separate Taxonomies (TXs) in NASA's 2020 technology taxonomy discuss cryogenic solutions: Sensors and Instruments (TX08) and Thermal Management Systems (TX14).

Within the Sensors and Instruments category is the Cryogenic/Thermal subcategory (TX08.1.6). This category encompasses cryogenic systems with both passive and active components used to cool space instrumentation, the requirements being that they have "low power, low mass, and low exported vibration during operation" [14]. Adiabatic Demagnetization Refrigerators (ADRs), heat pipes, and cryocoolers are all example technologies in this category [14].

Under Thermal Management Systems is Thermal Conditioning for Sensors, Instruments, and High Efficiency Electric Motors (TX14.1.3), which includes "cost-effective, high-efficiency,

low-weight/vibration cryocoolers and advanced sub-Kelvin cooling technology" [14]. These cryogenic solutions include technologies like magnetic refrigeration, solid cryogens heat sinks, and liquid hydrogen spacecraft Dewars [14]. From this taxonomy, we can deduce that high efficiency and low mass, vibrations, and power are stringent requirements for future space instrument refrigeration solutions.

1.4 Current Near Kelvin and Sub-Kelvin Refrigeration Solutions

Sub-K coolers represent the coldest stage of cryogenic refrigeration chains, where the integration of numerous cooling solutions results in a wide-ranging system able to lift heat from the instrument to highest temperature heat sink (e.g. deep space). A variety of cryogenic space cooling systems, which are either presently used or under development, are shown in Figure 9, with their cooling powers given at typical operating temperatures [8] [15].

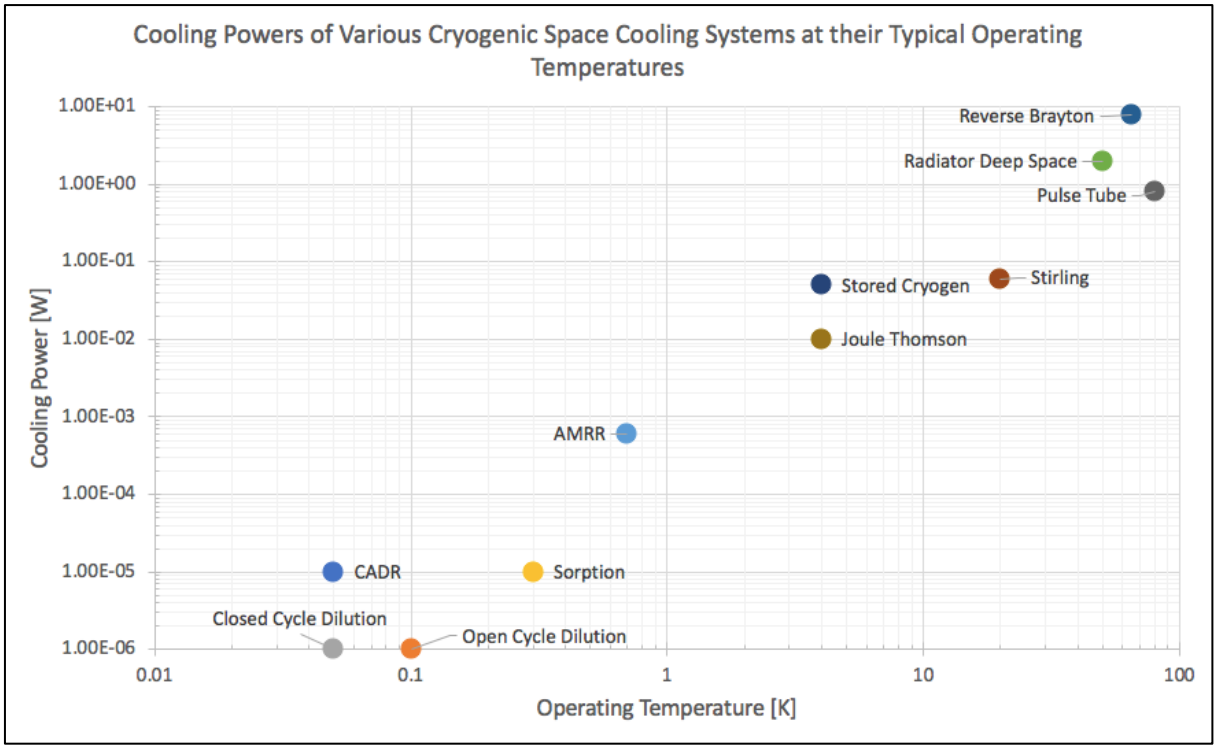

Figure 9. Cooling powers for cryogenic refrigeration solutions at a typical operating temperature. Data taken from [8] [15].

Early IR missions, such as IRAS, COBE, ISO, and Spitzer, relied solely on ^{4}He cryostats to achieve cryogenic operating temperatures between 1.4-3 K during flight [8]. It wasn't until the development of the ADR that the first sub-Kelvin mission, ASTRO-E, became possible. ASTRO-E was unfortunately lost during launch in 2005 but was designed to operate at 65 mK [8]. Subsequent development of new technologies has made achieving sub-Kelvin temperatures through different types of coolers feasible. In addition to the ADR/CADR, sorption coolers and open cycle dilution refrigerators have been used to reach these ultra-low operating temperatures in space. One primary focus of this research is on the development of a novel sub-Kelvin system, which addresses some of the challenges faced by these other solutions. Though the AMRR can operate as a stand-alone system for cooling to hundreds of millikelvin, coupling it to lower CADR stages enables scalable cooling to tens of millikelvin. To better understand the unique advantages of the AMRR and hybrid AMRR/CADR systems, it is important to provide a brief overview of the existing and near-future sub-Kelvin technologies for context.

1.4.1 Continuous Adiabatic Demagnetization Refrigerator (CADR)

Continuous Adiabatic Demagnetization Refrigerators (CADRs) are unique in that they can provide high power, long-term cooling at operating temperatures on the order of tens of millikelvin [8]. They conform to many of NASA's requirements for space coolers, offering highly efficient, nonvibrational, and continuous cooling [4]. Because of this, CADRs are presently the most widely used sub-K system in space applications.

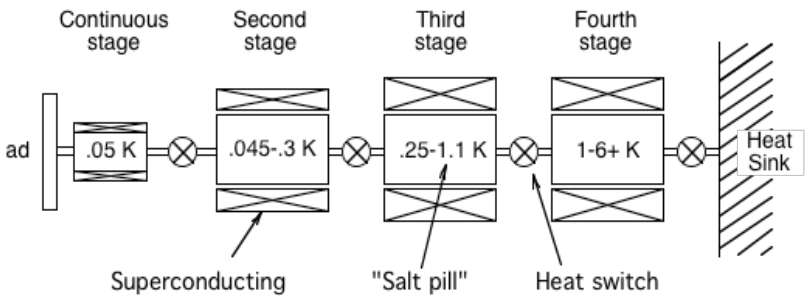

Figure 10. A diagram of the CADR system [4].

Figure 10 shows a diagram of the CADR, with the instrument on the left and the heat sink on the right [4]. As previously explained, each stage is composed of a salt pill surrounded by a superconducting magnet and magnetic shielding. The salt pills contain a paramagnetic refrigerant; therefore, the temperature of the pill is linked to the applied magnetic field due to the magnetocaloric effect. Cycling through magnetizing and demagnetizing each stage, the system can lift heat from the instrument to the heat sink, allowing heat to move between stages via passive and active heat switches. The CADR can maintain a constant operating temperature for the instrument and can provide 5-10μW of cooling at 50 mK [16] [4].

One of the disadvantages of this system is the large magnetic fields that are required. The requirement for a highly conductive thermal link between the system and detector limits the allowable distance between the two, placing the instrument in close proximity to the magnetic fields and necessitating substantial amounts of magnetic shielding, which adds significant mass. The heat switches are also an additional source of not only mass, but inefficiency and possible locations for failure within the system.

Former missions using this technology have used single-shot ADRs, which consist of just one of the previously described stages between the instrument and the heat sink. Though a single stage does not have as much weight as the complete CADR, it is not as robust an option because it cannot span as large of a temperature range or reach as low of temperatures, it has lower cooling power, and it cannot allow for continuous detector operation due to necessary periodic recycling of the single stage [4]. Due to these factors, NASA has been working to develop spaceflight CADRs for future missions [4].

1.4.2 Dilution Cooler

Dilution refrigerators (DRs) are also presently used for refrigeration of space instrumentation. An open-cycle adaptation of a ground DR was developed for the Planck mission and provided 0.1μW of continuous cooling at 0.1 K [17]. In this DR, gaseous ^{3}He and ^{4}He flowed from their respective reservoirs and were condensed into a mixing chamber where an endothermic mixing process dropped the temperature of the fluid and provided cooling at the cold tip. The resulting mixture was then pumped into space, limiting the cooler lifetime. For the Planck mission, 2.5 years of cooling was required, equating to 10,560 Liters at Normal Temperature and Pressure (LNTP) of ^{3}He and 31,680 LNTP of ^{4}He [17]. In upcoming missions, especially those with longer lifetimes, the open-cycle DR is impractical as the amount of required cryogens becomes too great.

Efforts are underway to create a gravity-insensitive closed-cycle DR, which would have a longer lifetime, reach temperatures in the tens of millikelvin, and offer cooling powers that are closer to the very high cooling powers (on the order of 100 μW at 0.1 K) that are normally associated with ground DRs [8] [17]. Though further development of this technology will address many of the weaknesses in the current DR solution, this is not a fully demonstrated option at this time.

1.4.3 ^{3}He/^{4}He Sorption Pump Cooler

^{3}He/^{4}He sorption pump coolers are also an option for sub-Kelvin space refrigeration. These closed-cycle coolers are simple in operation, requiring no moving parts and offering high efficiency duty cycles [8]. FIR instruments on the *Herschel* Space Observatory relied on a ^{3}He sorption cooler to reach operating temperatures of 285 mK for large arrays of bolometers [18]. An exploded representation of the space-flight system is shown in Figure 11. An exploded view of the ^{3}He sorption cooler used on *Herschel* . [18].

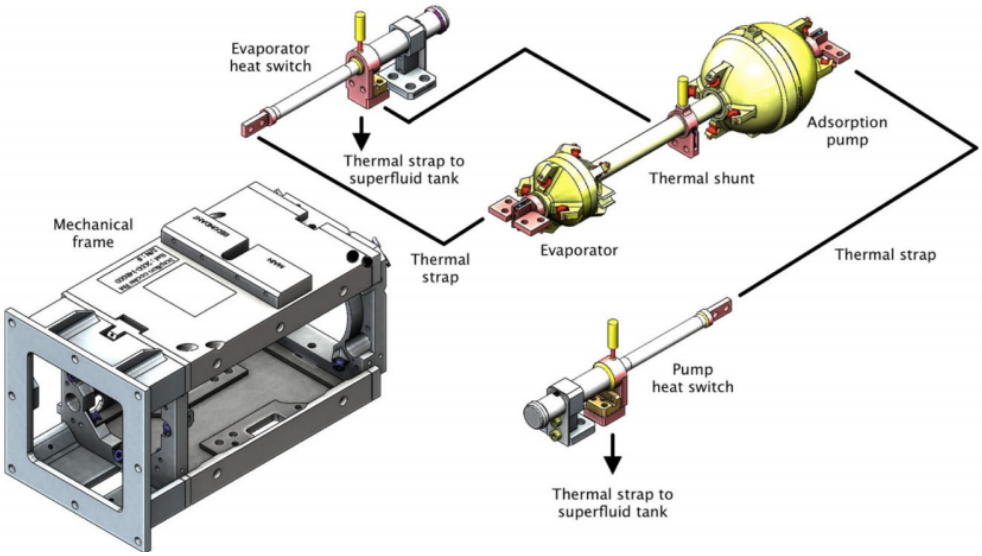

Figure 11. An exploded view of the ^{3}He sorption cooler used on *Herschel* [18].

In this system, liquid ^{3}He is trapped within a porous alumina sponge in the evaporator and provides cooling to the detector as it evaporates [18]. Activated charcoal in the sorption pump is used to drive this evaporation through adsorption, effectively pumping on the helium vapor and lowering the saturated vapor pressure and temperature [19]. The relationship between saturated vapor pressure and temperature for ^{3}He and ^{4}He is shown in Figure 12 [19].

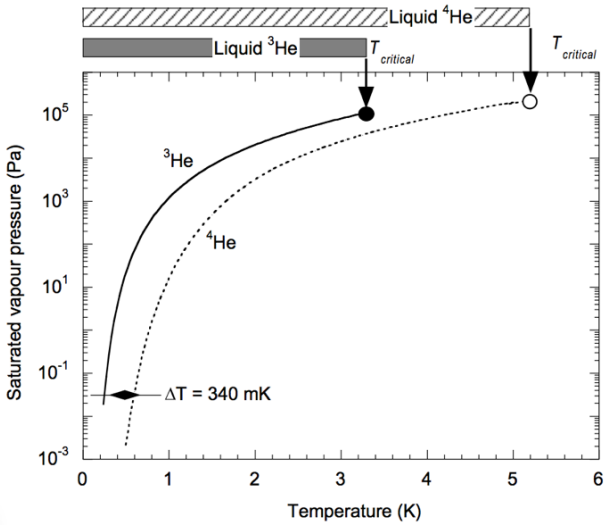

Figure 12. Saturated vapor pressure of helium 3 and helium 4 [19].

Physical adsorption occurs when a gas particle collides with a surface at a low enough temperature that the incident particle loses a substantial amount of kinetic energy and remains attached to the surface through weak intermolecular forces [20]. Porous materials maximize sorption capacity due to their large surface areas (typically 1200 $m^{2.}/g$ for activated charcoal) [19] [20]. The adsorption process continues until all of the helium is gaseous [18]. At this point, the recycling procedure begins. The recycling procedure is controlled by heaters and gas-gap heat switches throughout the system [18]. The sorption pump is heated to desorb the trapped helium gas, eventually outgassing and condensing the helium back on the evaporator which is thermally linked via a heat switch to a liquid ^{4}He bath at around 1.7 K [18]. To finish the procedure, the heat switch to the evaporator is opened, and the heat switch between the pump and the liquid bath is closed [18]. Cooling the charcoal causes it to begin pumping again, lowering the ^{3}He pressure and dropping the temperature of the liquid ^{3}He to the 300 mK operating temperature [18]. The *Herschel* system could provide a hold time between 60 and 73 hours, with recycling times of 2-3 hours [18].

Though the duty cycle in this system is long, the periodic operation necessarily prevents continuous cooling. Additionally, similar to the ADR, the reliance on heat switches and heaters results in inefficiency in the system as these components produce substantial waste heat – for the 10 μW detector load on *Herschel*, the total heat rejected to the liquid bath was 23 mW [16]. The adsorption of helium also limits the system. To maintain low pressure during pumping, the helium layer on the charcoal surfaces should not exceed a few monolayers of gas; beyond this point the adsorption effect becomes negligible and the helium pressure and temperature will increase [20]. An additional consequence of the reliance on adsorption is that the operating temperature is limited to about 300 mK for ^{3}He and 1 K for ^{4}He - temperatures corresponding to the achievable saturated vapor pressure in the system using a sorption pump. The adsorption process also necessitates

desorbing the gas from the charcoal getter each cycle, requiring heating to tens of Kelvin and contributing to the previously mentioned waste heat [16].

1.4.4 Comparison of Current and Proposed Solutions

There are only a small number of systems able to reach near and sub-Kelvin temperatures, and there are enough difference between these solutions in categories of importance to require careful consideration when designing for specific missions. For many near-future spaceflight missions requiring millikelvin operating temperatures, the CADR is the system of choice as it outperforms alternative solutions in many of these categories. Though one of the CADR's strengths is its ability to span large temperature ranges, replacing the higher temperature stages with an alternative cooler could be particularly advantageous for efficient scalable cooling. The solution made possible by this research capitalizes on the distinctive advantages of both the CADR and AMRR systems by replacing upper CADR stages with the lower mass and scalable AMRR system while keeping the lower CADR stages to reach temperatures in the tens of millikelvin range.

The AMRR system developed in this research will provide cooling down to approximately 900 mK with a predicted cooling power of 600μW-1mW, though future iterations with different types of magnetic refrigerant could reduce the cold end temperature. This system has no vibrations, is low mass, and has high efficiency and therefore has many of the characteristics laid out in the NASA guidelines. A specific advantage of this system is that the cooling is provided via circulation of a ^{3}He-^{4}He mixture, so integration with instrumentation or lower temperature stages is flexible and does not have the same limitations as solid-state systems. For example, when the AMRR is coupled directly to detectors, they can be located at a greater distance from the magnetic cooler than in existing systems because the flow of the ^{3}He-^{4}He mixture eliminates the need for the

traditional copper heat bus that is otherwise required. Lengthening this distance will reduce the magnetic shielding needed, therefore lowering the weight of the refrigeration system as a whole. The circulation of ^{3}He-^{4}He will also allow sub-K cooling to be distributed within instruments or over larger areas, allowing larger detectors, multiple detectors, and/or lower CADR stages to be cooled with one magnetic cooler. The use of an active magnetic regenerator also eliminates the need for the heat switches between the upper stages in of the CADRs, further decreasing the weight of the overall system. A substantial improvement over current cryogenic systems, this technology will reduce the mass of the refrigeration unit while maintaining reliable cooling of sensitive instruments and therefore represents an important step forward in cryogenic refrigeration technology. Additional weaknesses in the CADR are addressed through the development of an improved thermodynamic model to aid in material selection and system design.

1.5 Research Objectives

This research aims to improve sub-Kelvin cryogenic refrigeration of astrophysics detectors through two distinct efforts:

- the design and construction of a complete proof-of-concept AMRR system to enable low-mass, high efficiency, and scalable sub-Kelvin cooling, and
- the development and validation of a more accurate thermodynamic model of CCA for the lowest temperature CADR stages.

To develop the novel AMRR system, we created a simple numerical model for use as a design tool to size the components required by the system. Many of the SMP components were already available so the bulk of the design/fabrication work was focused on the remaining AMRR components. The regenerator canisters were fabricated, packed with crushed GGG to the desired porosity, and sealed. Two superconducting magnets were wound for the regenerators, and a pre-existing but unused replacement magnet was installed into the SMP. The resulting AMRR system was filled with the ^{3}He-^{4}He mixture to allow experimental testing. LabView was then used to cycle the system and collect data for system characterization.

Our improved thermodynamic model of CCA used a complete magnetic spin Hamiltonian to predict the paramagnetic properties of the salt. We examined the effects of hyperfine and zero field splitting on the predicted heat and refrigeration capacities and validated the model with data sets from two different CCA salt pills.

2. Background of Paramagnetic Refrigeration and the AMRR system

2.1 Introduction

To achieve sub-Kelvin refrigeration, cooling systems leverage a few key physical characteristics of paramagnetic refrigerants and/or liquid helium. Specifically, paramagnetic salts such as CCA have a coupling between the temperature of the material and an applied magnetic field, allowing for an induced temperature change as a response to changing magnetic fields. The AMRR system also takes advantage of unique ^{3}He-^{4}He mixture properties that result in temperature driven flow. A basic introduction to the foundational intricacies of paramagnetic refrigeration and near Kelvin helium mixtures is critical for understanding the cryogenic systems discussed in this work.

2.2 Low Temperature Helium Properties

Helium is the only element that is liquid in the temperature range of operation for the AMRR, making it the sole option for the system working fluid. In fact, helium will only freeze at pressures that are more than 20 times atmospheric pressure and has normal boiling points of 4.2 K for ^{4}He and 3.2 K for ^{3}He – both well above the maximum temperature seen within the AMRR cooler [21]. At low temperatures, each of the two stable helium isotopes exhibits unique properties. As a mixture, their respective properties, as well as interaction effects between the individual isotopes, contribute to the overall usefulness of the ^{3}He-^{4}He fluid in the AMRR system.

2.2.1 Pure ^{3}He

As noted above, helium is unique in that it is the only element that does not solidify unless it is subjected to high pressures. This is due to both its strong zero-point fluctuations and its weak intermolecular forces [22]. Zero-point motion refers to the oscillations of quantum particles about their average position and grows stronger in particles with small atomic mass like helium [22].

Having two protons but only one neutron, ^{3}He has a total nuclear spin of ½ and obeys Fermi-Dirac statistics, resulting in its unusual low temperature properties [22]. The Pauli exclusion principle states that only one particle can fill each available state in Fermi systems, and at absolute zero temperature the energy of the highest occupied state is known as the Fermi Energy E_F of the system [22]. This energy can be used to find the Fermi temperature, below which the gas is degenerate (i.e., all states are filled). For ^{3}He, this temperature is around 1 K [22].

At temperatures on the order of 1 mK and below, two different superfluid phases – where the ^{3}He atoms become frictionless – are observed [22]. The formation of these superfluid states is analogous to that of superconductive states in metals; the ^{3}He fermions form Cooper pairs which condense into the same quantum state, though in ^{3}He the spins align parallel with each other (S=1) [22]. In the presence of a magnetic field, a third stable phase emerges between A and the normal Fermi liquid, and the A phase becomes stable down to zero pressure [22]. However, this occurs significantly below the operating temperature of the AMRR and is out of the scope of this research. In the temperature range of the AMRR system, ^{3}He is a normal liquid as shown in the phase diagram in Figure 13 [22].

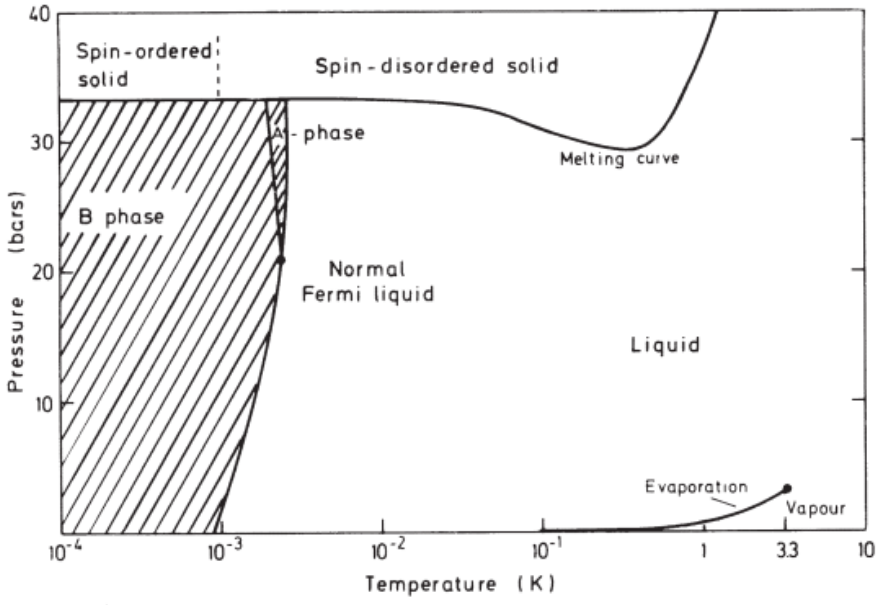

Figure 13. ^{3}He Phase diagram [22].

2.2.2 Pure ^{4}He

The more common isotope, ^{4}He, is the element traditionally referred to as "helium" and contains two protons and two neutrons [22]. It is the heavier of the two isotopes, and has a higher binding energy than ^{3}He, resulting in its higher boiling point [23]. Unlike ^{3}He, the ^{4}He atom has zero spin and obeys Bose-Einstein statistics [23]. Below the condensation temperature T_C, an increasing fraction of bosons occupies the lowest energy state, a phenomenon known as Bose-Einstein condensation [23]. In ^{4}He, this transition point is referred to as the λ-transition and occurs around 2.17 K, where normal liquid ^{4}He begins transitioning into a superfluid [23]. The ^{4}He phases at temperatures above and below this transition have markedly different properties and are commonly called He I and He II, respectively. These ^{4}He phases are shown in Figure 14 [22].

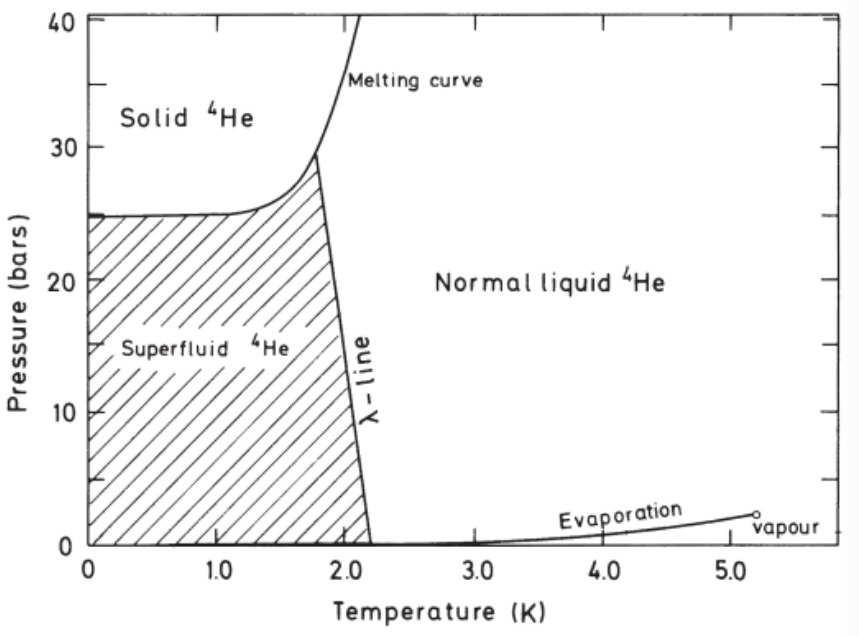

Figure 14. ^{4}He phase diagram [22].

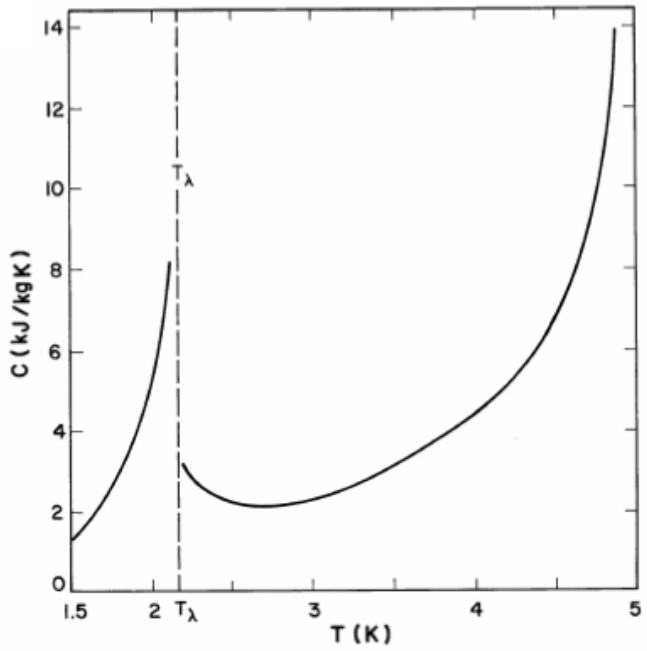

Figure 15. ^{4}He heat capacity as a function of temperature. He I and He II phases are shown on the right and left sides of the lambda temperature T_λ, respectively [23].

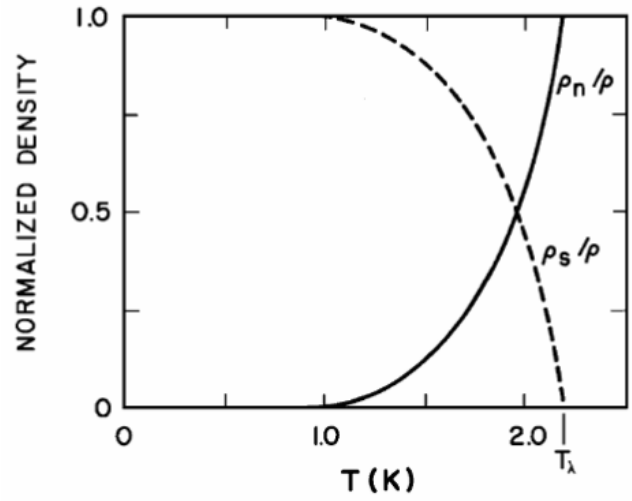

Figure 16. Superfluid and normal fluid density normalized to bulk He II density as a function of temperature [23].

He I and He II states never exist simultaneously, and the second-order phase transition between them makes clear their unique independent thermodynamic state properties. The He I and He II heat capacities are shown in Figure 15, separated by the discontinuity at the lambda temperature where the slope of the entropy is also discontinuous [23]. The normal fluid in the He I phase acts similarly to classical fluids and is even comparable to a weakly interacting gas due to its low viscosity and intermolecular attraction [23]. He II, on the other hand, is a quantum fluid and exhibits truly remarkable properties that are beyond classical comparison. This phase can be explained using Tisza and Landau's two-fluid model which states that He II is composed of both normal fluid, which contains the excitations and behaves as an ordinary liquid, and superfluid, which has no viscosity and no entropy [23]. The relative portions of normal fluid and superfluid are temperature dependent, and the ratios of normal (ρ_n) and superfluid (ρ_s) densities to the bulk liquid density are shown in Figure 16 [23]. At 1 K, 99% of He II is in the superfluid state, which cannot carry heat,

and is responsible for the rapid drop in heat capacity below the lambda temperature [23]. This contrasts with ^{3}He, whose large magnetic spin entropy gives rise to a large heat capacity: 40 times larger than the heat capacity of ^{4}He at 1 K.

Though He II exhibits many unusual transport properties, the thermomechanical fountain effect is particularly useful in the context of the AMRR system. This effect is demonstrated by placing a vessel of He II in a bath of He II and using a porous superleak to allow only superfluid to exchange between the two bodies of fluid. A superleak is a plug with pores on the order of a nanometer through which superfluid can flow without resistance, but normal fluid is blocked. The setup is shown in Figure 17 [23]. Both bodies are initially near 1 K, then a heater is used to increase the temperature of the inner vessel which promotes superfluid to the normal state, raising the pressure and forcing normal liquid to fountain out of the top. The resulting pressure difference drives the flow of superfluid from the bath into the vessel through the superleak, replacing the exiting normal fluid. This superfluid flow can also be explained considering the He II chemical potential, which is maintained at the same value for both bodies through this exchange. The relationship between superfluid flow direction and temperature change can be determined given:

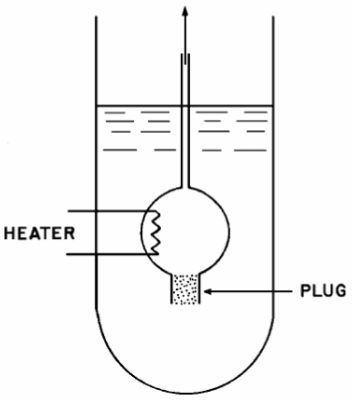

Figure 17. Experimental setup to demonstrate fountain effect in He II [23].

$$\left.\frac{\partial n}{\partial T}\right|_{\mu} = -n^2 \kappa_T \left.\frac{\partial \mu}{\partial T}\right|_{n} \quad (1)$$

where κ_T is a positive isothermal compressibility, n is the number of atoms in the body of fluid, T is the temperature, and μ is chemical potential [24]. For He II, $\partial\mu/\partial T|_n$ becomes negative around 1 K, meaning that increasing the temperature of the vessel reduces the chemical potential and

results in an influx of superfluid atoms driven to find a new equilibrium potential between the two bodies [24].

2.2.3 ^{3}He-^{4}He Mixture Properties

Some cryogenic applications require a mixture of both isotopes, capitalizing on the unique individual properties of both ^{3}He and ^{4}He, and the way they interact as a mixture. Several of these properties can be observed from the ^{3}He-^{4}He mixture phase diagram shown in Figure 18 [25]. To specify the state of the mixture, three independent properties are needed [25]. The phase diagram shown is at a constant pressure, with temperature and ^{3}He molar concentration, x, as the two additional independent properties. In calculating mixture state properties, it is sometimes helpful to use ^{4}He chemical potential, μ_4, as one of the independent variables instead of x or T, so lines of constant μ_4 have been added to the diagram. As seen with ^{4}He, the lambda line separates regions of single-phase He I and He II in the mixture, though increasing the ^{3}He concentration depresses the temperature at which this transition occurs. The lambda line terminates at the tri-critical point, where T = 0.872 K and x = 66.9% ^{3}He [23]. At temperatures below this point, there exists a phase-separation region where the mixture separates into a dilute phase with He II and lower ^{3}He concentration and a concentrated phase with He I and higher ^{3}He concentration [23]. This is the region of interest for dilution refrigeration, as very low temperature cooling in this

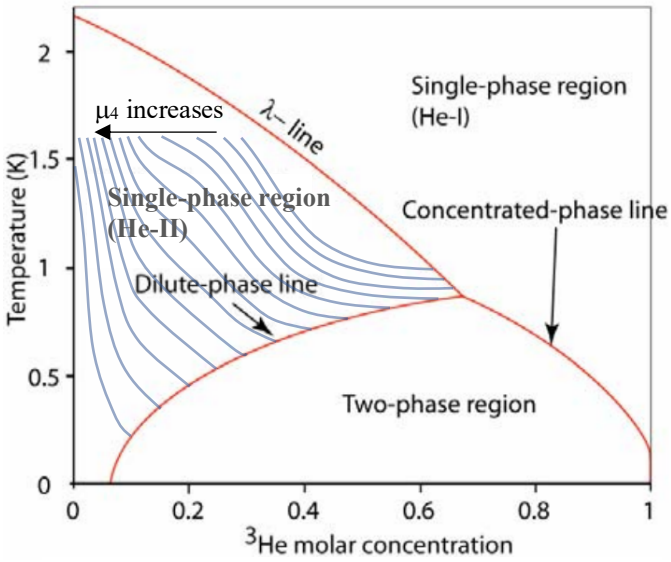

Figure 18. Phase diagram for ^{3}He-^{4}He mixtures at saturated pressure [25].

system is provided by transferring ^{3}He from a pure phase into the dilute phase, a process with a finite entropy of mixing.

It is critical to stay within the single-phase He II region while operating the AMRR for a variety of reasons. The superfluid component of the He II is vital to the operation of the SMP, which relies on the fountain effect to circulate fluid throughout the system. One canister is warmed while the opposite one is cooled, causing superfluid to rush from the cooling canister into the warming canister to equalize the chemical potential in the system and forcing normal fluid into the system. As can be observed by the lines of constant chemical potential in Figure 18, in a system of equal chemical potential the cold end has higher concentrations of ^{3}He. This results in a higher heat capacity in the cold heat exchanger than if He II were used alone. Recall that at temperatures below 1 K, ^{3}He has a heat capacity that exceeds 40 times the heat capacity of ^{4}He. To demonstrate this effect, the mixture heat capacity for various ^{3}He concentrations is shown in Figure 19 [25]. This experimental data has been smoothed, but effectively shows the impact of even small amounts of ^{3}He in increasing the overall mixture heat capacity.

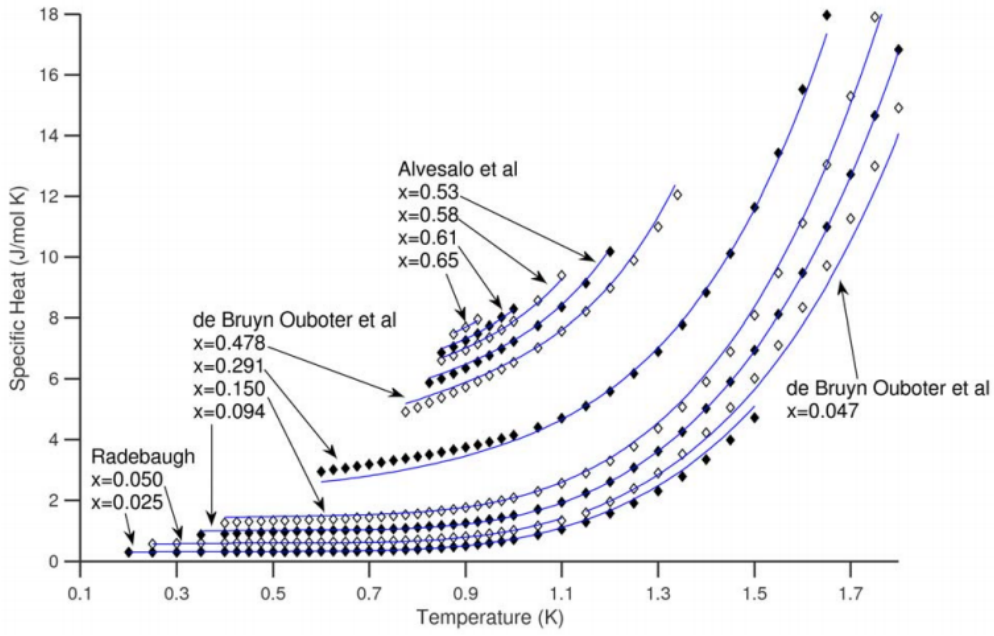

Figure 19. Specific heat of ^{3}He-^{4}He mixture for various concentrations [25], with data from [26] [27] [28].

Understanding the behavior of the mixture in the He II region is important for determining how to calculate some of the fluid properties needed to model the system; specifically the osmotic pressure and enthalpy, which require consideration of the superfluid behavior in the fluid. The bulk flow enthalpy, h, as well as other thermodynamic properties for a ^{3}He-^{4}He mixture, such as the specific volume, v, heat capacity, c, and concentration, x, are taken from Chaudhry, who fit property curves to smoothed data sets for ^{3}He-^{4}He mixtures [25]. Because there is a lack of consistent data in the region of interest, it should be acknowledged that there are limitations to the accuracy of these fits.

2.3 Magneto-Caloric Effect and Applications

The magnetocaloric effect, or adiabatic temperature change, is the heating or cooling of the material due to the interaction between magnetic moments in the material and a changing external magnetic field [29] [30]. The magnetic moments are attributed to the unfilled electron shells in some ions in the refrigerant, resulting in a total electronic angular momentum (J) of each of these ions [30]. When these moments align with an external magnetic field, the magnetic entropy (S_m) within the material is reduced. The resulting effect on temperature can be better understood looking at the total entropy of a magnetic solid (S), which is a function of both the magnetic field strength (B) and absolute temperature (T):

$$S = S_m(B,T) + S_l(T) + S_e(T). \tag{2}$$

The magnetic entropy becomes much larger than the lattice entropy (S_l) and entropy of conduction electrons (S_e) at low temperature, this is the main consideration for cryogenic applications [30]. The magnetic portion of the entropy can be represented by the following isolated paramagnetic spin equation, which assumes the magnetic moments within a material do not interact with each other:

$$\frac{S_m(T,B)}{R} = x \cdot \left(\coth(x) - (2J+1) \cdot \coth\left(x \cdot (2J+1)\right)\right) + \ln\left(\frac{\sinh\left(x \cdot (2J+1)\right)}{\sinh(x)}\right) \quad (3)$$

$$\text{where } x = \frac{\mu_B g B}{2 k_B T}. \quad (4)$$

The parameters include the gas constant R (8.314 J mol^{-1} K^{-1}), the Bohr magneton μ_B (9.27·10^{-24} J/T), the Boltzmann constant k_B (1.38·10^{-23} J/K), the total electronic angular momentum J, and the Landé g-factor g [30]. The Landé g-factor is a geometric factor that accounts for the changing orbital and spin momenta vectors relative to the applied field. The magnetic entropy also depends on the ratio of B/T; therefore, changing the applied magnetic field necessarily changes either the total entropy of the material or the temperature.

The link between temperature and applied magnetic field in a magnetic material is demonstrated visually in Figure 20 [29]. A material is initially at S_0, T_0, and applied magnetic field $H_0 = 0$. If the material is adiabatically and reversibly magnetized to H_1, the total material entropy remains constant; this process is represented by the horizontal arrow in Figure 20. The magnetic contribution to the entropy reduces as the magnetic ions align with the increased magnetic field. Consequently, the thermal entropy and temperature increase, maintaining constant total entropy in the system. This is captured in equations (2) and (3), where holding S_m constant while increasing B must increase T as well. Thus, the final state has a higher temperature due to the magnetization of the material. This process is reversible, and therefore with an adiabatic demagnetization the system can return to its initial state. The work done on the system is analogous to the adiabatic compression and expansion of a gas.

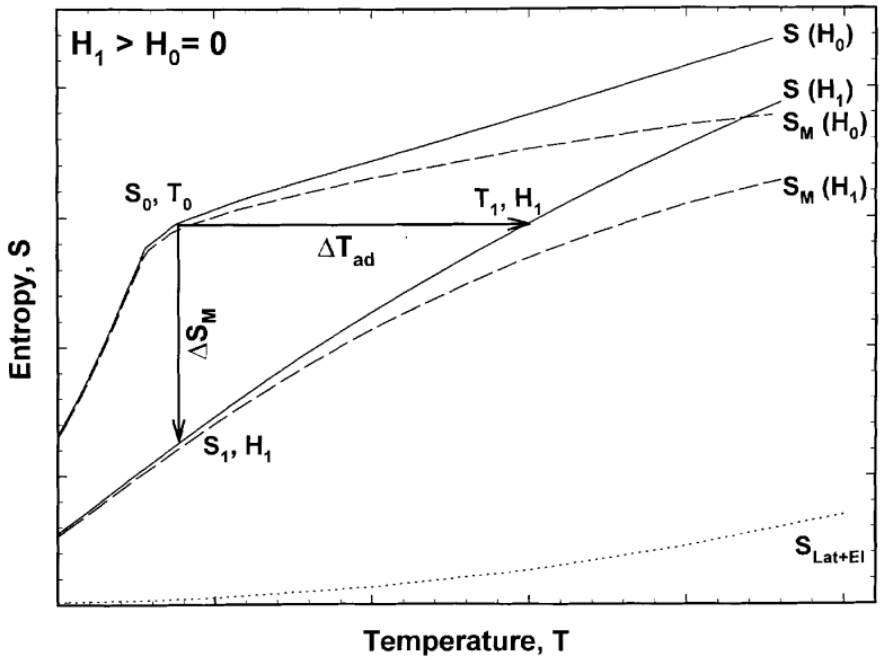

Figure 20. Visual representation of isothermal and adiabatic magnetization process in a magnetic material, indicated by vertical and horizontal arrows respectively [29].

At the opposite limit, a magnetic material undergoing an isothermal magnetization is also shown in Figure 20 by the vertical arrow. In this process, temperature and thermal entropy are constant by definition; therefore, the magnetization reduces the total entropy of the system as the magnetic moments become coupled to the increasing field. Heat must be removed from the magnetic material to maintain a constant temperature.

This effect was originally discovered in iron by Warburg in the late 1800s, and later proposed to achieve ultra-low temperatures through adiabatic demagnetization by Debye (in 1926) and Giauque (in 1927) [16]. Using the magnetocaloric effect, temperatures below the boiling point of liquid helium were achievable – the lowest reachable temperature at that time [16].

2.3.1 Paramagnetic Material Properties

Though the magnetocaloric effect can be observed in all magnetic material, materials that are paramagnetic at low temperatures have been the focus of early sub-Kelvin cooling research.

The magnetocaloric effect in paramagnets is maximized at temperatures approaching 0 K where the lattice heat capacity becomes negligible [29]. However, at a low enough temperature (which is material-dependent) known as the Néel or Curie temperature, most paramagnetic materials become magnetically ordered into ferro-/ferrimagnetic or antiferromagnetic states, severely reducing the zero field entropy and refrigerant efficacy [30] [31]. In selecting a paramagnetic salt for magnetic refrigeration, it is important to choose a material that is suitable for the temperature range of the system to ensure maximum adiabatic temperature change without risking material ordering. In this context, a variety of other factors should be considered as well, for example:

- larger magnetocaloric response is seen with large angular momentum J and Landé factor g;
- large thermal conductivity helps minimize temperature gradients;
- the material should exhibit small magnetic and thermal hysteresis;
- the material should be simple to make good thermal contact with;
- the material should be non-toxic, corrosion resistant, and easy to form; and
- the material should have a reasonable cost [30].

Table 2 contains various paramagnetic refrigerants that have sub-K ordering temperatures [30]. The temperatures listed in the table are the lowest temperatures achieved during heat capacity measurements of the materials and are the same as the refrigerant ordering temperatures in most cases. However, it should be noted that more recent research has reported that GLF has an ordering temperature below 0.25 K [31]. The AMRR system developed in this research is designed to provide cooling at a temperature no lower than 0.7 K, making Gadolinium Gallium Garnet (GGG) and Gadolinium Lithium Flouride (GLF) attractive options as they have ordering temperatures of 0.38 K and 0.25 K, respectively; temperatures closest to the design temperature without risk of

ordering. These two options have identical angular momentums and Landé factors, and both are often used as refrigerants at higher sub-K and low Kelvin temperatures.

Table 2. Angular momentum, Landé factor, lowest temperature achieved in measurements, and magnetic ion density for various paramagnetic refrigerants [30].

Refrigerant	Chemical Composition	J [1]	g [1]	T_o [K]	N [cm^{-3}]
CMN	$Ce_2Mg_3 \cdot (NO_3)_{12} \cdot 24H_2O$	1/2	2	0.0015	$1.65 \cdot 10^{21}$
CCA	$CrCs(SO_4)_2 \cdot 12H_2O$	3/2	2	0.01	$2.09 \cdot 10^{21}$
CPA	$CrK(SO_4)_2 \cdot 12H_2O$	3/2	2	0.009	$2.21 \cdot 10^{21}$
FAA	$Fe(SO_4)_2NH_4 \cdot 12H_2O$	5/2	2	0.026	$2.14 \cdot 10^{21}$
MAS	$Mn(SO_4)_2(NH_4)_2 \cdot 6H_2O$	5/2	2	0.17	$2.79 \cdot 10^{21}$
DGG	$Dy_3Ga_5O_{12}$	15/2 [a]	8	400	$1.28 \cdot 10^{22}$
GGG	$Gd_3Ga_5O_{12}$	7/2	2	0.38	$1.26 \cdot 10^{22}$
GLF	$GdLiF_4$	7/2	2	0.48	$1.34 \cdot 10^{22}$

As shown in Table 2, GLF has a slightly higher ion density than GGG, translating to a 20 to 60 percent larger entropy change than that of GGG [30]. However, GGG is still a suitable and widely used refrigerant at this temperature, has good thermal and transport properties, good chemical stability, reasonable cost, and can easily be crushed to the desired particle size [16] [30]. For the proof-of-concept AMRR developed in this research, GGG was chosen as the refrigerant for both the SMP and the regenerators, partially due to the large amount of GGG available to the UW-Madison Cryolab. Future iterations could use multiple stages of different refrigerants to reach lower temperatures.

2.3.2 GGG as a Refrigerant

GGG is often used in higher temperature ranges, typically from approximately 1 K up to 20 K; although the magnetocaloric effect diminishes approaching the upper temperature limit [30]. The low end of the usable temperature range for GGG is somewhat limited by the Néel temperature. However, the magnetic moments in GGG below this temperature interact in a way that does not lead to one preferred spin orientation and so magnetic ordering into an antiferromagnetic (AFM) state is dependent on the presence of an applied field [32] [30].

The AMRR system design temperature range is between 0.7 K and 1.8 K, well within the upper and lower bounds of GGG's useful temperature range. For this system, the entropy of the GGG can be modeled with a slight modification of Eqs. (2) and (3) to account for interaction between magnetic moments with no external applied field. These interactions are accounted for with an effective B value that averages the applied field with the material background field, b, which is 0.481 T for GGG [31]:

$$B_{eff} = \sqrt{B^2 + b^2}. \tag{5}$$

Using this correction, specific entropy for GGG is shown as a function of temperature for various applied fields in Figure 21. We can see that the zero-field entropy for material at 700 mK is about 9 J/mol-K. If this material is adiabatically magnetized to B = 1 T, the temperature will increase from 700 mK to 1.6 K – an adiabatic temperature change ΔT_{ad} of close to 1 K.

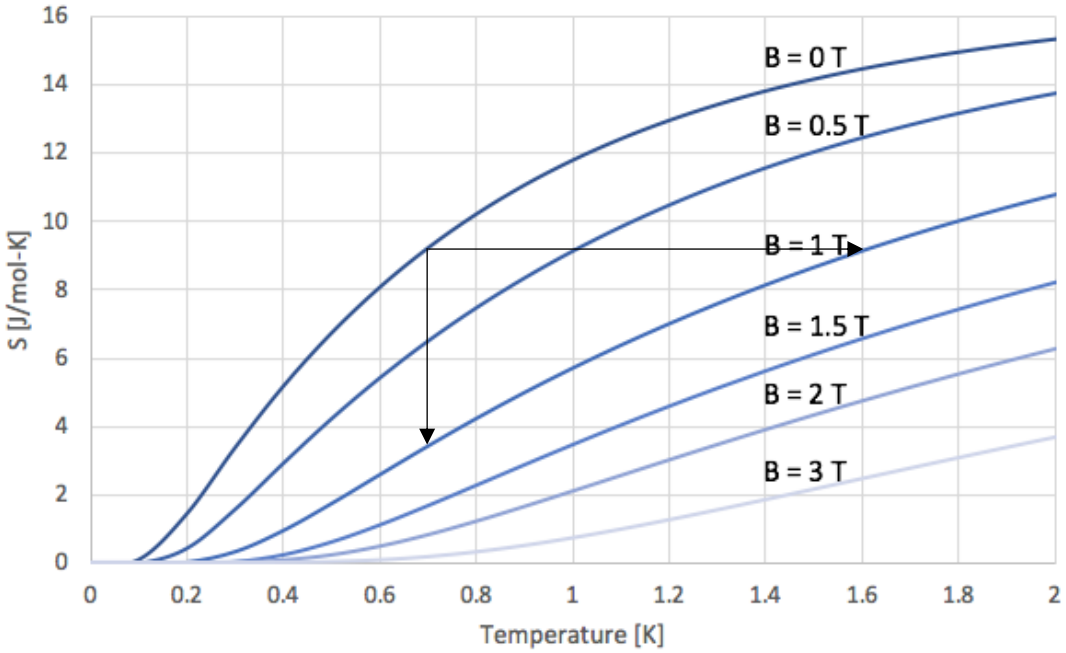

Figure 21. Specific entropy values for GGG as a function of temperature for select applied fields.

At the opposite limit, isothermal magnetization of GGG at 700 mK to $B = 1$ T will result in a final entropy of about 3.5 J/mol-K. With a total ΔS_M of 5.5 J/mol-K, 3.85 J/mol of heat must be rejected from the GGG. The regenerators within the AMRR system operate between these two limits.

A summary of important GGG properties, including molar weight (MW) and density (ρ), are provided in Table 3.

Table 3. Important GGG material properties.

Refrigerant	J [-]	g [-]	b [T]	T_N [K]	ρ [kg/m^3]	MW [kg/mol]
GGG	7/2	2	0.481	0.48	7080	1.012

2.4 Introduction to the AMRR System

For cooling large detectors at a few hundred millikelvin or to cool multiple lower temperature detectors via CADR stages, the AMRR system exploits many of the unique GGG and helium mixture properties to circulate the fluid and lift heat from the cold heat exchanger. A superfluid magnetic pump (SMP), two regenerators, one cold heat exchanger, and two hot heat exchangers comprise the AMRR system shown in Figure 22. The left hand side (LHS) and right

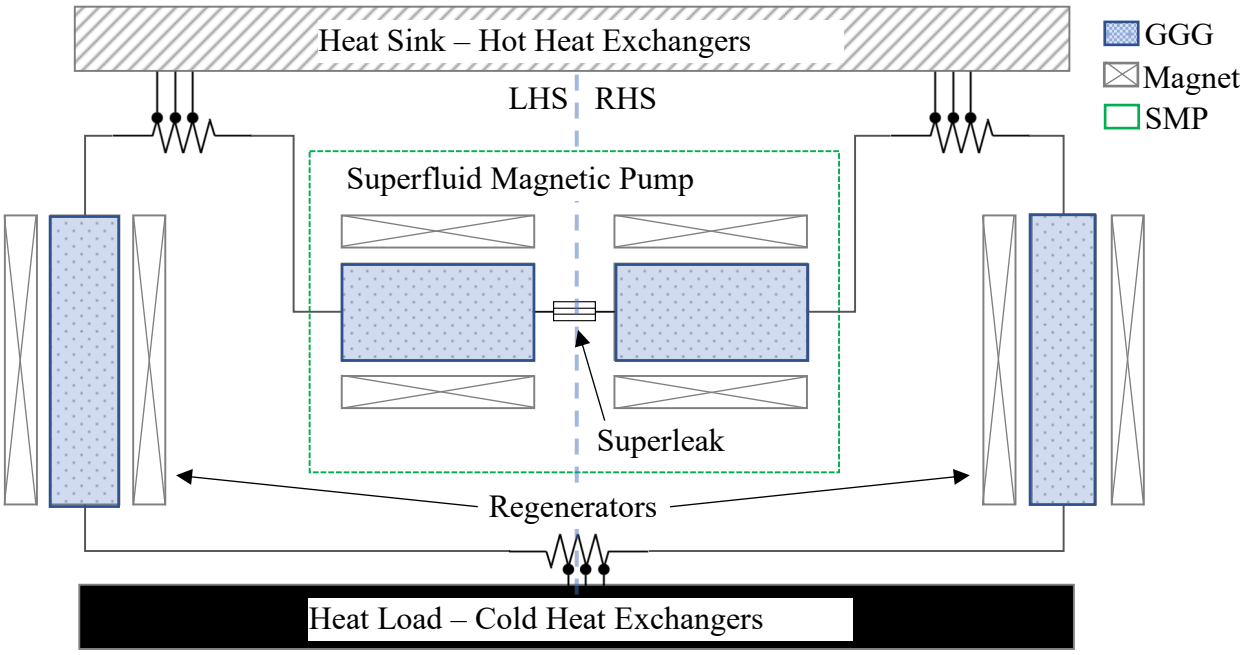

Figure 22. A diagram of the AMRR system.

hand side (RHS) operate identically and 180° out of phase of each other. This is a novel AMRR in that it uses the nearly thermodynamically reversible SMP to displace the fluid, resulting in a system with no moving parts. This greatly increases the reliability of the system and makes it a strong candidate for use in space for cooling sensitive instruments.

The SMP is composed of two separate canisters that are each filled with finely crushed paramagnetic GGG particles and are suspended within the hollow bores of superconducting magnets. A superleak with 4 nm pores connects the two pump canisters and allows superfluid ^{4}He to move freely between the two beds. To produce flow, the current in one coil is increased while the current in the opposite coil is decreased, resulting in increasing and decreasing magnetic fields, respectively. The shift in applied fields causes the thermal and magnetic entropies in the paramagnetic beds to also change due to the magnetocaloric effect. As the magnetic field in one canister rises, the magnetic entropy of the GGG must decrease. The thermal entropy thus increases, offsetting the magnetic change to the total entropy and raising the overall temperature. Because the ^{3}He-^{4}He is in good thermal contact with the GGG, the fluid tracks the temperature of the particles very closely. The increase in temperature promotes a portion of the ^{4}He from the superfluid state to the normal state, and forces fluid to exit the canister through the normal port into the rest of the system. The opposite is true for the canister experiencing a decreasing magnetic field. The superleak maintains continuity in the system, allowing only superfluid ^{4}He to cross from the cooling canister into the warming canister to replace the promoted ^{4}He. Flow in the system is reversed by alternating between increasing and decreasing the magnetic fields in each canister.

The magnetic regenerators are almost identical in construction to the pump. Canisters of crushed paramagnetic GGG are suspended inside the bore of superconducting solenoids by Kevlar strands. As fluid is forced out through the warming pump bed, it moves down through the

demagnetizing regenerator, which cools the mixture so that it exits the bed at the desired outlet temperature. The mixture then moves through a cold heat exchanger (CHX), providing sub-Kelvin cooling to the load (e.g., one or more detectors). It flows back up through the opposite, magnetizing regenerator which rejects more heat into the fluid. Finally, this heat is rejected to the precooling stage at a temperature around 1.6 K. The system can then be reversed, sending flow back in the opposite direction. The development of fluid flow is inherent to this system and is one of the most important differences between the AMRR and other cryogenic refrigeration systems as it addresses many of the aforementioned inefficiencies, making it an attractive option for future space science missions.

2.5 Introduction to CCA chemical formula and paramagnetic properties

The isolated paramagnetic spin model forms the basis for the entropy formula given in Eq. (3). Unfortunately, this fails to capture other low temperature effects that lead to entropy suppression at temperatures approaching zero K. Though it has become common practice to introduce an "effective field" to approximate this behavior, as seen in Eq. (5), this adjustment is admittedly "difficult to justify on theoretical grounds" [31]. To better understand from where the entropy suppression derives, it is important to understand a few key quantum level interactions that split the lowest energy levels in the ions that gives these low-temp salts their paramagnetic properties. Insights related to how these interactions effect the paramagnetic properties would enable better modeling and material selection for the coldest CADR stages.

The paramagnetic salts used in the lowest temperature CADR stages, namely FAA, CPA, and CCA, are all part of the alum chemical family. Alums are a group of hydrated double salts with the formula:

$$R^{i}R^{iii}(R^{vi}O_4)_2 \cdot 12H_2O \tag{6}$$

where R^{i} is a monovalent cation, R^{iii} is a trivalent cation, and R^{vi} is Sulphur for the cases considered [33]. In CCA, the monovalent ion is Cs^{+} and the trivalent ion is Cr^{3+}. Cr^{3+} is in the transition group and gives CCA its paramagnetic properties due to unpaired electrons in its 3d shell, which result in a nonzero spin value of S=3/2 [6]. Additionally, approximately 9.5% of the Cr^{3+} ions have a nonzero nuclear spin of I=3/2. Further information on stable Cr^{3+} isotopes is given in Table 4 [34].

Table 4. Spin values and natural abundances of Cr^{3+} stable isotopes [34].

Isotope	S Spin	I Spin	Abundance
Cr^{50}	3/2	0	0.0435
Cr^{52}	3/2	0	0.8379
Cr^{53}	3/2	3/2	0.0950
Cr^{54}	3/2	0	0.0237

The alum crystal is composed of face-centered cubic unit cells, each containing four trivalent ions [6]. Every trivalent ion is surrounded by an octahedron of six water molecules, creating near cubic crystal electric field symmetry at the ion and lowering the electrostatic energy of the dϵ orbitals (xy, yz, and zx) relative to the dγ orbitals (x^2-y^2 and $2z^2$-x^2-y^2) [6]. For reference, these orbitals are shown in Figure 23 [35]. With just three electrons in the 3d shell in Cr^{3+}, this energy shift results in a half-filled dϵ triplet and effectively quenches the orbital momentum [6, 36].

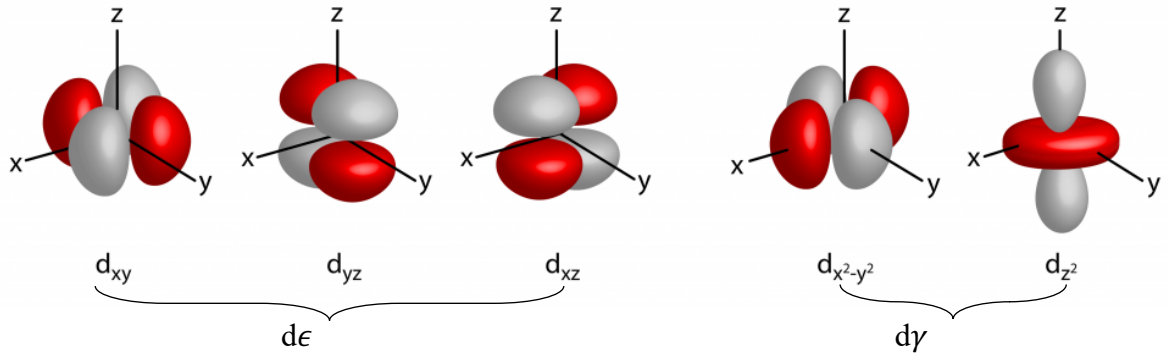

Figure 23. The d orbitals [35].

Zero field splitting

Distortions in the octahedrons can result in additional trigonal splitting, in which case the four trivalent ions in the unit cell are no longer equivalent and the direction of the external field relative to the crystalline axes needs to be considered [36]. For trigonal splitting, these symmetry axes are approximately oriented along each of the four cell body diagonals [37]. Though the trigonal field does not have a direct effect on the ground state, it gives rise to a spin-orbital coupling between the ground $^4S_{3/2}$ state and $^4P_{3/2}$ state that can split the ground state levels by a few tenths of a cm^{-1} [36, 38]. The total resulting change to the energy levels due to the crystal electric field is known as Zero Field Splitting (ZFS).

Zeeman splitting

When paramagnetic salts are placed in external magnetic fields, the interactions between the electron magnetic moments and the external field further split the energy levels of the ground state through the Zeeman effect. The combined ZFS and Zeeman effects for a Cr^{3+} ion in a trigonally distorted octahedron are shown in Figure 24, where the Zeeman effect is qualitatively shown as a function of increasing applied field for the energy levels in the ground state [38]. In predicting the

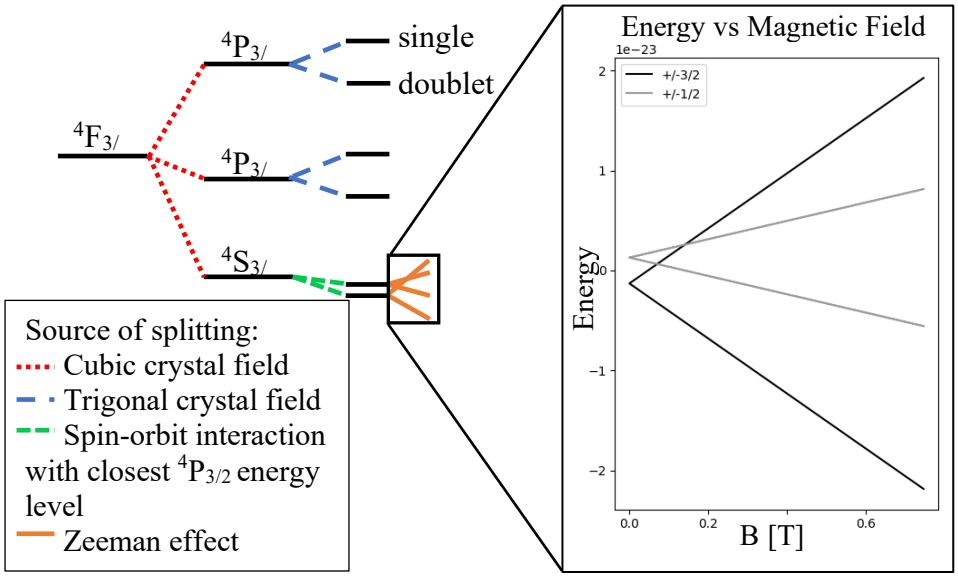

Figure 24. Explanation of energy splitting in ground state of Cr^{3+} ion in trigonally distorted octahedron [38]. Relevant energy levels are shown in the magnified graph on the right.

thermodynamic behavior of these ions only the ground state needs to be considered [37]. The relevant energy levels are magnified in Figure 24.

Hyperfine splitting

Lastly, as reported in Table 4, Cr^{3+} has a stable isotope with nonzero nuclear spin: Cr^{53} with I=3/2. In this case, the nuclear magnetic moment interacts with the electronic magnetic moment, subdividing each electronic energy level [6]. The unpaired electrons in the ion can also create an electric field gradient at the nucleus, consequently making some orientations of the nuclear quadrupole moment more favorable than others, further splitting the energy levels [6]. One final consideration is the interaction between an externally applied field and the nuclear magnetic moment, which is analogous to, but far smaller than, the electronic Zeeman effect. Though the nonzero nuclear spin isotope of Cr^{3+} has a relative natural abundance of just 9.5%, the associated hyperfine interaction terms that arise from a positive nuclear spin have been included in this analysis for completeness. The Zeeman, ZFS, and hyperfine interactions can be captured in a complete magnetic spin Hamiltonian to predict the thermodynamic properties of CCA.

3. Development of an Improved CCA Model

The CCA model developed in this work uses the complete spin Hamiltonian to predict the thermodynamic properties of the paramagnetic salt below a few hundred millikelvin. The details of this model, as well as comparisons with other theoretical paramagnetic models, are outlined below. We also describe the methods used by Warren Holmes and his colleagues at JPL to grow and characterize two salt pills. We used the data from these salt pills for model validation.

3.1 Experimental design

3.1.1 CCA salt pill growth

Prior to this work, two CCA salt pills were grown from a solution onto a gold wire thermal bus mostly following the process described in Hagmann [39]. The compressed wire bundle was inserted into a close fit cavity in a high purity copper bus bar-steel cap assembly with normal metal braze powder. The assembly was then vacuum brazed and inspected by X-ray to verify complete fill of the braze material within the copper cavity and around the pressed gold wires. A completed salt pill thermal bus assembly is shown in Figure 25. The thermal bus assembly was mounted in the crystal growth assembly shown in Figure 26. A stochiometric mixture of Cesium Sulphate (Cs_2SO_4) and Chrome Alum ($Cr_2(SO_4)_3*12H_2O$) dissolved in a liter of 21% nitric acid was poured into the top of the growth setup. CCA crystal growth was initiated by cooling the thermal bus to a range of temperatures -

Figure 25. CCA grown on thermal bus (top) gold wires brazed into gold plated copper thermal bus (middle) with stainless steel cap and sleeve (bottom).

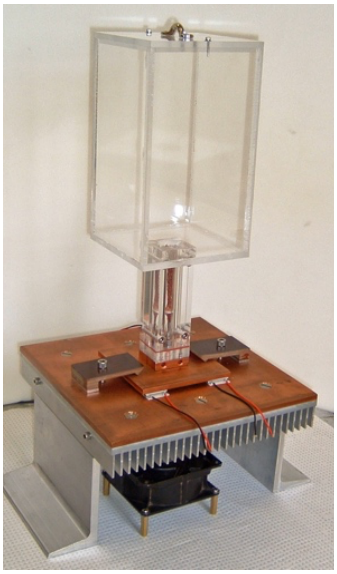

Figure 26. Crystal growth station.

10°C to 3°C using an array of thermoelectric coolers. Fresh solution was replaced roughly every week along with removal of stray crystal growth in flow channels on the side of the cylindrical mold region. Crystals were >90% complete after 6 weeks, removed from the mold and trimmed to slip fit into a stainless steel canister. Measured mass, after trimming, of the crystals grown on to the thermal bus are given in Table 5. A stainless steel canister was laser welded to the thermal bus assembly to hermetically seal the CCA against dehydration. Verification of the hermeticity of welding procedure was performed on an empty thermal bus canister assembly.

The completed salt pills were characterized using a vacuum insert dipped into a pumped liquid helium bath. The insert is equipped with a pumped ^{3}He stage with a base temperature of ~ 300 mK. The vacuum insert was located in the bore of a superconducting magnet immersed in the liquid helium. The base temperature of each CCA pill was below the quoted calibration range of the Ruthenium Oxide thermometer used on the sample. Using a standard calibration curve for this thermometer, we estimated that the base temperature achieved was ~ 20 mK. The CCA temperature increased from 20 - 50 mK in ~ 10 hours. Using this drift rate, the upper bound on the parasitic heat load from the 300 mK stage is of 20 nW.

Table 5. CCA pill assembly characteristics.

	Volume [cc]	Mass [g]	Cr^{3+} [mmol]	Gold wire [g]	Steel [g]	Copper [g]
CCA1	25	35.8	36	13.9	11.4	28.4
CCA2	25	30.5	30	13.9	11.4	28.4

3.1.2 CCA heat and refrigeration capacity measurements

The heat capacity measurements were taken by applying heat pulses to the pill at regular intervals and measuring temperature change. The temperature measurement from an example pulse is shown in Figure 27. To calculate the heat capacitance, a program was written in MATLAB to find linear fits to the first and second segments, and then extrapolate both segments to the center

of the heat pulse to find the corrected temperatures. These temperatures were used to find the ΔT associated with the pulse itself. We determined the change in energy from:

$$Q = \frac{tV^2}{R} \tag{7}$$

where t is the duration of the heat pulse (20s), V is the voltage that is applied during the heat pulse, and R is the resistance of the heater (22906 Ω). The applied voltages were adjusted in order to maintain a relatively constant ΔT value. The heat capacity is then calculated from:

$$C = \frac{Q}{\Delta T} \tag{8}$$

The refrigeration capacity was also measured using the heat pulse technique, but instead of determining a temperature change we find the decrease in applied field that is required to return the system to the initial temperature following a heat pulse event. The change in field, along with the input energy found with Eq. (7), can be used to find the refrigeration capacity at a given temperature and field:

$$\frac{\partial Q}{\partial B} \tag{9}$$

3.1.3 Parasitic heat and CCA conductance measurements

Careful experimental design is crucial for minimizing losses and increasing measurement accuracy. We characterized such losses through conductance and thermal relaxation measurements, as well as estimates of parasitic heat as a function of the temperature of the measurement stage. As the temperature of the pill decreases, the parasitic heat from the precooling stage becomes more significant. Estimates of this load at each experimental temperature point based on drifts in the baseline data were used to make corrections to the measured heat inputs and observed temperature changes. Following this adjustment, the maximum systematic error is estimated to be <0.4 mJ/K or <5.171e-25 J/ion-K. We measured thermal resistance between the thermal bus and the CCA for CCA1. Our conductance measurements fit to $1/T^3$ are shown in Figure 28 which indicates thermal resistance limited by the CCA to gold boundary resistance. The

absolute value of the thermal resistance is consistent with other measurements in the literature as shown in Figure 28 [39, 40]. Thus, the CCA is in good contact with the thermal bus. However, the literature values suggest that the thermal resistance could still be reduced by a factor of 3 if ideal surface contact is made between the CCA and gold [39].

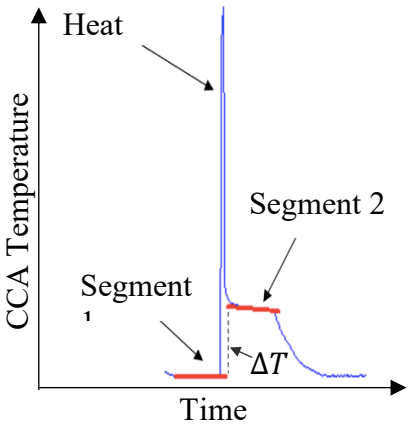

Figure 27. Method of determining heat capacity from heat pulse in paramagnetic salt. The settling time after the pulse is <1 minute and time span for a segment is 2 ~ 8 minutes.

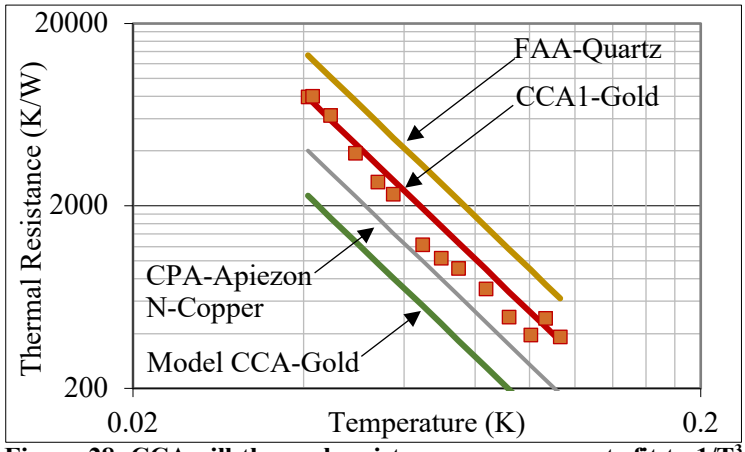

Figure 28. CCA pill thermal resistance measurements fit to $1/T^3$ compared with thermal resistance measurements of chrome potassium alum (CPA) to copper and ferric ammonium alum (FAA) to quartz.

3.2 CCA Model Development

3.2.1 Magnetic spin Hamiltonian

As previously explained, the Zeeman, ZFS, and hyperfine splittings all effect the lowest energy levels in the Cr^{3+} ion and therefore its thermodynamic properties. Together, these interactions comprise the magnetic spin Hamiltonian for a paramagnetic ion in a crystal, which can generally predict the behavior of the lowest energy levels. The Hamiltonian, assuming axial symmetry, is given as [6, 41, 38]:

$$\mathcal{H} = \beta g_{||} H_z S_z + \beta g_{\perp} \left(H_x S_x + H_y S_y\right) \tag{10}$$

$$+D\left\{{S_z}^2 - \frac{1}{3}S(S+1)\right\} \tag{11}$$

$$+AS_z I_z + B\left(S_x I_x + S_y I_y\right) \tag{12}$$

$$+Q\left\{{I_z}^2 - \frac{1}{3}I(I+1)\right\} \tag{13}$$

$$-\beta_n g_n \boldsymbol{H} \cdot \boldsymbol{I} \tag{14}$$

where *S* and *I* correspond to the ion's electronic and nuclear spins, respectively.

Equation (10) of the Hamiltonian captures the electronic Zeeman effect, where β is the Bohr magneton, **H** is the applied magnetic field vector, and g is the spectroscopic splitting factor [42]. The ZFS effect is accounted for by Eq. (11), where D is the crystalline splitting factor. Equations (12), (13), and (14) capture the effects of positive nuclear spin and are thus only included when $I>0$. In this event, Eq. (12) captures the interactions between the electronic spin and nuclear spin, Eq. (13) adds the nuclear quadrupole term, Q, and Eq. (14) represents the nuclear Zeeman effect, where β_{n} and g_{n} are the nuclear magneton and nuclear spectroscopic splitting factor, respectively.

The Hamiltonian parameters A, B, D, Q, g, and g_N have been extensively studied using paramagnetic resonance experiments for Cr^{3+} ions in chrome alums, though infrequently for CCA. A selection of observed values for these parameters for Cr^{3+} ions in CCA or similar crystals are given in Table 6.

Table 6. Experimentally determined Hamiltonian values for Cr^{3+} and corresponding measurement temperature.

Parameter [Unit]	Value	T [K]	Ref.
A [cm^{-1}]	17.557×10^{-4}	4.2	[38][a]
	17.2119×10^{-4}	4.2	[43][a]
B [cm^{-1}]	17.4875×10^{-4}	4.2	[38]
	17.4754×10^{-4}	4.2	[43]
D [cm^{-1}]	-0.066±0.001	20	[44]
	-0.06701±0.00050	4.2	[38]
	-0.0652±0.00050	4.2	[41]
Q [cm^{-1}]	$0.1547\pm0.0001\times10^{-4}$	4.2	[38]
	0.1546×10^{-4}	4.2	[43]
$\boldsymbol{g}$	$g_{\|\|}$ 1.9718±0.0050	4.2	[38]
	$g_{\perp}$ 1.9722±0.0050	4.2	[38]
	1.975±0.005	4.2	[41]
$\boldsymbol{g_N}$	-0.31114±0.00050	4.2	[38]
	-0.3110	4.2	[43]

[a]Values taken from [9, 12] are for $CsGa(SO_4)_2$ enriched with Cr^{3+}

3.2.2 Modeling method and calculations

The magnetic interaction Hamiltonian and experimentally determined parameters were used to develop a model in Python for calculating the thermodynamic properties of CCA. Complete spin matrices for the Cr^{3+} ion for both parallel and perpendicular orientations of the applied field to the z-axis can be found in [41, 38]. Diagonalization of these Hamiltonian matrices gives the energy eigenvalues of the ion. The partition function can then be used to find the thermodynamic properties of the ions given these energy levels, and is defined as:

$$Z = \sum_i e^{-\beta E_i} \tag{15}$$

where β is equal to $(k_B T)^{-1}$, k_B is the Boltzmann constant, and T is the temperature. The expected energy, $\langle E \rangle$, and heat capacity, C, of the ion can then be determined using the following equations:

$$\langle E \rangle = -\frac{\partial \ln Z}{\partial \beta} \tag{16}$$

$$C = \frac{\partial \langle E \rangle}{\partial T} \tag{17}$$

Additionally, we calculated the predicted refrigeration capacity of the ion, which is defined as:

$$T \frac{\partial S}{\partial B} \tag{18}$$

where B is the applied magnetic field and S is the entropy, calculated using:

$$S = \frac{\partial (k_B T \ln Z)}{\partial T} \tag{19}$$

We had sets of data from the two different CCA pills described in Section 3.1.1, introducing an additional ions/g scaling parameter for each data set, representing the total number of Cr^{3+} ions in the respective samples, and an effective field parameter, adjusting for possible off-center axial suspension of the sample within the magnet bore and field edge effects.

3.2.3 Cr3+ ion energy, magnetic moment, and heat capacity in CCA

Before fitting the model to our data, we used it to better understand the impact of the previously explained splittings on the energy levels, magnetic moment, and heat capacity of the Cr^{3+} ion itself. An energy level diagram for the Cr^{3+} ion in CCA with the magnetic field parallel to the z-axis is shown in Figure 29. The effect of trigonal compression of the water octahedron around the Cr^{3+} ion can be seen, as the ±3/2 states are lower in energy than the ±1/2 states at zero field [41, 38]. At low enough temperatures, the energy difference between these sets of states at zero field and the points where they overlap at low fields have a significant impact on the energy and entropy of the ion. In terms of Hamiltonian parameters, this compression results in a negative D ZFS parameter [41, 38]. This distortion also increases the B hyperfine parameter relative to A for isotopes with nonzero nuclear spin [41, 38].

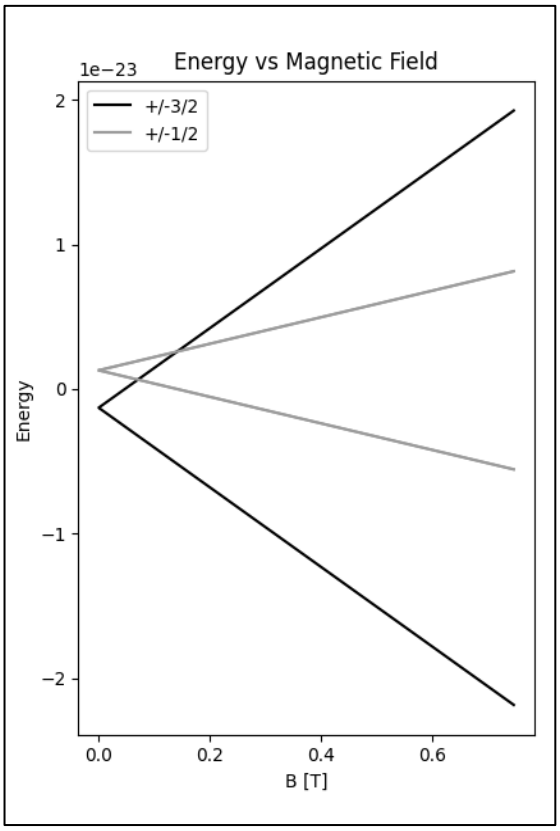

Figure 29. The lowest energy levels in the Cr^{3+} ion.

It is also informative to look at the effects of ZFS through comparison with the well-known Brillouin theoretical function, which gives the average magnetic moment per ion as a function of B/T [Tesla/Kelvin]. Without inclusion of the ZFS D term in the Hamiltonian for I=0 ions, agreement between magnetic moment predictions by the Hamiltonian and Brillouin function is quite good. The inclusion of this ZFS term results in the temperature dependent divergence shown in Figure 30, where the magnetic field is assumed to be oriented along a crystal cubic axis.

Similarly, it is common to report heat and refrigeration capacity curves as a function of B/T. Figure 31 further highlights the consequences of ZFS as these predicted thermodynamic properties diverge from ideal paramagnetic behavior at temperatures approaching zero Kelvin.

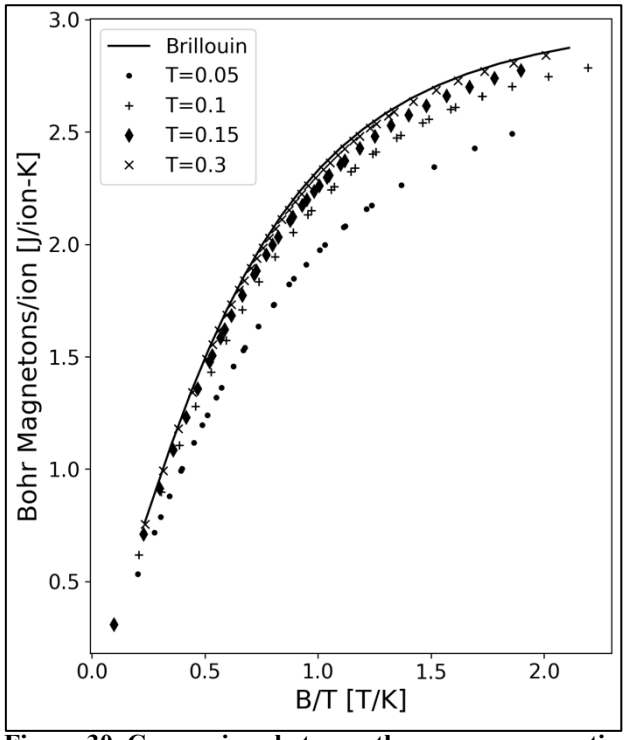

Figure 30. Comparison between the average magnetic moment per Cr^{3+} ion calculated by Hamiltonian and Brillouin function.

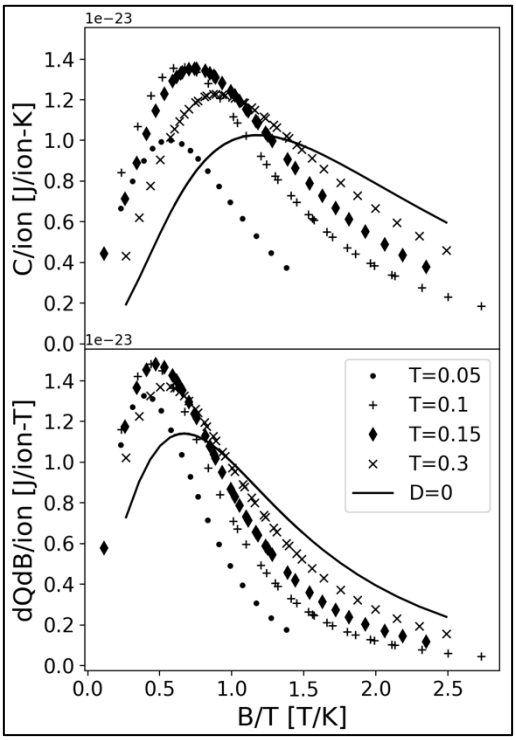

Figure 31. Heat and refrigeration capacity curves for Cr^{3+} ion with and without ZFS.

4. CCA Model Results

Following the initial work to develop the CCA thermodynamic model, we focused on fitting the CCA model to our data. Through the CCA model examination, we determined which low temperature effects have the greatest impact on the salt properties and whether the inclusion of the additional splitting terms provided an improved fit to the experimental data over the isolated paramagnetic spin model.

4.1 CCA Model Results

The CCA investigation focused on quantifying the effects of different low temperature magnetic interactions, determining the heat capacity of CCA through experimental testing, and combining these efforts to improve the understanding and modeling of CCA properties. To understand which of the previously described effects has a significant effect on the thermodynamic properties of the salt in the temperature range of interest, we explored the effects of changing select Hamiltonian values from Table 6. Because Cr^{53} is the only isotope with nonzero nuclear spin and has a low natural abundance of 9.5%, it is easiest to see the effects of the hyperfine interaction terms

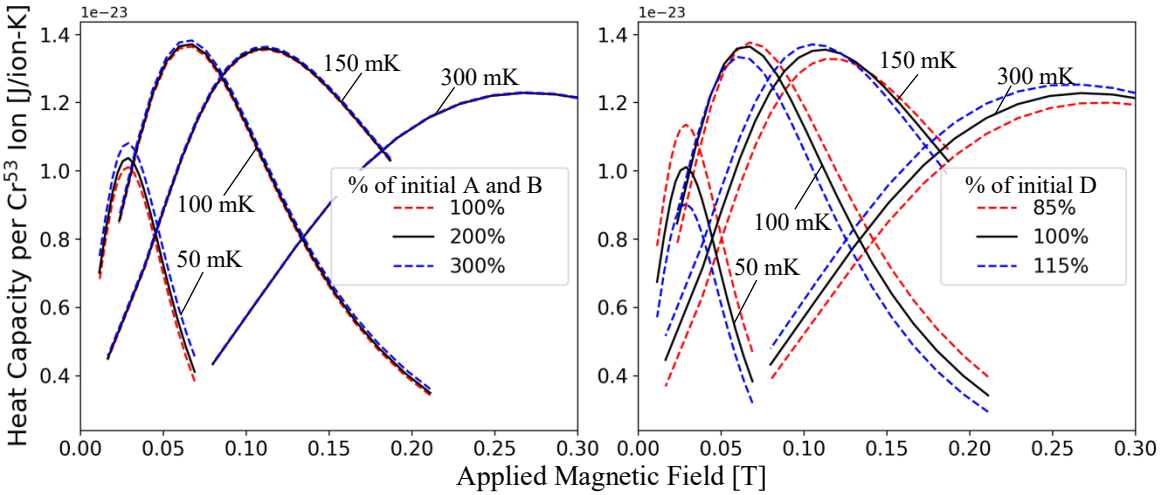

Figure 32. Effects of varying the hyperfine A and B parameters (left) and ZFS D parameter (right) on the specific heat of a Cr^{53} ion. Both plots have the same ranges and scales.

considering just this ion. Heat capacity curves for Cr^{53} with the hyperfine A and B parameters at 100%, 200%, and 300% of their initial values are shown in the left plot in Figure 32. It is apparent that changing the A and B hyperfine parameters does not have a material impact on the total predicted heat capacity. Changing the ZFS D factor, however, does. Heat capacity curves with 85%, 100%, and 115% of the initial ZFS D value are shown on the right in Figure 32. To highlight the sensitivity of the ZFS parameter, both plots are for a single Cr^{53} ion and have the same ranges and scales. The greatest changes are seen at 50 mK, where increasing A and B to 200% and 300% of their initial values increases the peak predicted heat capacity by approximately 3% and 7%, respectively. As with the hyperfine A and B parameters, changing the ZFS D parameter had the greatest effect on the lowest temperatures. An increase of 15% of the initial D value decreased the 50 mK peak heat capacity by approximately 10%.

For model fitting to experimental data, we excluded hyperfine interactions and assumed that the applied field was oriented along the cubic axis of the crystal. This orientation is at an angle θ relative to the trigonal axes, where $c = \cos^2\theta = \frac{1}{3}$ for all four trivalent ions in the unit cell [45]. The energy levels for this orientation are taken from [45, 46]. As previously noted, the only independent fitting parameters are the ions/g scaling factor, which scales the model from a single ion to the total number of ions per gram in each pill, and effective field scaling factor, which scales the applied field for possible off-centered suspension and field edge effects. Because parasitic loads and measurement uncertainties increase at decreasing temperatures, we fit the independent parameters to the 300 mK measurements. Additionally, because addenda heat capacity potentially contributes to the heat capacity measurements, we fit the model to the refrigeration capacity data, which includes only magnetic contributions. Contour plots of the best fit values for this parameter

space using a nonlinear least-squares analysis are shown in Figure 33. The data points were weighted by both estimated measurement error and by distance from the center of the 300 mK temperature peak, giving higher importance to the critical fit area.

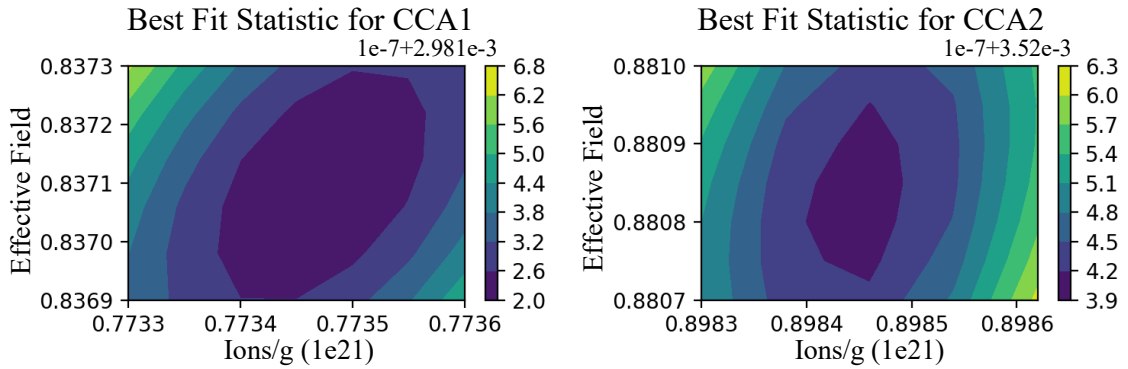

Figure 33. Contour plots of best-fit statistic for scaling parameters from least-square fits to 300 mK refrigeration capacity data.

The final values from this fit, as well as estimated parameter values, are given in Table 7. The estimated field scale is calculated from averaging the actual applied field based on the magnet geometry over the crystal volume. The estimated ions/g is found using the molar mass and crystal structure of CCA.

Table 7. Estimated and best fit parameter values for CCA1 and CCA2 refrigeration capacity data.

Effective Field Scale	CCA1	CCA2
Estimated	0.87	0.87
Applied	0.8371	0.8808
Ions/g Scale	**CCA1**	**CCA2**
Theoretical [ions/g]	1.02×10^{21}	1.02×10^{21}
Fill Fraction [ions/g]	0.7735×10^{21}	0.89845×10^{21}

The measured specific refrigeration capacities, along with the capacities predicted by the model using the best fit parameters from Table 7, are shown in Figure 34 for the two CCA salt pills. The cooling capacity was measured for two CCA salt pills from 50 mK – 300 mK. The isolated paramagnetic spin model tells us that there should be a peak value refrigeration capacitance that is a function of the applied magnetic field, shifting to higher magnetic fields for higher temperatures.

The measured cooling capacity shows significant reduction below this spin model for temperatures below 100 mK. The inclusion of the ZFS parameter in our model results in better qualitative agreement with this low temperature reduction, as shown in Figure 34. However, measured data at 50 mK still shows a significant reduction below our model prediction. Though increasing the magnitude of the D value appears to better approximate the suppression of capacity at lower temperatures, this does not fit the general trend for the splitting parameter found in literature. D is temperature dependent but is observed to decrease in magnitude approaching absolute zero [41]. Thus, an increase in the ZFS is an unlikely explanation for the experimental behavior of the CCA salts at this temperature.

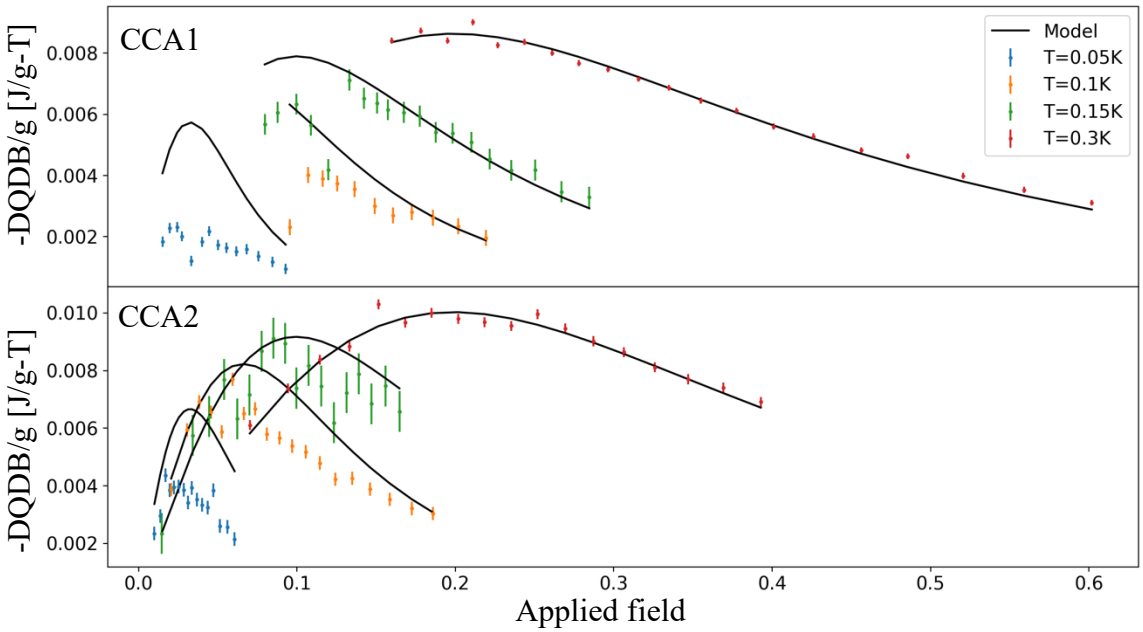

Figure 34. Model fit to CCA refrigeration capacity data with Cr^{3+} best fit parameters from table 7.

Finally, to evaluate addenda heat capacity and entropy loss due to non-adiabatic effects we examined the experiment collection ranges in the context of the entropy-temperature plane shown in Figure 35. Here, the beginning and ending data collection points for each temperature are shown

with the blue and red circles, representing CCA1 and CCA2 respectively. A magnetic refrigeration cycle is overlayed on this plot. We can see that in the low field, low temperature limit there is a transition to reduced capacity. The ideal ratio of S=3/2 to S=1/2 is $\ln(2)^{-1} \cong 1.44$; the model is close to the isolated spin limits. Examination of Figure 35 allows us to evaluate non-adiabatic losses as well. The magnetization at constant temperature is consistent with the modelled field curves. This agreement helps verify that the addenda heat capacity is small and changes temperature adiabatically with the salt. The thermal resistance measurement of the salt to the thermal bus and thermal relaxation times of the temperature measurement stage were also used to characterize addenda heat capacity and entropy loss. These checks find that the reduction in cooling capacity below 100 mK cannot be accounted for by excess addenda heat capacity or non-adiabatic effects.

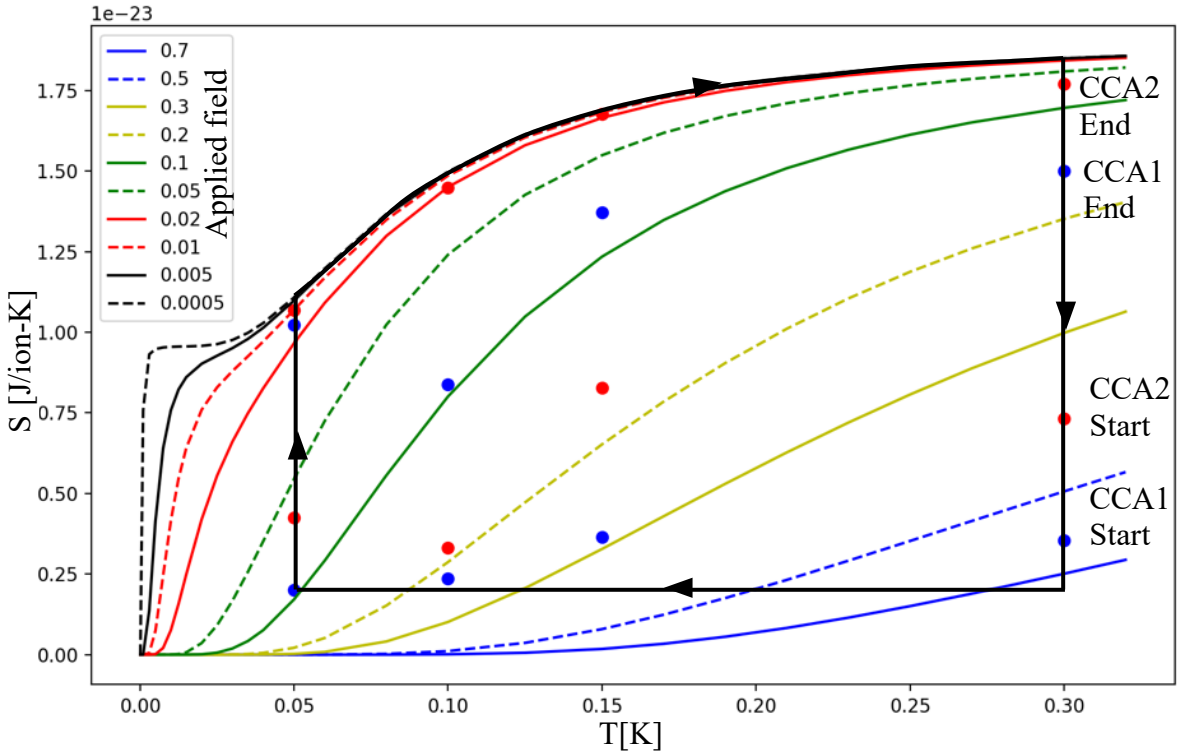

Figure 35. CCA temperature-entropy plot with lines of constant applied magnetic field. The circles represent the beginning and end points of the data collection at 50 mK, 100 mK, 150 mK, and 300 mK, with CCA1 in blue and CCA2 in red. A magnetic refrigeration cycle between 300 mK and 50 mK is outlined in black.

5. Design and Construction of AMRR System

The AMRR system developed in this work was designed to be integrated with an existing SMP. A simple numerical system model was used to design the AMRR regenerator magnets and canisters, and then these components were constructed and assembled to form the complete AMRR system. The AMRR design and construction work is discussed in this chapter.

5.1 Introduction

The development of a proof-of-concept AMRR system relies on the proper design of each component to ensure that there is enough paramagnetic material and sufficient magnetic field to force circulation of the fluid and manipulate the temperature of the ^{3}He-^{4}He mixture throughout the system. The objective of the proof-of-concept AMRR is to provide measurable cooling at the CHX with this novel cycle. Simulating the behavior of the system with a high level of accuracy is difficult because of the large number components that interact throughout the multi-process cycle. These components do not only interact at their boundaries but also by redistribution of the different components of the mixture in order to satisfy both continuity and equilibration of chemical potential. In particular, there is nearly instantaneous movement of superfluid in the system that is driven to maintain uniform chemical potential. The simulation is further complicated by the complex dependence of the helium properties and the magnetocaloric material properties on multiple state variables, leading to a highly nonlinear system. For the development of a proof-of-concept system, a simplified model of the AMRR focusing on a single regenerator is adequate to inform the design process as it allows the approximate determination of the required cooling capacity of the regenerator without attempting to entirely capture the complexities of the AMRR system. As a functional SMP already exists in the UW-Madison SEL, this process primarily

focused on the design of the remaining components that are required to complete the AMRR system: the superconducting regenerator magnets, regenerator canisters, and CHX.

5.2 AMRR Cycle Design Model

In order to properly design the remaining AMRR components so that they match the existing SMP, a model is required to guarantee refrigeration at the desired temperature. A simple model was developed focusing on a single AMRR regenerator, and the subsequent magnet and CHX models were developed based on the results of this model. For a more complete understanding of these models, an introduction to and explanation of the AMRR cycle processes is necessary.

5.2.1 AMRR Cycle Description

The AMRR cycle consists of four main processes which repeat in the following order: No Flow Demagnetization (NFD), Flow Demagnetization (FD), No Flow Magnetization (NFM), and Flow Magnetization (FM). Each side of the system is identical in construction and they operate 180° out of phase from each other. This means that while one side is in the NFD or FD process, the opposite side is in the NFM or FM process, respectively. Because of this tandem operation, it is important to understand that the explanation of each process is representative of the behavior of just one side of the AMRR, which consists of one regenerator, one SMP canister, one hot heat exchanger (HHX), and half of the CHX. A diagram of half of the system is shown in Figure 36.

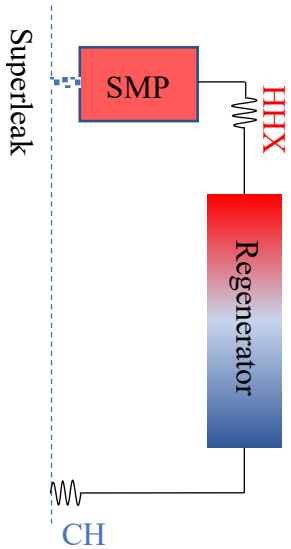

Figure 36. The RHS of the AMRR system.

The NFD process is shown in Figure 37 and begins with the regenerator at its maximum cycle magnetic field and temperature, and the SMP canister at its minimum cycle magnetic field and temperature. Field strength is represented by the blue ovals, with more lines indicating higher fields. The temperature is qualitatively represented by the color, with 1.7 K shown in dark red and 0.75 K shown in dark blue. During the NFD process, the SMP field is held constant, so there is no temperature change in the canister and no induced flow in the system. The regenerator is demagnetized, increasing the magnetic entropy of the GGG and lowering the temperature profile in the canister until the cold end temperature equals the inlet temperature of the CHX, designed to be at 0.75 K. At this point, the FD process can begin.

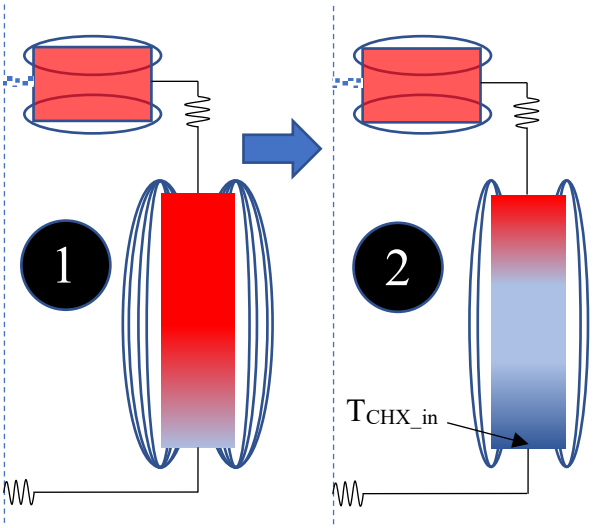

Figure 37. The start and end of the NFD process in the RHS of the AMRR.

During the FD process shown in Figure 38, the SMP canister is magnetized, warming the fluid and forcing the mixture into the rest of the system due to the previously explained fountain effect. Superfluid ^{4}He crosses the boundary into the warming canister during this process, driven to maintain a constant system chemical potential. The exiting mixture flows through the HHX into the regenerator,

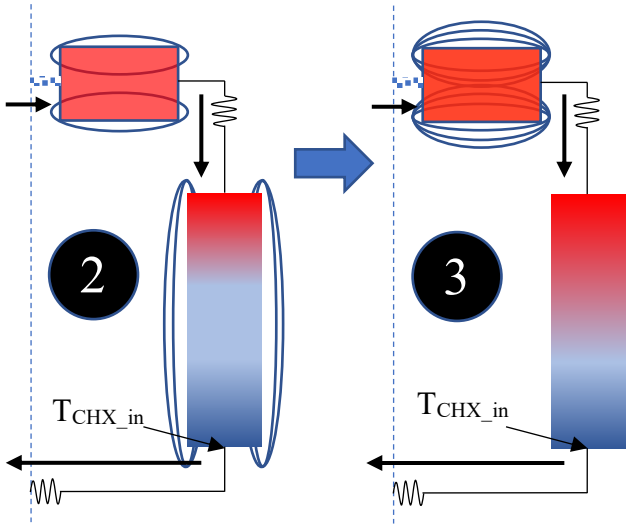

Figure 38. The start and end of the FD process in the RHS of the AMRR.

which is still demagnetizing and cooling the fluid so that it exits at the desired CHX inlet temperature. The fluid then moves into the CHX, where a thermally linked instrument can reject heat into the mixture. The mixture exits the CHX into the opposite side of the AMRR. Eventually, the regenerator field depletes to 0 T, at which point the NFM process begins.

During the NFM process shown in Figure 39, the SMP canister has a constant field and temperature, resulting in no flow in the system. This is similar to the NFD process, except the SMP canister is now at its maximum temperature and field. The regenerator magnetizes at a constant rate, warming the temperature of the entrained fluid. This magnetization continues until the opposite side of the AMRR, in the NFD process, has a low end regenerator temperature equal to the desired CHX inlet temperature. At this point, flow can begin again in the opposite direction, and the system moves into the final process: FM.

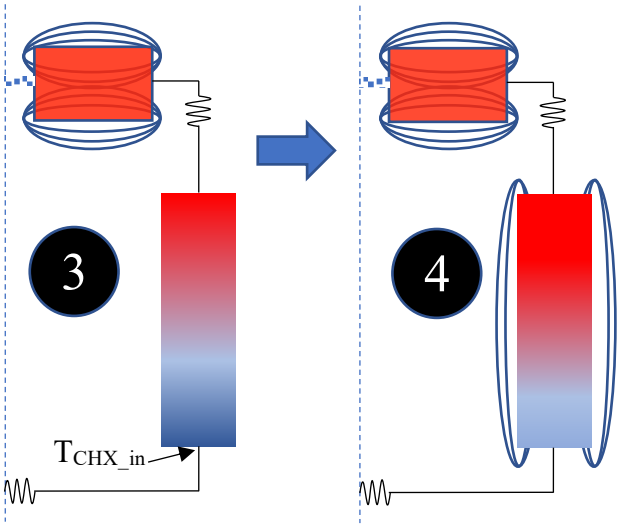

Figure 39. The start and end states of the NFM process in the RHS of the AMRR.

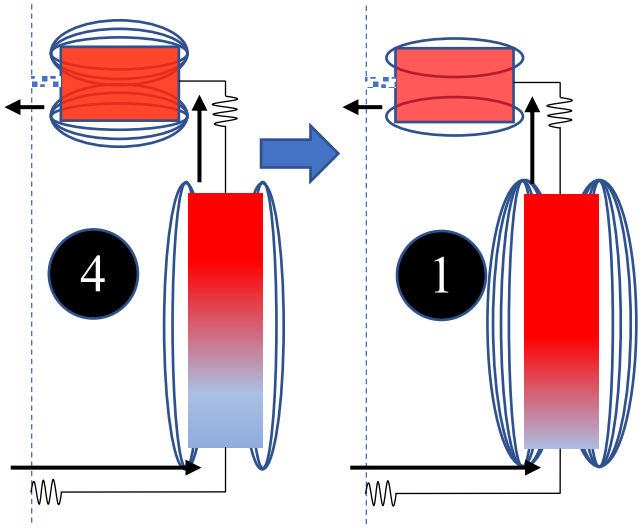

Figure 40. The start and end states of the FM process in the RHS of the AMRR.

In the final system process, shown in Figure 40, the SMP canister demagnetizes, lowering the temperature and drawing in fluid from the system as superfluid ^{4}He exits through the superleak into the

warming canister. The regenerator continues to magnetize, warming the incoming fluid from the CHX. After moving through the regenerator, the mixture rejects heat at the HHX and enters the cooling SMP canister. This process continues until the maximum magnetic field is reached in the regenerator and the minimum field is reached in the SMP canister. The completion of this process returns the AMRR system to its initial state and thus represents the completion of a single cycle.

5.2.2 Simple Design Model for AMRR Regenerators

Our simplified 1D transient design model focused on one regenerator canister during a flow process in the AMRR system. The control volume (CV) for the regenerator is indicated by the dashed box in Figure 41 and contains only the fluid; the mixture enters at the left from the

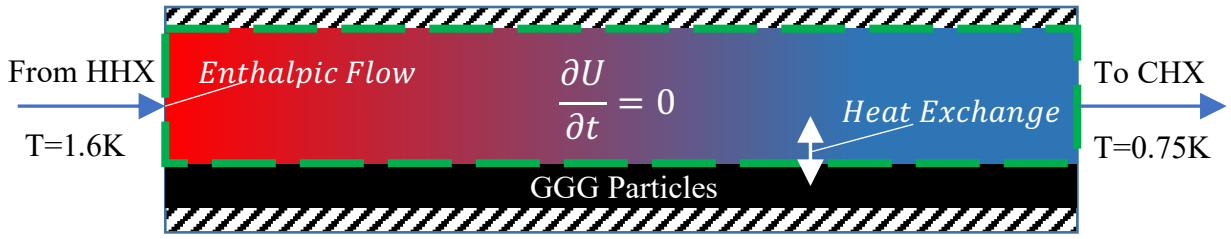

Figure 41. Control volume for regenerator canister. Fluid enters from the HHX at the left and exits to the CHX on the right.

HHX at 1.6 K and exits on the right to the CHX at 750 mK. We assume a constant linear temperature distribution between these two extremes across the regenerator, a conservative assumption relative to the expected temperature swings. The GGG particles are represented by the black box below the CV, and the magnetocaloric effect is captured through the heat exchange between the fluid and particles at the CV boundary according to the second law balance:

$$\frac{dQ_{GGG}}{T} = dS_{GGG}(B,T), \tag{20}$$

where dQ_{GGG} is the heat into the GGG, dS_{GGG} is the entropy change of the GGG, and T is the temperature at the boundary. The GGG is discretized into spatial (i=1…N) and temporal (j=1…M) nodes. This captures the entropy dependence on changing magnetic field and the spatial variation

in local temperature. Rearranging terms and expanding the expression for entropy provides the total heat into the GGG in node *i* during timestep *j*:

$$Q_{GGG,i,j} = T_i \cdot n_{GGG} \left(\frac{\partial s}{\partial B}\Big|_{B=B_j} \left(B_{j+1} - B_j\right) \right), \tag{21}$$

where T_i is the boundary temperature at node *i*, n_{GGG} is the number of moles of GGG in node *i*, B_j is the field at time *j*, and the derivative of the entropy as a function of magnetic field is evaluated at B_j. Note that we can ignore temperature-driven changes in the entropy as we are assuming a constant (in time) temperature throughout the process. Summing over *i* from 1 to *N* sums the heat contributions from every node and summing over *j* from 1 to *M* sums the heat contributions over the entire process.

Performing a first law energy balance on the total CV gives:

$$n_{in} h_{flow,HHX} = n_{out} h_{flow,CHX} + \sum_{j=1}^{M} \sum_{i=1}^{N} Q_{GGG,i,j}, \tag{22}$$

where n_{in} and n_{out} are the number of moles of mixture moving into or out of the regenerator, respectively, $h_{flow,HHX}$ and $h_{flow,CHX}$ are the molar specific enthalpies of the mixture at the two ends of the regenerator , and $Q_{GGG,i,j}$ is, again, the heat out of the mixture into the GGG.

Several design constraints include the inner diameter of our canister, the maximum allowable field swing, which determined our field values used in our entropy calculation, and the total number of moles circulated through the regenerator, which determined our enthalpy term. Using Eq. (22), we were able to determine the canister length required to maintain an outlet temperature of 750 mK during the flow process.

The final regenerator canister dimensions and required field swing are then used to constrain the magnet design. The equation for the magnetic field along the axis of a solenoid is derived in Jahromi[3], and is given as:

$$B_{axis,inside} = \frac{\mu_0 N_{turn} I}{2}\left[\frac{x}{\sqrt{x^2+R_{coil}^2}} + \frac{L_{coil}-x}{\sqrt{(L_{coil}-x)^2+R_{coil}^2}}\right], \quad (23)$$

where μ_0 is the permeability of free space, $4\pi \times 10^{-7}(N/A^2)$, N_{turn} is the total turns per unit length, I is the current in the coil, x is the axial location, L_{coil} is the length of the coil, and R_{coil} is the effective radius of the coil, calculated at half of the coil thickness. Equation (23) can be used to find the total number of turns for a given mandrel geometry required to reach the desired field at the center of the coil. For the regenerator, the magnets were designed to reach a maximum of 1.5 T, more than twice the required field for the flow process according to the simple model.

5.2.3 Final Regenerator Design

The final regenerator design includes the canister pieces, magnet mandrel and winding specifications, and suspension system for thermally isolating and centering the canister within the bore of the magnet. The final design is shown in Figure 42.

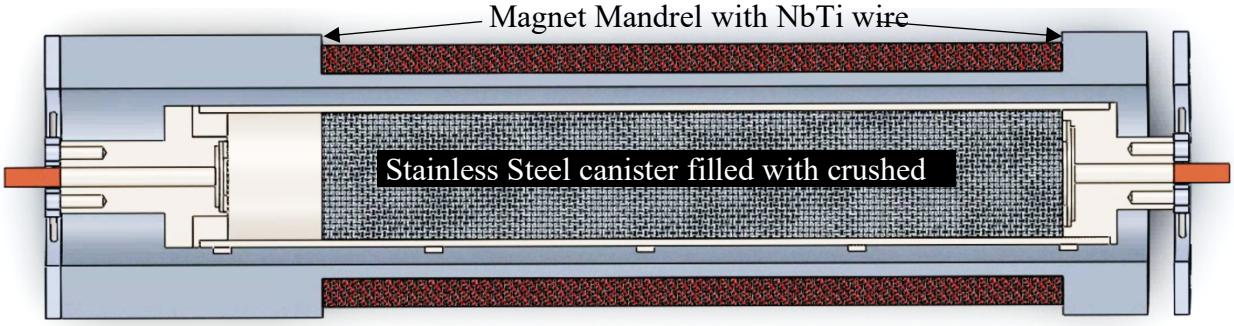

Figure 42. Cross-sectional view of the final regenerator design, which includes the canister, suspension, and magnet.

The regenerator canister is composed of four stainless steel pieces: the thin-walled tube and three end caps. Two of these end caps are welded to the tube, one with an opening to allow for packing, and the third is welded into the open cap after the canister is packed with GGG. Inlet and outlet headers are included in the endcaps to allow for even flow distribution radially within the regenerator. Fine mesh screens are used to prevent the movement of GGG particles into these volumes, consequently preventing the displacement of GGG into the remainder of the system.

Because GGG has a relatively large heat capacity under these conditions (which would be undesirable in the unmagnetized portion of the bed), crushed glass with the same particle size and fill porosity as the GGG was used to fill the extra volume in the canister that extended beyond the magnet length as glass heat capacity approaches zero at the temperatures within the regenerator.

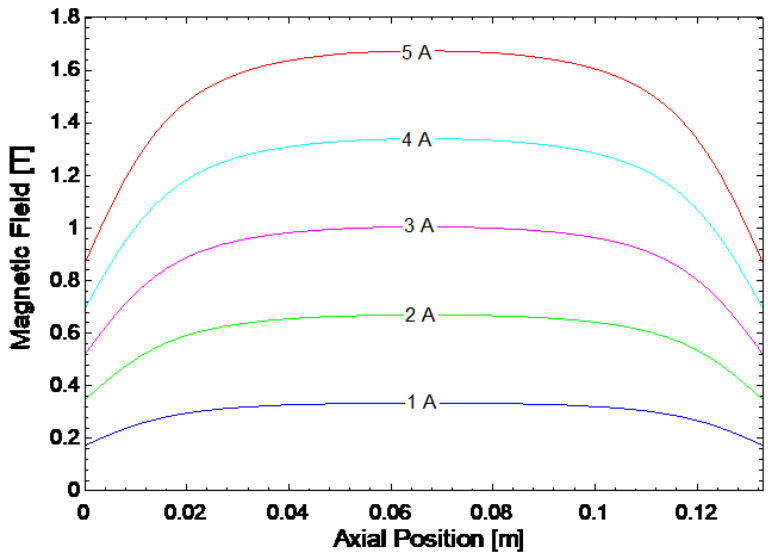

Figure 43. Magnetic field at center axis as a function of axial location for different currents.

The regenerator magnet consists of a niobium-titanium (NbTi) coil potted in an aluminum mandrel. The wire chosen contains 54 NbTi filaments, each with a diameter of 9 μm, embedded in a stabilizing copper matrix with a total insulated diameter of 0.127 mm. This diameter, along with a conservative current of 4.7 A, was used to determine the number of turns required to reach 1.5 T in the center of a magnet. The magnetic field at the center of the regenerator as a function of axial location is shown in Figure 43 for various currents. One other important component of the magnet is the diode pocket, which is located in one of the flanges and contains two back-to-back diodes to prevent coil damage if a quench occurs. When this happens, the coil transitions into a normal state and the forward voltage of the diode is exceeded, redirecting the current through these diodes.

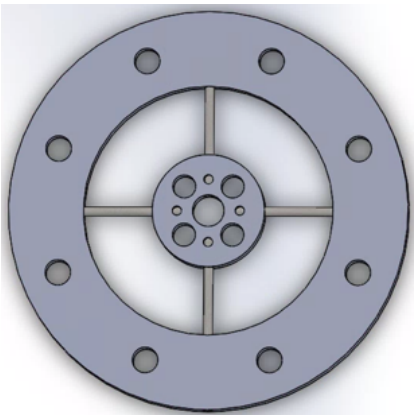

Figure 44. The regenerator suspension design.

The final regenerator component, the suspension, is composed of a center disk suspended by Kevlar within a thin aluminum ring. This suspension is shown in Figure 44 and is identical on both sides of the regenerator. The center disk attaches to the regenerator canister, while the outer ring is supported by the magnet mandrel, centering the canister within the bore of the magnet. Kevlar is incredibly strong in tension, having a tensile strength around 3.6 GPa, and has a very low thermal conductivity. These qualities make it an attractive option for use in suspending and thermally isolating the canister.

A summary of key final regenerator design parameters is provided in Table 8:

Table 8. A summary of key final regenerator canister and magnet parameters.

Regenerator Canister		Regenerator Magnet	
Canister Material	304 Stainless Steel	Mandrel Material	6061 Aluminum
ID [m]	0.0229 m	ID [m]	0.03175 m
OD [m]	0.0254 m	OD [m]	0.0508 m
Porosity [-]	0.38	Coil Material	54S43 NbTi
GGG Fill Length [m]	0.133 m	Coil Length [m]	0.133 m
Glass Fill Length [m]	0.017m	Current [A]	4.7 A
Total Mass GGG [kg]	0.240 kg	Number of Turns [-]	37,000
Total Mass Canister [kg]	0.204 kg	Max Field [T]	1.5 T

5.3 AMRR System Construction

After finalizing the remaining AMRR component designs, we began construction. This included machining the canisters, mandrels, and suspension components, winding the magnets, and crushing and packing the GGG into the canister. These components were then assembled to complete the AMRR system.

5.3.1 Regenerator Canister Assembly

As previously mentioned, the canister assembly consists of one thin-walled tube and three endcaps, all machined out of stainless steel. Two of the endcaps are shown in Figure 45. These endcaps are welded to the end of the tube to seal the canister once the GGG has been packed and have header volumes for better distribution of incoming fluid. Two mesh screens with <0.08 mm openings are fit into the header volume to prevent GGG particles from escaping. One complete regenerator is shown in Figure 46. Brazed into each outermost endcap is a short length of copper tubing to allow for easy integration with the rest of the system assembly.

Figure 45. The regenerator canister endcaps.

Figure 46. One finished regenerator canister.

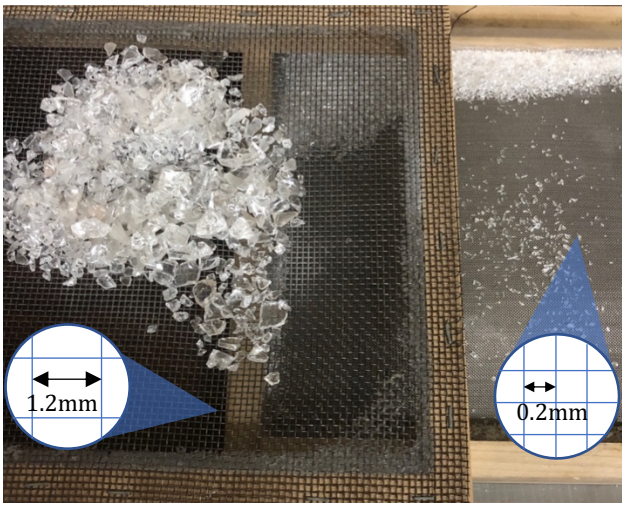

Figure 47. The two sieves used to achieve a GGG particle size of approximately ≤1 mm.

Though GGG crushes into irregular shapes, the target particle size was roughly ≤1 mm in diameter. To achieve this, two sieves with 1.2 mm and 0.2 mm hole widths were used to create a go no-go gage. Figure 47 shows an image of the sieves taken during the crushing process. Large chunks of the crystal were hammered into finer pieces, which were placed on top of the wider sieve and shaken to ensure that all particles with diameter <1.2 mm would pass through into the second sieve. The particles collected in the second sieve could be used to pack the canister beds. Any finer particles that passed through the second sieve were discarded.

In order to reach the optimal porosity of 0.38 in the canisters, we determined the mass of GGG required to fill 62% of the internal canister volume. We slowly packed this mass into the canister, vibrating the canister throughout the process to ensure even distribution of the particles. Once filled, we pushed the canister end cap on and vibrated the canister to allow the particles to settle further. We then reopened the canister to fill the small void created from settling and repeated this void filling process until there was no void from settling to guarantee that the particles were packed tightly and would not shift during operation. Once each canister was fully packed, we welded the remaining endcap in place to permanently seal the open end. The GGG particles do not get hot enough during this process to melt the crystal.

5.3.2 Regenerator Magnet Assembly

We used thick walled 6061 Aluminum tubing to create the magnet mandrels, turning down the outer radius to form flanges on either side of the winding length and reach the required mandrel thickness.

To prepare for winding, we polished the winding surface and flanges using six different 3M polishing papers, which stepped down from 30-micron paper to 1-micron paper. Polishing the mandrel is crucial because under the forces created by the winding process and the magnetic fields even small imperfections on the surface can cut through the wire insulation and short the coil to the mandrel. Once polished, the surface was extensively cleaned to remove any paper fibers or residue from machining. We subsequently wrapped the winding surface and flanges using 0.025 mm thick Kapton to further protect against shorts by creating a backup insulation layer between the coil and mandrel. The Kapton layer also minimally increases the thermal resistance between the coil and mandrel – an important consideration in the event of a quench when the coil must reject heat to the mandrel.

Prior to winding, the wire is wrapped and secured around one of the flanges to provide an adequate lead length. The wire is fed through the diode pocket into the mandrel and secured at the entry point. Care is taken not to wrap the wire tightly around one edge of the channel when entering the winding surface. A picture of this setup is shown in Figure 48.

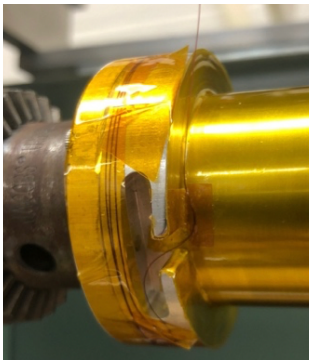

Figure 48. The setup of one magnet mandrel prior to winding.

During the winding process, we continuously brushed CTD-A521 magnet epoxy onto the coil using a silicone bristle brush. Potting the coil in epoxy helps prevent frictional heating in the magnet by preventing movement of the coil loops due to forces created during magnetization. The epoxy also helps to create good thermal contact between the wires and mandrel, allowing for efficient heat rejection.

Once the number of required turns was reached, we wrapped and fastened the second magnet lead around the flange. In order to prevent the epoxy from running off or distorting the coil, the magnet was slowly rotated on the winding machine for at least 24 hours as the epoxy cured.

To finish the magnets, we stripped the insulation on the leads in the diode pocket, and then soldered two back-to-back 1N4001 diodes across the leads. This pocket is then filled with epoxy to secure the diode configuration and create a good thermal link to the mandrel. As noted previously, the current is redirected through these diodes in the event of a quench, when the voltage across the coil leads exceeds the forward voltage of the diodes. The diodes are placed back-to-back so that the direction of the applied current does not matter. Images of the AMRR magnets installed in the cryostat are shown in Figure 49.

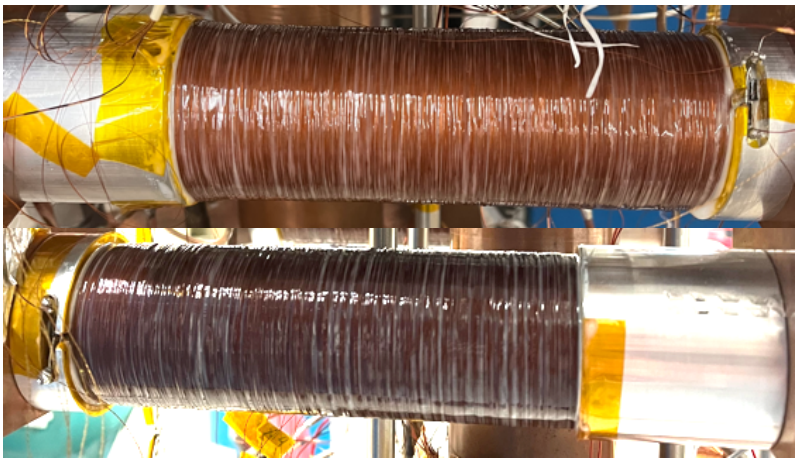

Figure 49. The two regenerator magnets installed in the cryostat.

5.3.3 Entire AMRR Assembly

Prior to installing the AMRR system into the Dewar, suspension components had to be machined. These included copper end brackets for the magnets and suspension rings for centering the canisters within the mandrels. The copper brackets have the same conduction resistance from the magnet to the 4 K plate as the preexisting copper brackets used with the SMP canisters, ensuring that the magnet will not heat up too much in the event of a quench. The brackets are positioned within the Dewar to suspend the regenerator canisters parallel and approximately below the pump canisters, as shown in Figure 50. The red arrows indicate the locations of the two SMP canisters, and the green arrows point towards the regenerators. The circulation path is configured so that while one regenerator is magnetizing, the above pump canister is also magnetizing and vice versa; in this way deconstructive interference of the magnetic fields is minimized.

The HHXs used in the AMRR system were already attached to the bottom of the 1 K stage. The temperature of this platform can be controlled by a heater to maintain a precooling temperature around 1.5 K. The CHX consists of tubing attached to a copper plate with a contact length that matches the design length. The CHX plate also has a heater attached to allow control and measurement of the cooling power of the system.

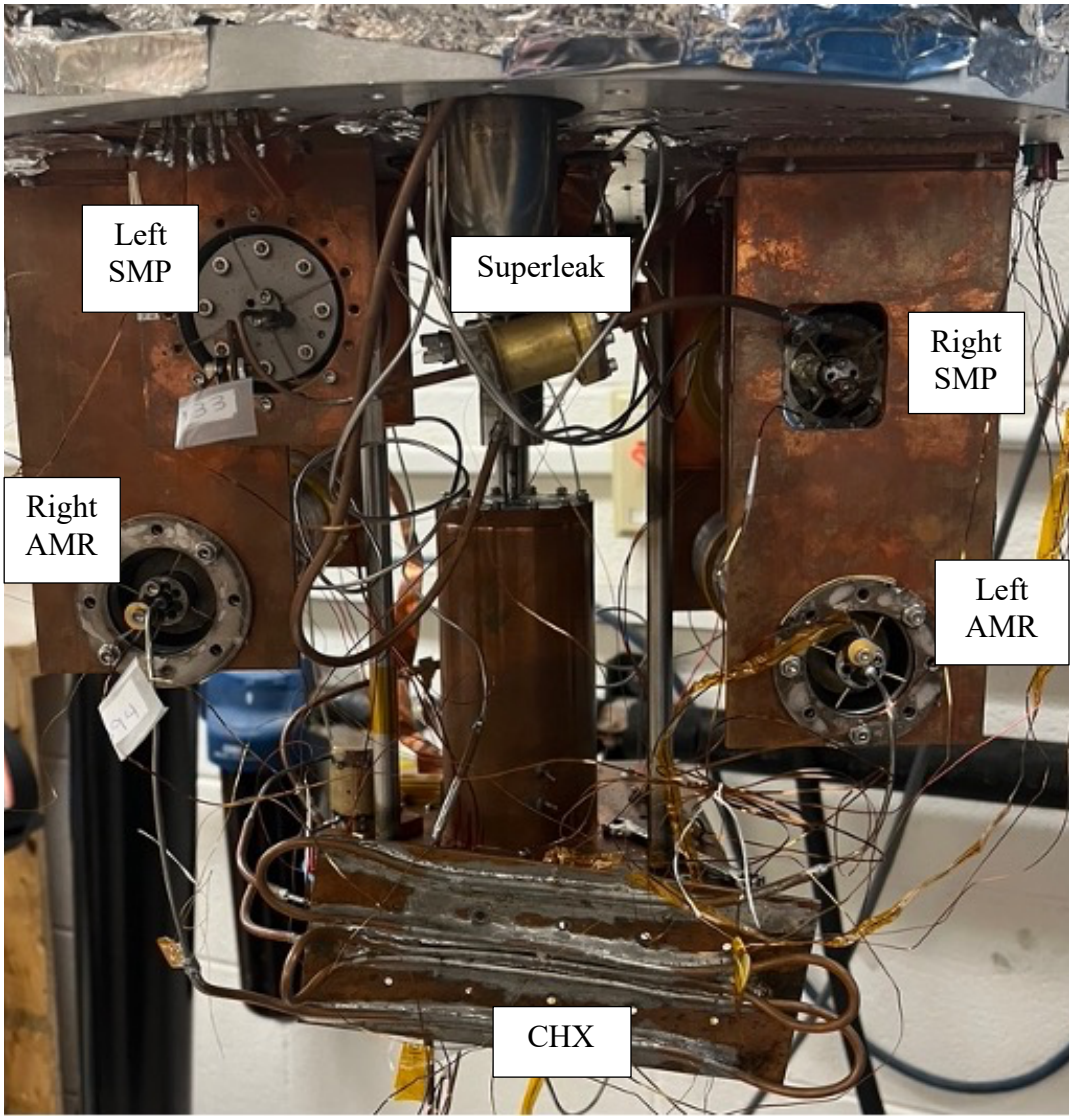

Figure 50. AMRR assembly in Dewar.

The construction of the individual AMRR components was relatively straightforward, but we have encountered several challenges during the assembly of the AMRR system:

- The first two regenerator magnets failed after a handful of cooldowns. Further investigation showed shearing of the leads in the diode pockets, likely from differences in the epoxy and wire CTEs. We adjusted the diode filling method, and our two replacement magnets are still functioning after being thermally cycled numerous times.
- Backstreaming of oil from the vacuum pump into the AMRR fill line required a complete disassembly of the system and flushing of the fill lines. We have replaced this pump with a diaphragm pump.
- The 1 K pot used to cool the AMRR system developed a superfluid leak. We completely rebuilt this system, replacing the indium and soldered joints with brazed joints, and it is now leak tight.
- The AMRR system had one or more cold leaks. Because these leaks only exist at low temperatures, they were nearly impossible to find. We decided to disassemble the AMRR and reassemble it one component at a time to locate the leaks. Through this method, we determined that the indium seals in the regenerator canisters were leaking. After replacing the indium seals numerous times without success, we decided to redesign the endcaps and weld the canisters shut. Despite these efforts, one regenerator still appears to have a very small superfluid leak.

5.4 AMRR ^{3}He-^{4}He Mix System

As previously explained, one of the unique benefits of the AMRR is that it is a circulatory system which uses a ^{3}He-^{4}He mixture to lift heat. This working fluid relies on the individual properties of the two helium isotopes and requires a specific concentration of ^{3}He to effectively

lift heat without reaching a region of phase separation. Ensuring that we reach and maintain the accurate concentration requires care in both the mixing and storage of the gas mixture.

To properly size the mixture storage container and choose appropriate pressure gauges, we made an initial estimate of the number of moles of mixture required to fill the system based on the internal volumes of the system components and tubing. The total system volume is approximately 110 cc, which requires 0.1398 moles of ^{3}He, and 3.8556 moles of ^{4}He to reach a ^{3}He concentration of 3.5%. To account for any errors in our volume estimate and ensure there was enough gas remaining in the fill tank to condense liquid into the system at 1 atm, we mixed 150% of this initial mole estimate. This required a ^{3}He pressure of 10.8 kPa and a total mixture pressure of 311.34 kPa in our 49.6 L mixture tank.

Ensuring these two pressures were achieved within an acceptable degree of accuracy required two separate gauges – one for the ^{3}He and one for the mixture. For the lower pressure ^{3}He measurement, we used the Wallace & Tiernan gauge shown in Figure 51 which has an uncertainty +/- 0.25 torr. To eliminate any systematic errors related to the gauge reference pressure and "zero" point, we first filled the line with ^{4}He to a base pressure of 106.25 torr. We then added ^{3}He until the pressure reached 187.3 torr to reach the total 81 torr of ^{3}He required in our mixture. For measuring the pressure of our total mixture, we used the Ashcroft compound gauge shown in Figure 52 which has a range of 30 in Hg vacuum – 60 psi. Because this gauge uses atmospheric pressure as its zero point, we used a barometer to get a precise measurement of this pressure to within +/- 0.1 torr and adjusted our total pressure accordingly. We continued to add ^{4}He to the mixture until we reached a total mixture gauge pressure of 30.5 psi +/- 0.15 psi. Propagation of the uncertainties of each individual gauge allows us to determine the overall uncertainty of our mixture concentration, which is 3.5% +/- 0.016%.

Figure 51. Wallace & Tiernan gauge used to measure the pressure of the ^{3}He in the mixture.

Figure 52. The Ashcroft compound gauge used to measure the total mixture pressure.

Building a mixing system with leak tight tubing, joints, and tank is essential for guaranteeing that the mixture remains pure and is not slowly depleted over time. To achieve this, our system uses stainless steel tubing, and most of our joints use Swagelok VCR fittings. The mixing tank has a bellows sealed valve instead of a traditional gas tank valve, and the VCR connection to this valve is brazed into a brass plug soldered in the top of the tank. The mixing tank, tubing, and gauge fittings were all tested with a leak detector prior to mixing. A diagram of the complete AMRR mixing system is shown in Figure 53 in the AMRR mixture procedure below. This section also details the ^{3}He-^{4}He mixture process.

AMRR Mixture Procedure

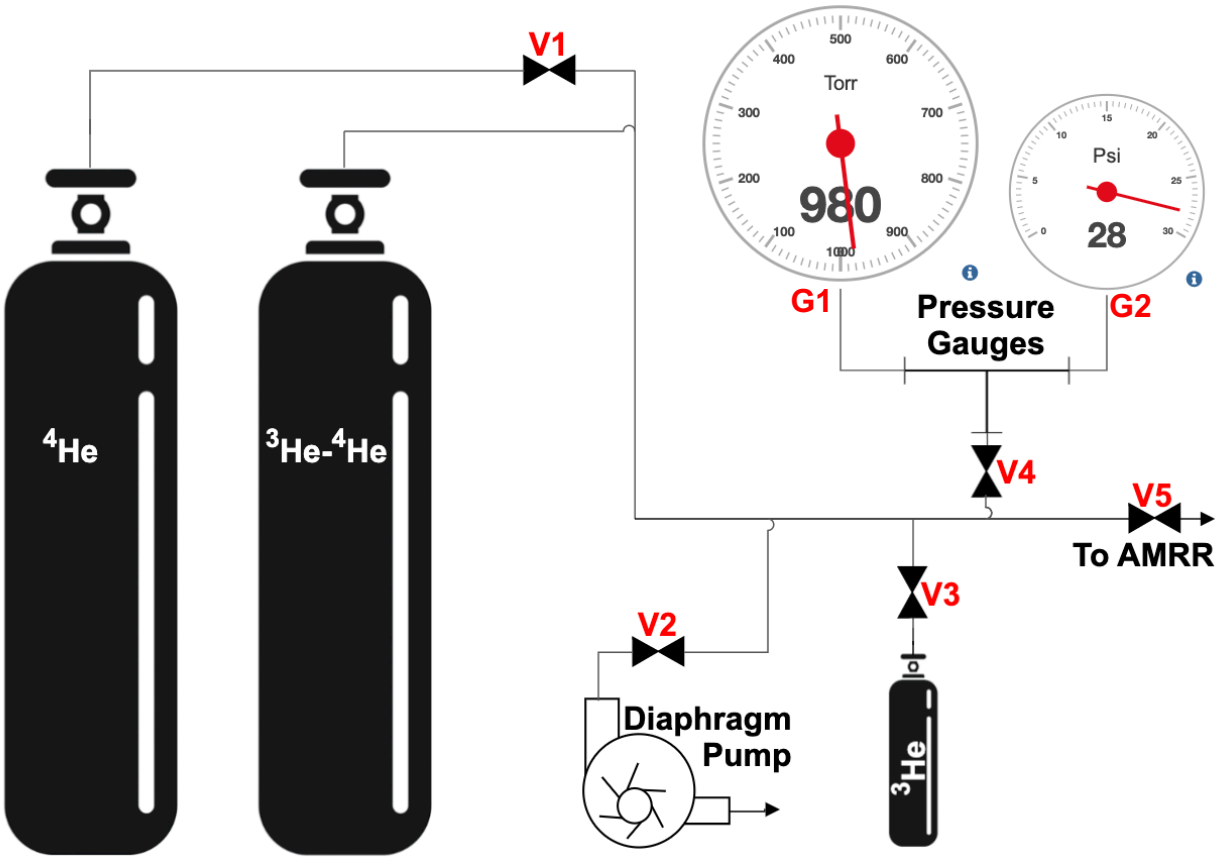

Figure 53. A diagram of the AMRR ^{3}He-^{4}He mixing system.

1. Close all piping valves (V1, V2, V3, V4, V5) and tank valves. Adjust ^{4}He regulator to 5 psi.
2. Ensure ^{3}He tank valve is closed. Open ^{3}He-^{4}He tank valve, V3, and V4 valves.
3. Start diaphragm pump.
4. Open V2 valve to vacuum out fill line and tank. Allow pressure to bottom out.
5. Close V2 valve. Open V1 to pressurize line and tank to 5 psig.
6. Close V1 valve.

7. Repeat steps 4-6 five times to dilute impurities. Close V3 while under vacuum prior to final pressurization step.
8. Open V2 valve slowly to drop pressure on G1 gauge below 500 torr. Turn off diaphragm pump.
9. Determine ^{3}He fill pressure by adding 81 torr to pressure indicated by G1 gauge.
10. Open ^{3}He tank valve to fill line up to V3. Close ^{3}He tank.
11. Quickly open and close V3 and wait for pressure to reach equilibrium.
12. Repeat step 11 until pressure on G1 gauge has reached desired pressure determined in step 9. If ^{3}He pressure in fill line is depleted repeat step 10 with V3 closed.
13. Check that ^{3}He tank and V3 valves are closed.
14. Adjust ^{4}He regulator to 15 psig. Open V1 valve. Continue to increase ^{4}He regulator pressure until G2 gauge reads 30.5 psig.
15. Close ^{3}He-^{4}He tank valve, and all piping valves (V1, V2, V3, V4, V5).

6. AMRR System Experimental Design and Results

6.1 AMRR System Experimental Setup

The AMRR developed in this work is a proof-of-concept system; therefore, the main objective is to demonstrate measurable cooling at the cold end. Experimental design for cryogenic temperatures requires careful selection of proper instrumentation for controlling and monitoring the various system components. To cycle the AMRR system and collect data for system characterization, we developed a LabView program to interface with our equipment. We sourced a range of voltages across a resistive heater on the CHX to measure and control the power into the cold end and placed our thermometry at strategic locations throughout the system to characterize the system response. Through these methods, we were able to control the system and measure cooling power. This section outlines the AMRR experimental instrumentation, design, and results.

6.1.1 AMRR Instrumentation

A variety of instruments are required to measure the thermometry and power the magnets and heaters. Ramping a superconducting magnet requires a power supply for sourcing current and a measuring device for measuring the voltage drop across the leads. This measurement is important for controlling the ramp rate and reducing the current in the event of a quench. For our magnets we use Keithley Source-Measuring Units (SMUs) which simultaneously supply current and measure voltage. An example of a Keithley SourceMeter is shown in Figure 54. The two SMP magnets require a 3 A maximum current, while the AMR magnets require close to 5 A. Because of this, the two SMP magnets use Model 2420, which has a maximum current of 3 A, and the two AMR magnets use Model 2440, which has a maximum current of 5 A. These instruments have an accuracy of 0.012% with 6 ½-digit resolution.

Measuring temperatures in the near and sub-K range requires particular thermometry and instrumentation. Cernox thin film resistance sensors have high sensitivity at low temperatures, excellent stability, and are suitable for use near magnetic fields. Four-wire measurements are used to determine the sensor resistance, which corresponds to a certain temperature. Various Cernox models are available with heightened sensitivity in different temperature ranges. For the AMRR system, we used CX-1010 and CX-1030 sensors which have a reported calibration uncertainty of +/- 4 mK at 1.4K. From the dimensionless sensitivity bands shown in Figure 55, it is clear that these two types of sensors have similar responses at low temperature, though each individual sensor has its own sensitivity curve.

Figure 54. A Keithley SourceMeter, which can be used to ramp superconducting magnets.

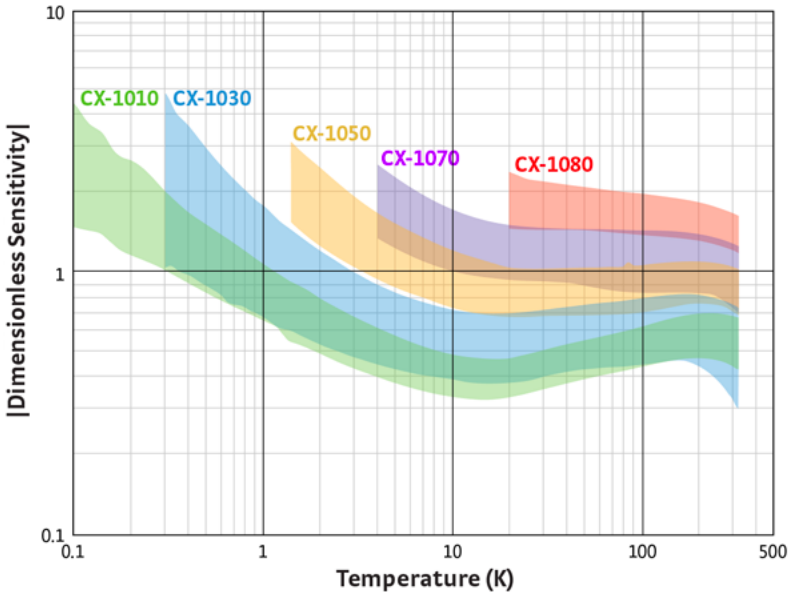

Figure 55. Cernox dimensionless sensitivity as a function of model and temperature.

Cernox calibration curves are unique to each sensor and convert resistance readings into temperatures. These curves can be uploaded into our Cryo-Con 44 temperature controller, which automatically interpolates between curve points to report readings in units of temperature. For taking resistance measurements, the Cryo-Con controller maintains a constant voltage bias across the Cernox sensors and adjusts the AC excitation current to maintain this bias. Constant-voltage measurements minimize the self-heating errors that can otherwise occur at ultra-low temperatures. The reported accuracy for reading NTC resistor sensors like Cernox sensors is 0.05% of the sensor reading + 0.05% of the range. This means that at 1.5 K, the measurement accuracy for the Cryo-Con with one of our Cernox sensors is +/- 5.5 Ω, which translates to +/- 7.5 mK.

The Cryo-Con temperature controller also has control loops which can be used to power the two 50 Ω heaters in the AMRR system. The heater for the HHXs needs to hold the pre-cooling stage at a controlled temperature that is near 1.5 K. This power can be manually adjusted until the appropriate temperature is reached. The heater for the CHX can be controlled similarly, with the separate objective of applying a specific rate of heat transfer into the cold end of the system; the desired cold end heat input is typically between 0-1 mW. An accurate measurement of the power into the CHX is crucial for properly characterizing the refrigeration system. Because the Cryo-Con controller in not capable of reporting measurements of power dissipation in the heater, we use an additional Keithley 2700 multimeter to make measurements of the voltage drop across the heater. We take an initial resistance reading of our heater prior to cycling the AMRR and then determine the CHX power using the voltage measurements. This resistance reading is necessary for accurate power calculations because resistance can be a strong function of temperature. We found the heaters we used had low temperature sensitivity; the resistance change between room temperature and 1 K was only ~0.2 Ω. The 2700 multimeter can read resistances within +/- 0.014% and voltages

within +/- 0.0037% in the ranges required for our application. An image of the Keithley 2700 Multimeter is shown in Figure 56 below.

Figure 56. The Keithley 2700 Multimeter used to take voltage measurements across the CHX.

6.1.2 AMRR LabView Program

Though cycling the AMRR system is complex, LabView has the capabilities to meet the operation requirements. That is, LabView can independently ramp the four system magnets to meet a desired cycle time, control the two system heaters to meet temperature and power targets, and record multiple temperatures from the thermometry placed around the system. An image of the LabView program during AMRR cycling is shown in Figure 57 The upper left green box contains the starting cycle parameters: max pump current, max AMR current, NF current, cycle time in seconds, and the flow delay in seconds. Here, the NF current represents the current the regenerator magnets should reach during the no flow processes, and the flow delay represents the length of the no flow processes. Below the AMRR System Start box, there are two graphs recording the current supplied to each of the four magnets as a function of time. The compliance voltage for each magnet was separately specified such that the magnet would ramp to the desired current in the specified time.

In the center column, there is a diagram of the system with temperature information as well as a plot of the temperatures. We placed seven Cernox thermometers around the AMRR system: one on each SMP, one at the top and bottom of each regenerator, and one at the HHX.

In the purple box on the top right is the AMRR heater control for controlling the CHX and HHX heaters. This allows for the heaters to be turned on and off and adjusted to meet the previously explained temperature and power targets. A graph of the CHX power is also displayed here, which is a function of the CHX heater resistance. This resistance can be updated from the front panel to reflect the resistance measurements taken prior to each cycle. Finally, a plot of the housekeeping thermometry is shown on the bottom right which tracks the temperatures of different stages within the cryostat. This program records all the temperatures, heater control settings, AMRR cycle settings, and magnet currents as a function of time.

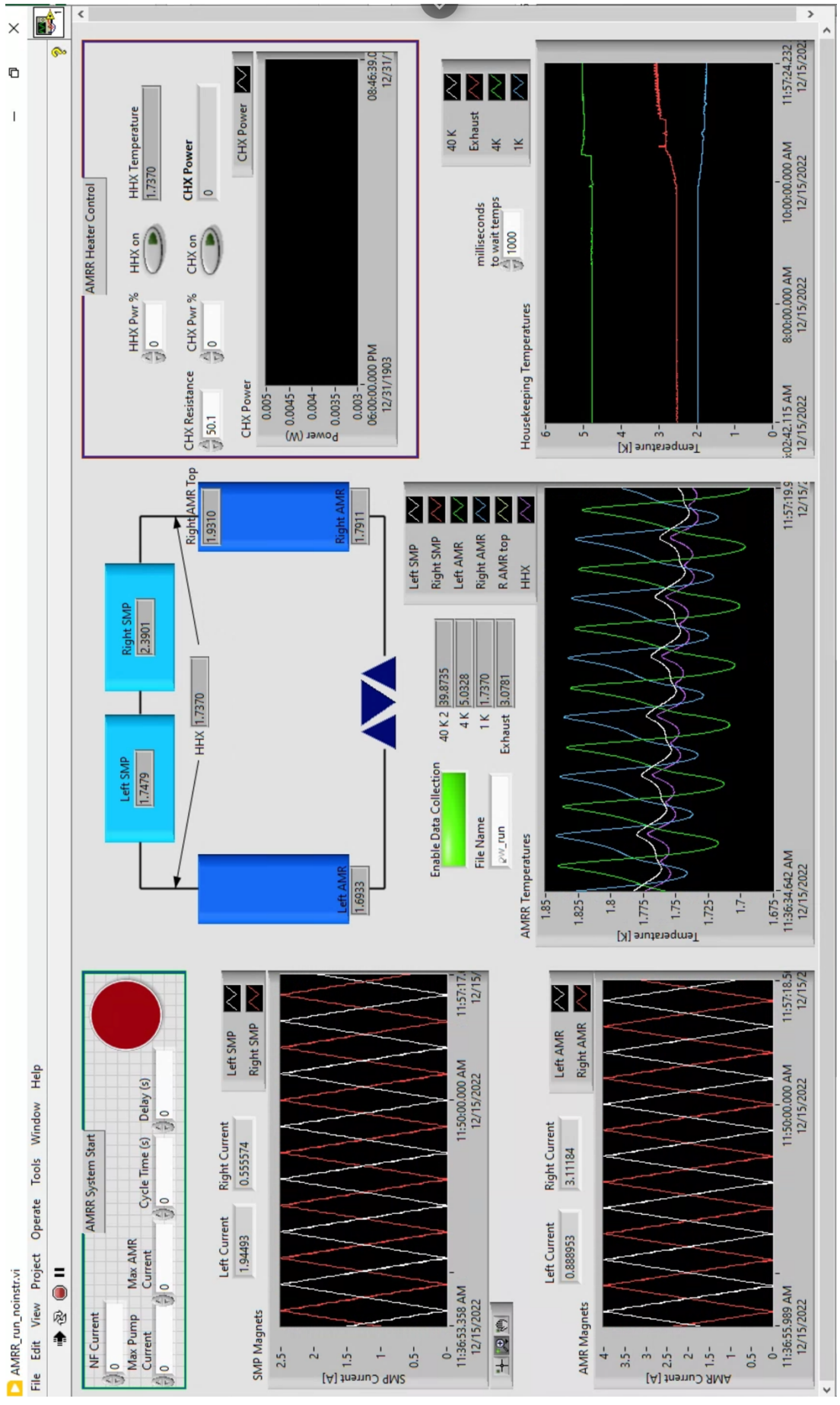

Figure 57. LabView program for controlling the AMRR system and recording data for system characterization.

6.1.3 Experimental Design and Procedure

The AMRR system configuration is shown in Figure 58. This diagram does not include extraneous components such as the 1 K pot fill and pump lines and the cryocooler. The four canisters are mounted horizontally in the Dewar and the tubing is configured such that one SMP and the "opposite side" AMR are vertically stacked to minimize destructive magnet interference. The locations of the seven main system Cernox thermometers are indicated by the small orange tabs and CX-X labels in the diagram.

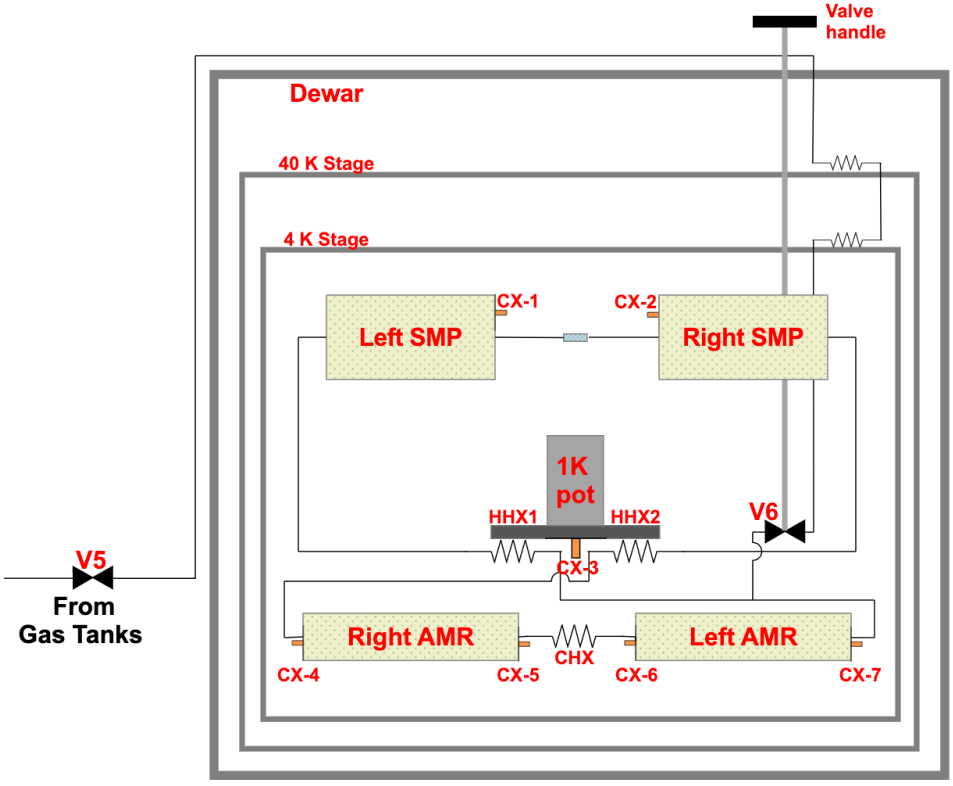

Figure 58. A diagram of the AMRR setup within the Dewar.

Room temperature ^{4}He or ^{3}He-^{4}He gas enters the Dewar through a vacuum port at the top and is precooled through multiple heat exchangers as it flows towards the AMRR loop. Once the 1K pot begins to condense ^{4}He and provide cooling to the 1 K platform, the helium in the AMRR loop begins to condense and subcool. The pressure in the AMRR fill line is kept at approximately 2-3 psig during the condensing process. Once the temperatures within the loop reach equilibrium

with the 1 K platform, the AMRR loop is fully charged. Typically, the canisters will equilibrate around 2 K while the 1 K platform is at 1.2 K. At this point, the Nupro Valve (V6) is closed using the drive shaft that runs through the vacuum space and the back of the fill line is pumped out to prevent thermal shorts between the AMRR system and the 4 K platform. The SMP is then cycled to displace fluid through the HHXs at the 1 K platform and further cool the system to approximately 1.4 K. The LabView program is then used to then cycle the full AMRR system, allowing us to adjust system parameters and record system performance over a range of HHX temperatures for different operating parameters.

A diagram of both the external AMRR gas handling system and AMRR system within the Dewar is shown in Figure 59. The procedures for system cooldown, experimental runs, and warmup are outlined beginning on the page following this diagram.

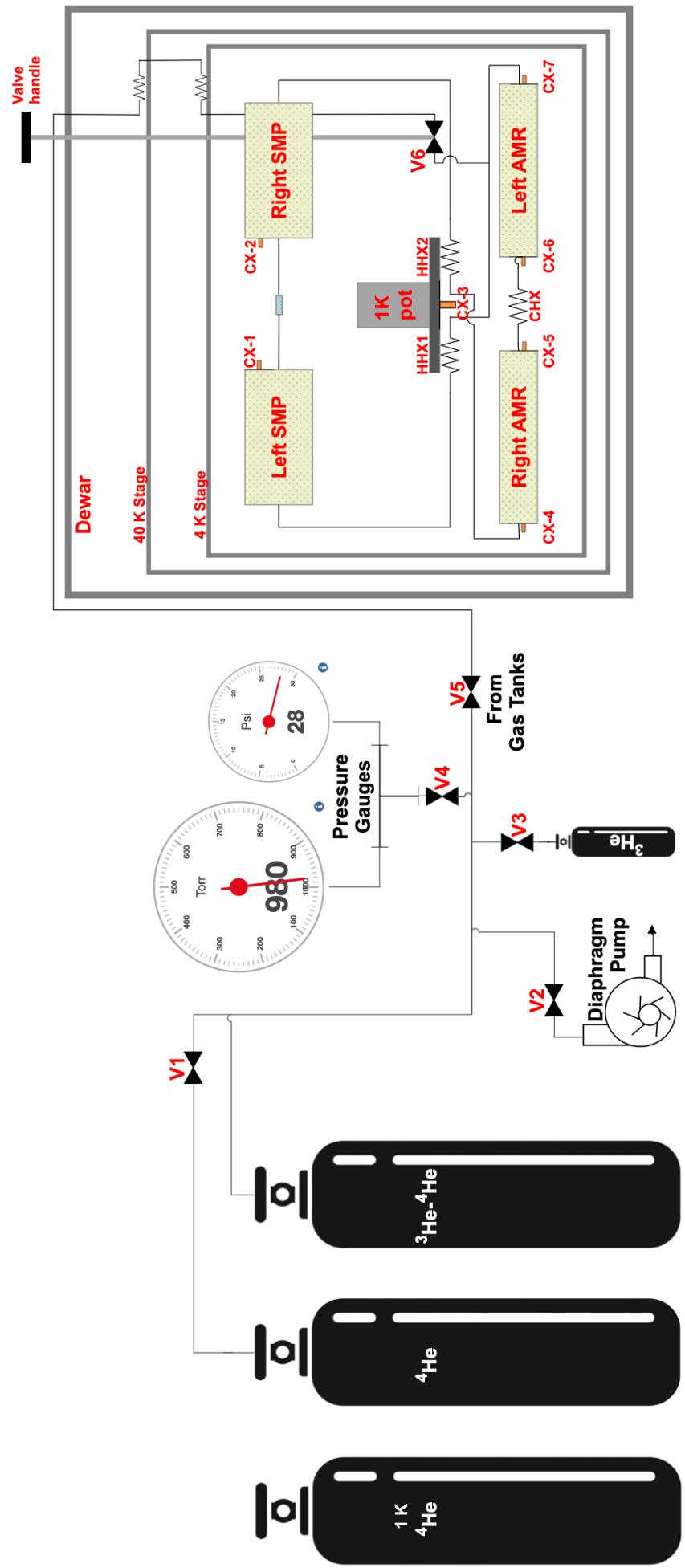

Figure 59. A diagram of the AMRR gas handling system and AMRR system within the Dewar.

AMRR Cooldown Procedure

If AMRR loop has been exposed to atmosphere since prior cooldown, AMRR system will be charged with ^{4}He to check for superfluid leaks:

1.1 Close all piping valves (V1, V2, V3, V4, V5, V6) and the ^{3}He-^{4}He tank valve. Adjust regulator on ^{4}He tank to 5-10 psig and ensure the tank has enough helium to fill AMRR system (>75 psi).

1.2 Start diaphragm pump (the one attached to the AMRR gas line).

1.3 Open V5 and V6 valves to allow for vacuuming and filling AMRR system.

1.4 Open V2 valve (to diaphragm pump). Allow pressure to bottom out.

1.5 Close V2 valve.

1.6 Open V1 valve (near ^{4}He tank) to pressurize line and system to 5-10 psig.

1.7 Close V1 valve.

1.8 Repeat steps 1.4-1.7 seven times to dilute impurities in the system. If this is not done thoroughly, the capillary tubing in the AMRR system could become clogged when cold.

1.8 Adjust regulator on ^{4}He tank to 2-3 psig to fill AMRR system.

If loop is still charged with ^{3}He-^{4}He from prior cooldown:

1.1 Check line pressure and ensure there is enough ^{3}He-^{4}He remaining to fill system (>28 psig).

For both ^{4}He and ^{3}He-^{4}He cooldowns:

2. Check 1 K helium bottle to ensure there is enough helium for a cooldown (>1000 psi). If tank needs to be changed, follow *Preparation of the 1 K pot* procedure outlined in Jahromi's thesis.
3. Adjust 1 K helium tank's pressure regulator to 28-30 psig.
4. Check the low-pressure side and ensure the rotary vane pump inlet pressure is < 30 mTorr.
5. Close vacuum chamber vent and turn on vacuum chamber diaphragm pump.
6. Open pump valve on top of vacuum chamber to begin pumping out chamber.

7. When vacuum chamber pressure reaches < -20 inHg, turn on the Pfeiffer turbopump mounted on the chamber. Keep the diaphragm backing pump on.
8. When vacuum chamber pressure reaches < 1E-3 mbar, the CryoMech PT-410 cryocooler can be turned on. The cooling water loop should be checked for flow, and the water filters should be replaced every 2-3 weeks of flow time.
9. Begin **AMRR_run_full.vi** LabView program to record temperatures. Enter a file path and turn on "Enable data collection". Change "milliseconds to wait" to 300000.
10. Monitor temperatures and vacuum chamber pressure during cooldown. Note the vacuum chamber pressure before and after the system reaches 2 K. If the pressure rises, there is likely a superfluid leak in the system (>5E-8 mbar). The backside pressure of the 1 K pot should increase to ~200-500 mTorr at base temperature. If the pressure is lower than this and helium will not condense into the 1 K pot, slowly increase inlet pressure until the 1 K platform temperature drops below 4 K.
11. If the vacuum pressure goes up once the system drops below 2.17 K, the system must be warmed up to fix the superfluid leak. Skip to *AMRR Warmup Procedure.* If all temperatures around the system are below 2.17 K and the pressure has remained constant over the course of ~12 hr, the system can be assumed to be superfluid tight.

If AMRR loop was initially charged with ^{3}He-^{4}He mixture:

12.1 Close V6 valve with handle. Take care not to shear drive shaft, but ensure valve is tightly sealed.

12.2 Close ^{3}He-^{4}He mixture tank valve.

12.3 Check to make sure AMRR diaphragm pump is still on. Open V2 valve to vacuum out AMRR system fill line up to closed AMRR loop. Keep fill line under vacuum. Let system temperatures bottom out.

If AMRR loop was initially charged with ^{4}He:

12.1 Check to make sure AMRR diaphragm pump is still on. Open V2 valve to begin to vacuum out AMRR system.

12.2 Close valve on 1 K helium tank regulator to cut off helium supply to the 1 K pot.

12.3 Allow ^{4}He to slowly boil off (~1 day). Track canister temperatures to verify boiloff.

12.4 Once all AMRR system temperatures and 1 K pot temperature are above 4.5 K, AMRR system is considered to be empty. Close V2 valve to diaphragm pump.

12.5 Slowly crack V3 valve on the ^{3}He-^{4}He mixture tank to introduce some gas into the line. Watch temperatures of AMRR system and Dewar stages. Wait for temperature to equilibrate before introducing more gas.

12.6 Continue to introduce gas slowly until V3 valve can be left open without causing a thermal reaction.

12.7 Open valve on 1 K helium tank regulator to reintroduce gas to 1 K pot.

12.8 Allow ^{3}He-^{4}He mixture to condense into AMRR system (~1 day). When all temperatures around the system reach base temperature (~2 K), system is full.

12.9 Close V6 valve with external handle. Take care not to shear drive shaft, but ensure valve is tightly sealed.

12.10 Close ^{3}He-^{4}He mixture tank valve.

12.11 Check to make sure AMRR diaphragm pump is still on. Open V2 valve to vacuum out AMRR system fill line up to closed AMRR loop. Keep fill line under vacuum. Let system temperatures bottom out.

AMRR Experimental Procedure

1. Check AMRR loop temperatures to ensure that all temperatures are near 2 K.
2. Adjust AMRR cycle parameters in top left corner of AMRR_run_full.vi to run the SMP by setting the SMP to full range (2.75 A) and the AMR currents to a small value (<0.005 A). There should be no "No-Flow Delay".
3. Change "milliseconds to wait" to 1000 and choose new file path name to describe specific cycle.
4. Turn on the AMRR system to begin to displace fluid through the HHX and bring the system into thermal equilibrium.
5. Prior to supplying power to the CHX heater, use the multimeter to measure the resistance to appropriately capture any shift in resistance at low temperature. Enter this measurement into the resistance box in the top right of the Labview program.
6. Once the AMRR temperatures are consistent with the HHX, you can start to adjust the cycle parameters. To change cycle parameters, you must turn off the AMRR system and let the magnets ramp back down to 0 A before restarting the system with new parameters. To record power measurements, turn on the CHX.
7. System must be turned off and all magnets need to be at 0 A before moving to *AMRR Warmup Procedure*.

AMRR Warmup Procedure

If AMRR loop is charged with ^{3}He-^{4}He mixture:

1.1 Close V2 valve to diaphragm pump.

1.2 Open V6 low temperature valve using external handle (~1/4-1/2 turn).

1.3 Slowly crack ^{3}He-^{4}He tank valve to system line to introduce a bit of mixture. Watch the temperatures around the AMRR system loop and at the 1 K platform to avoid rapid boil off. Let temperatures equilibrate before introducing more mixture.

1.4 Continue to slowly introduce mixture until tank valve is fully open. Leave valve open to allow mixture to re-enter tank during warmup.

If AMRR loop is charged with ^{4}He:

1.1 Ensure diaphragm pump is on and V2 is open. Open V6 low temperature valve using external handle (~1/4-1/2 turn) to begin pumping on system. The ^{4}He will be pumped out and not collected.

If AMRR loop is charged with either ^{4}He or ^{3}He-^{4}He mixture:

2. Close valve on 1 K helium tank regulator to cut off helium supply to 1 K pot.

3. Allow system to slowly boil off (~1 day). Keep cryocooler on.

4. When all temperatures are > 5.5 K, turn off cryocooler and cryocooler water supply. Allow system to slowly warm back up to room temperature.

6.2 AMRR Experimental Results

Once the mixture had condensed into the AMRR system, we ran the SMP to help circulate and cool the mixture through the HHXs. This step is significant because the SMP is a novel technology which has:

1. never been run with two active canisters (during the initial development and demonstration of the pump, one of the SMP magnets was not functional), and
2. never been demonstrated with a ^{3}He-^{4}He mixture.

A graph showing the system response to initially cycling the SMP is shown in Figure 60. The steady state temperatures are shown in the first ~100 s. The AMRR temperatures range from 1.75 K to 2.07 K, and the HHX is at approximately 1.2 K. Evidence of the SMP displacing fluid around the system loop can be seen by looking both at the temperature swings at the top ends of the AMRs, and at the thermal pulses that are evident at the HHX as heat is rejected by the displaced fluid. At this point, the AMRs were not being cycled.

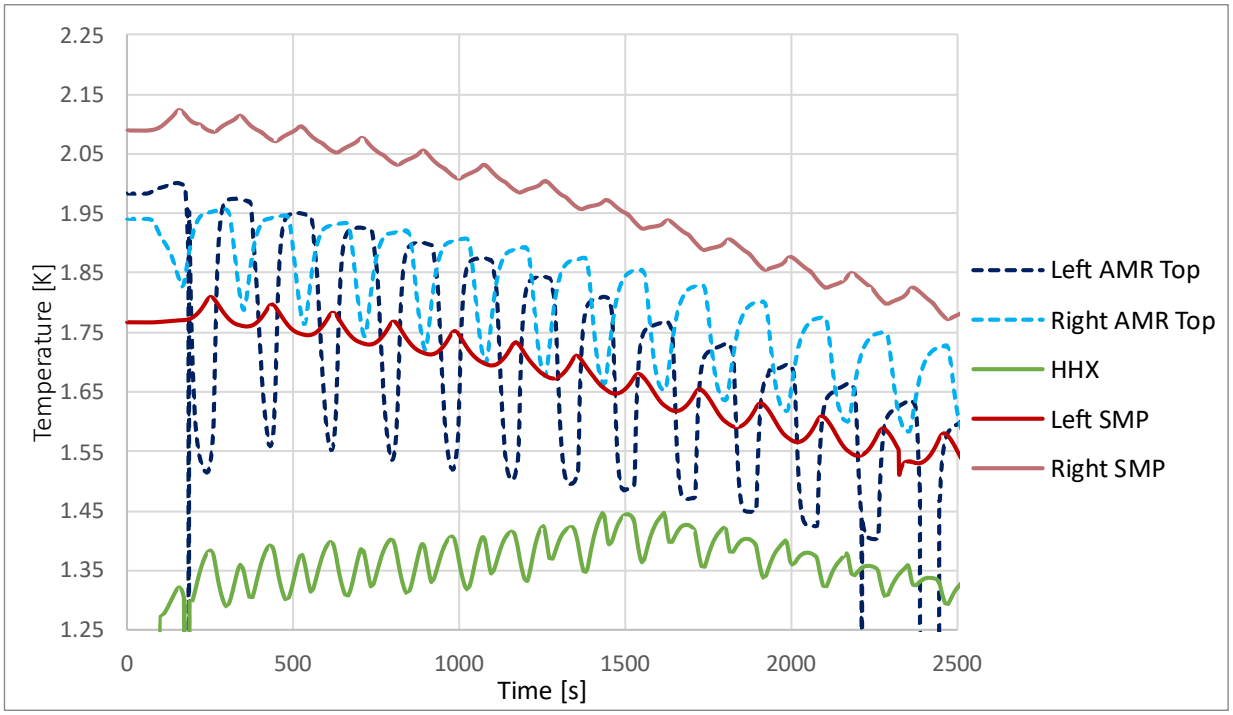

Figure 60. AMRR system response to SMP cycling from steady state.

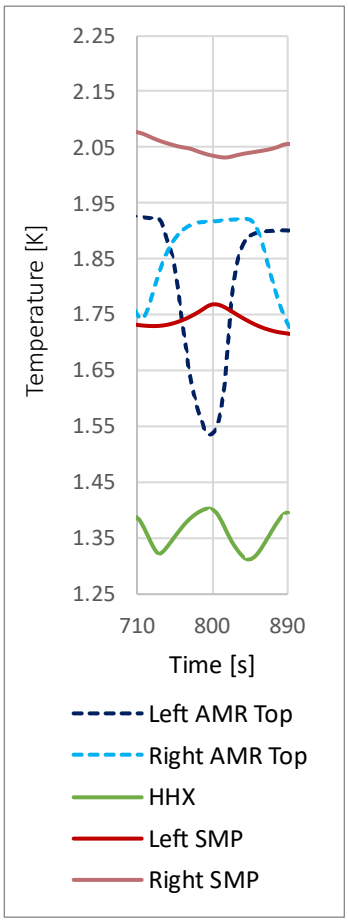

Figure 61. Subsection of SMP cycle response.

A one-cycle subsection of Figure 60 is shown in Figure 61. Here, one complete cycle is 180 s (90 s of flow in both directions). When the left SMP magnetizes, fluid is pushed out and displaced through the HHX and then down through the top of the left AMR. Examination of Figure 61 makes it clear that when the left SMP is warming, the top of the left AMR is indeed cooling. This fluid is displaced down through the left AMR, across the CHX, and up through the opposite right AMR, raising the temperature of the top of the right AMR as it has picked up heat around the loop. The fluid then rejects this heat into the HHX as it is flows into the right SMP. We can see the associated rise in the HHX temperature. After 90 s, the right SMP begins warming and displaces the fluid in the opposite direction, cooling the top of the right AMR and rejecting heat to the HHX after moving through the remainder of the loop.

We let the SMP run until the temperatures around the AMRR system reached a quasi-steady state. We then began cycling the AMRs and adjusting cycle parameters to roughly optimize the system. These parameters include the field swings of the regenerators during the no-flow and flow processes, the field swings of the SMPs during the flow processes, and the length in time of each of the processes. To lift entropy, the AMR bed needs to be warmer when the fluid flows up to the HHX than when it flows down to the CHX, thus the no-flow processes are critical for lifting heat from the cold end of the system as they drive this shift in temperature. Because of this, most of our parameter adjustments were related to the no-flow field swings and process times. Additionally, we fine-tuned the field swings of each canister to roughly match the amplitudes of

the temperature swings between the SMPs and between the AMRs. Our final system parameters are shown in Table 9. The full cycle time is the time to return the system to its initial state; it includes two no-flow and two flow processes. The no-flow time is the length of one no-flow process. The maximum and no-flow currents represent the maximum and no-flow current swings. Estimates of the associated field swings in the AMR magnets based on the magnet geometries are provided in Table 10. The difference between the current swings in the SMPs is largely due to differences in the SMP magnet geometries; the right SMP has approximately half the number of turns as the left SMP. The difference between the current swings in the AMRs, however, is most likely due to a large parasitic heat leak into the right AMR. To compensate for this heat load, we used higher current swings in the right AMR.

Table 9. AMRR cycle parameters.

Parameter	Full Cycle Time [s]	No-Flow Time [s]	Max Current [A]				No-Flow Current [ΔA]	
			Left SMP	Right SMP	Left AMR	Right AMR	Left AMR	Right AMR
Value	210	50	2.75	4.8	3.0	3.75	2.75	3.45

Table 10. Estimated AMR field swings.

Estimated Max Field [T]		Estimated No-Flow Field Swing [ΔT]	
Left AMR	Right AMR	Left AMR	Right AMR
0.91	1.14	0.83	1.05

Using the parameters reported in Table 9, we began cycling the AMRR system to characterize the system. Figure 62 shows AMRR temperatures as a function of time over approximately 5 cycles with a HHX temperature of 1.53 K. The bottom end AMR temperatures are the lowest temperatures in the system, consistently below their respective top end temperatures;

this indicates that the AMRs were providing cooling to the mixture as it flows to the CHX and proves that a superfluid ^{3}He-^{4}He AMRR system is conceptually sound.

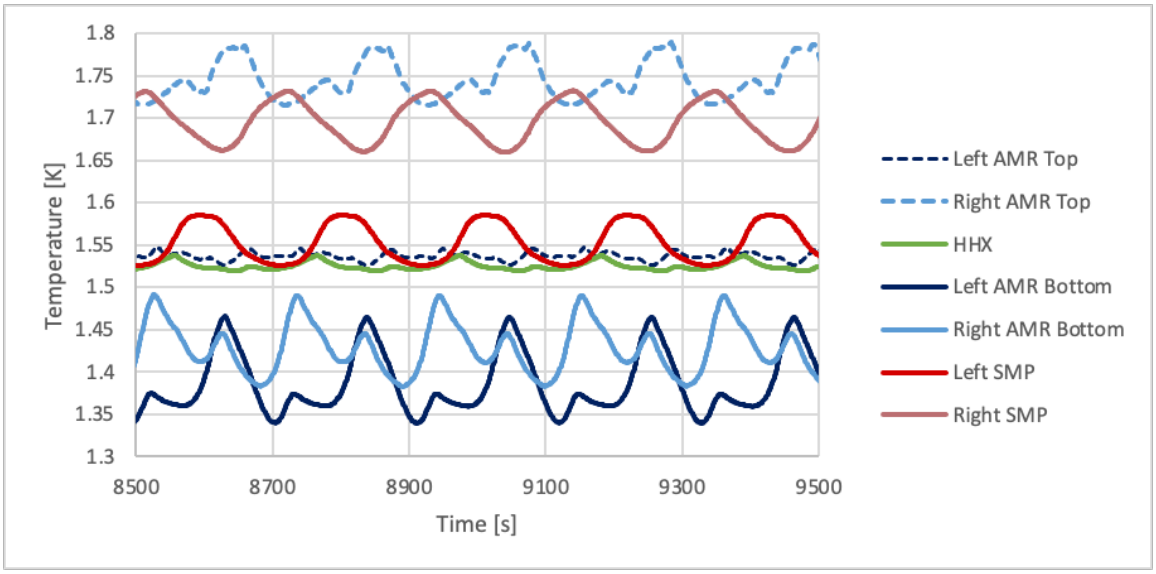

Figure 62. Temperatures in the AMRR system as a function of time.

The temperatures of the left SMP and the top of the left AMR were close to the HHX temperature, which is designed to be the system high temperature. The temperatures of the right SMP and the top end of the right AMR, however, were significantly warmer than the HHX. This suggests the existence of a significant and unknown parasitic load on the right side of the system. There is likely a small superfluid leak at the top of the right AMR that is thermally shorting the canister to the 4 K brackets across the Kevlar. Though the AMRR system could still provide measurable cooling, the cooling power was much lower than predicted and we could not reach the design base temperature of 750 mK. However, as a proof-of-concept system, the demonstration of cooling is the primary objective.

To generate AMRR cooling curves, we held the HHX temperature constant at 1.40 K and 1.53 K while sourcing a range of voltages across the 50 Ω CHX resistor to vary the cooling power. It took at least 3 hours at each power to reach a steady state operating condition. To provide an

easy comparison, Figure 63 and Figure 64 show side-by-side AMRR temperature variations for single quasi-steady state cycles at each of the six different heat loads. The temperatures of the SMPs and HHXs are relatively unaffected by the CHX loads as expected. The top ends of the AMRs drifted up a bit as more heat was applied at the CHX, but the main difference is seen at the bottom ends of the AMRs.

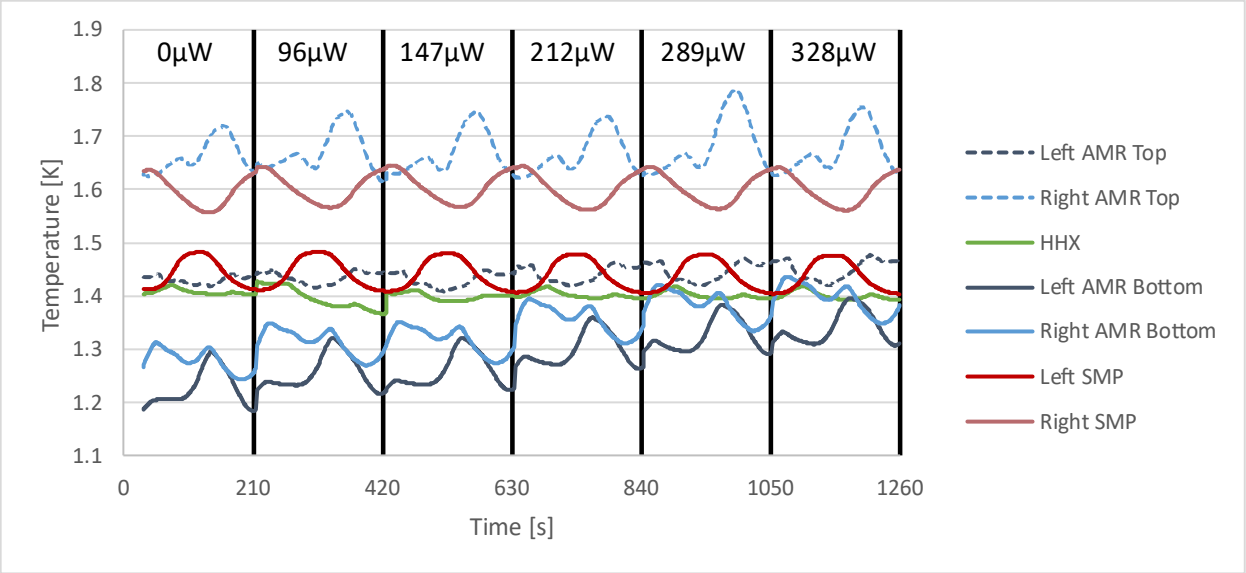

Figure 63. AMRR steady state temperatures for six different CHX loads while HHX is kept at 1.40 K.

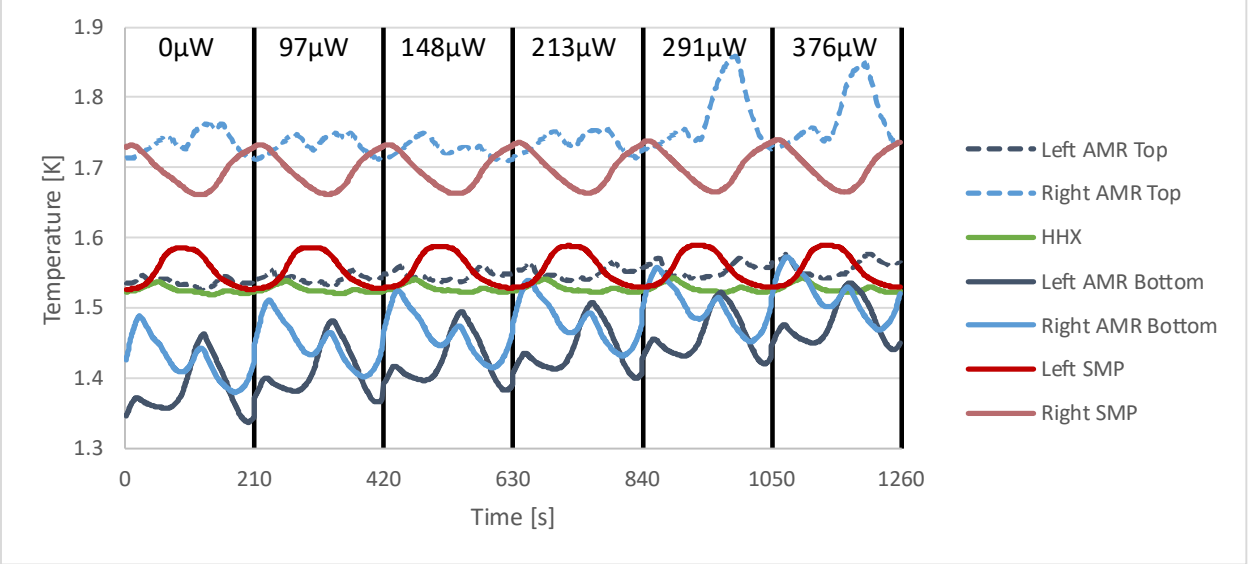

Figure 64. AMRR steady state temperatures for six different CHX loads while HHX is kept at 1.53 K.

Because of the significant parasitic heat load into the right regenerator, the two AMRs reject heat to different temperatures and therefore quantifying system performance is not straightforward. To address the difference between these reject temperatures, we calculated an "effective" reject temperature by estimating the heat rejected at each AMR top end temperature, and then equating the entropy flows associated with these two heat rejections in order to define an effective heat rejection temperature:

$$\frac{Q_{right}}{T_{right,AMR,top}} + \frac{Q_{left}}{T_{left,AMR,top}} = \frac{Q_{right} + Q_{left}}{T_{effective}} \tag{24}$$

To estimate the heat rejected at the HHX for the right and left sides of the system, we first estimated the flow rates during the "flow" processes. To do this, we needed to determine the ^{4}He chemical potential (μ_4^0) at the beginnings of both the counterclockwise and clockwise flows to determine thermodynamic properties using our measured temperatures. We used an initial estimate of ^{3}He moles in the system based on the concentration of our mixture and the volume of the AMRR system and found the μ_4^0 values required to conserve ^{3}He moles given the AMRR temperatures at the beginnings of the flow processes. We assumed a linear temperature profile along the AMRs between the average bottom and average top temperatures over the flow processes. Through this method, we could determine the moles of mixture displaced from the pump during a flow process, and the associated heat rejected between the top of an AMR and an SMP canister. We found that the effective rejection temperature is 1.63 K for the cases run with the HHX at 1.40 K, and 1.72 K for cases with the HHX at 1.53 K. The estimated mass flow rates as a function of CHX power and effective AMRR reject temperature are shown in Figure 65. For comparison, measured flow rates from the SMP are shown in Figure 66, which is taken from Jahromi and reports measured the flow rates of pure ^{4}He with just one pump canister operating [16]. We used an effective ramp rate voltage of approximately 0.3 V for our left SMP, which is the same magnet and canister used to

generate the curves shown in Figure 66. The estimated flow rates are on the same order of magnitude as the previously measured flow rates, though 3-4 times lower than previous measurements. Most of the discrepancy is likely due to the assumption of linear temperature profiles along our regenerators in our estimate.

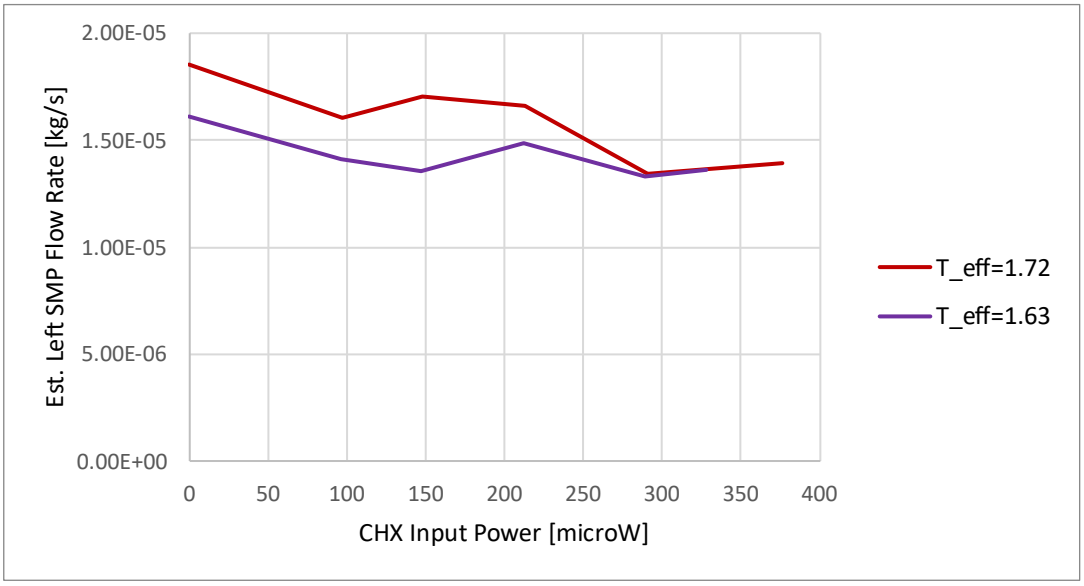

Figure 65. Estimated mass flow rates in AMRR as a function of CHX input power and effective system rejection temperature.

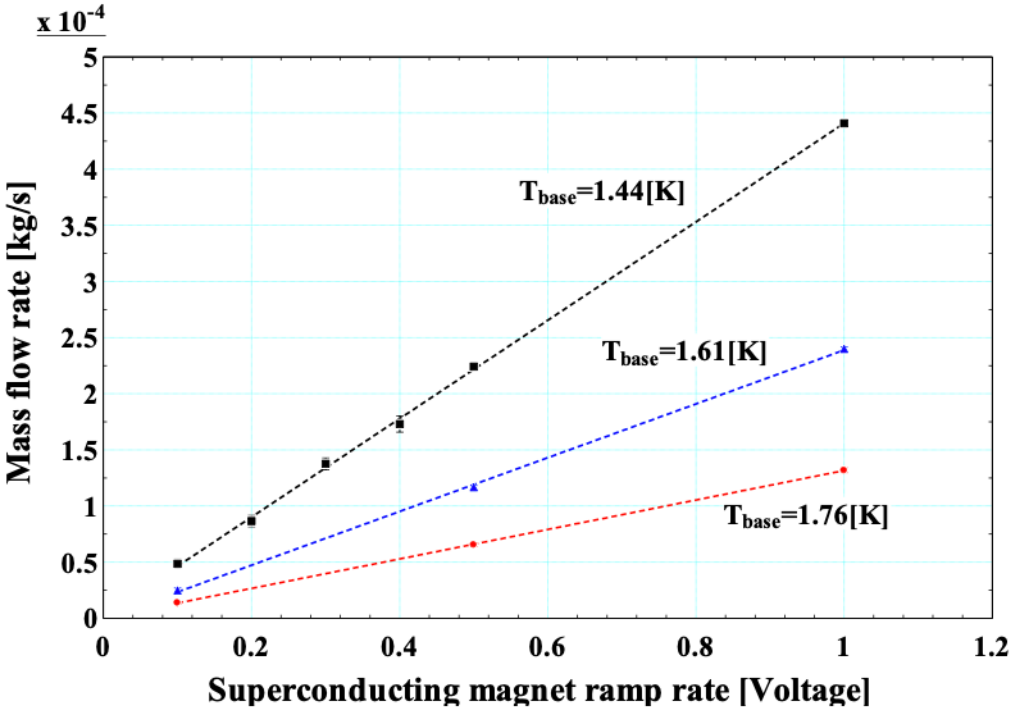

Figure 66. SMP measured mass flow rate as a function of base temperature and ramp rate [13].

Given the estimated flow rates and temperatures across the HHX, we could calculate the heat rejected on each side of our system. Figure 67 shows these estimated heat loads. The right side of the system, which has the large parasitic load, has an estimated heat rejection of several milliwatts while the left side of the system has much lower estimates in the hundreds of microwatt range. The left side shows the expected increase in heat rejection as the power into the CHX is increased.

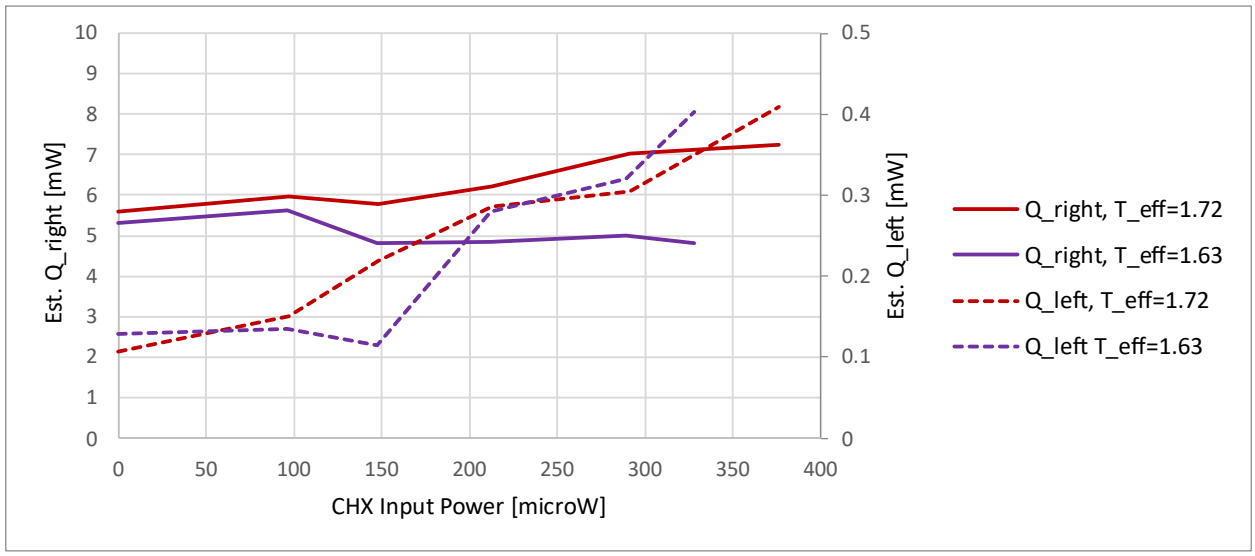

Figure 67. Estimated heat rejected at the HHX on the right and left sides of the AMRR system.

Using the effective reject temperatures we calculated, we generated cooling power curves for the AMRR system at two separate temperatures. These curves are shown in Figure 68, which also shows the individual power curves for the AMRs with associated uncertainty. As explained before, the AMRR system did not provide the initially predicted cooling power nor reach the predicted base temperature because of the large parasitic heat load, so these curves are not representative of the full capacity of the AMRR system and cannot be directly compared to

previous models. They provide an operation baseline and demonstrate that the AMRR can provide distributed cooling via circulation of a ^{3}He-^{4}He mixture using a non-moving SMP.

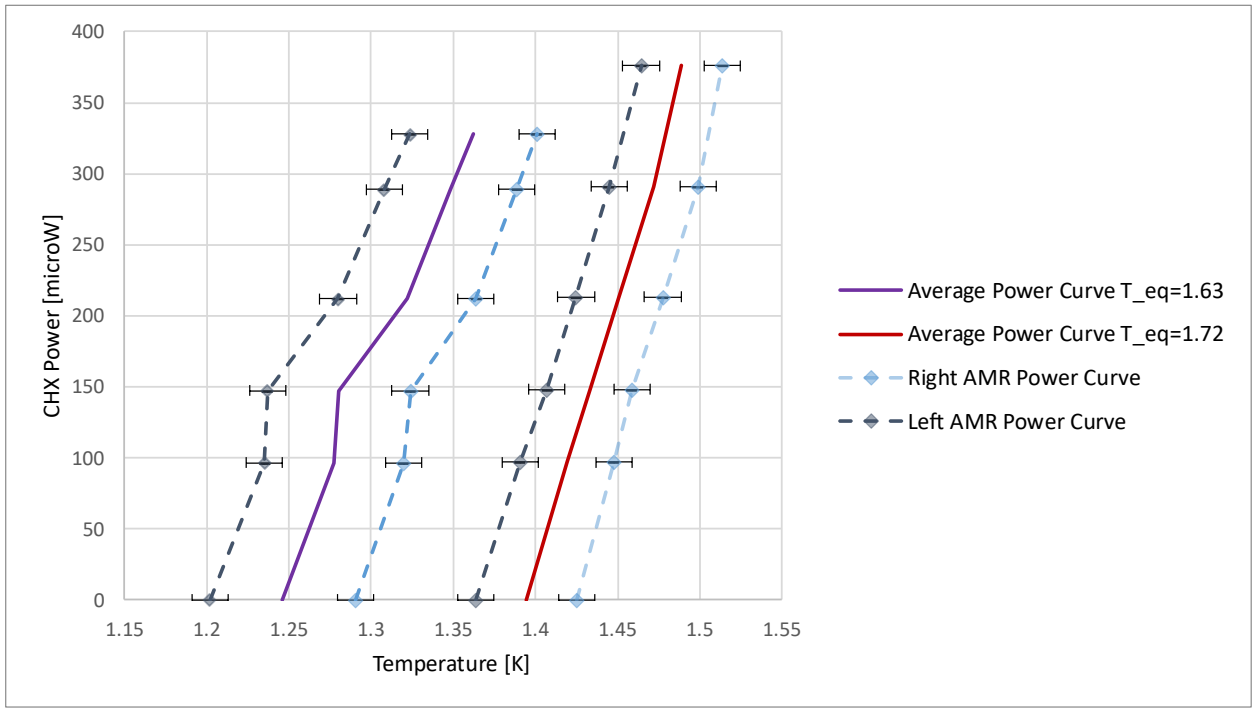

Figure 68. AMRR cooling power curves.

We also examined the temperatures of the SMP and AMR canisters relative to the cycling of each canister's respective magnet. These graphs are shown in Figure 69 and correspond to the AMRR cycles captured in Figure 62. The top two graphs correspond to the left and right SMP field and temperature swings. The magnetic field plateaus at the maximum and minimum currents are the "no-flow" periods where the pump canisters would ideally maintain constant temperatures and therefore not produce flow through the regenerators. In practice, this is not entirely true because the mixture is not perfectly thermally coupled to the GGG particles, and the canisters are not thermally isolated from the system as the mixture can move freely into or out of the canisters. For the parameters we used, the SMP canister temperatures continued to increase/decrease once the current became constant likely due to the small boundary layer resistance between the mixture and

particles. The heat capacities of the stainless steel canisters and contact resistances between the canisters and thermometry could also be contributing to the measured thermal delay. The total temperature swings, along with the "no-flow" temperature swings are provided in Table 11. Future work optimizing the system could minimize these "no-flow" temperature swings through adjusting the SMP magnetic fields to counteract the temperature drifts.

Table 11. SMP total temperature swings and "no-flow" temperature swings.

	ΔT_{total} [K]	$\Delta T_{NF,high}$ [K]	$\Delta T_{NF,low}$ [K]	$\frac{\Delta T_{NF,high}}{\Delta T_{total}}$	$\frac{\Delta T_{NF,low}}{\Delta T_{total}}$
RSMP	0.0727	0.0294	0.0320	40.43%	43.98%
LSMP	0.0592	0.0324	0.0149	54.69%	25.26%

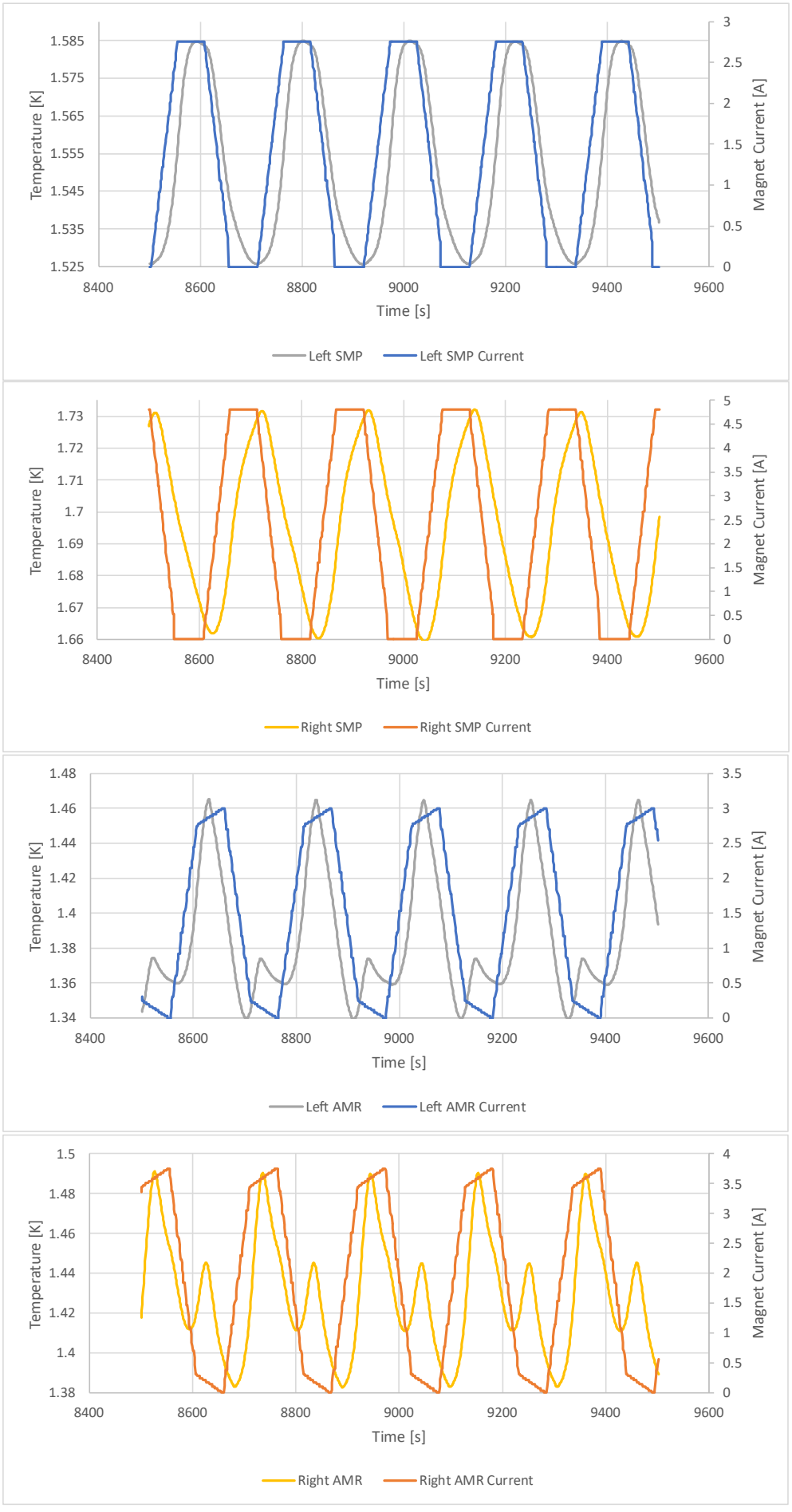

Figure 69. The temperatures and currents of each SMP and AMR.

7. Conclusions and Future Work

This work is focused in part on the development and validation of an improved CCA thermodynamic model. Inclusion of the ZFS term in this model resulted in improved qualitative agreement with experimental data compared to the isolated paramagnetic spin model, though it does not fully capture the severe reduction in cooling capacity below 100 mK. The remaining difference between observed and predicted magnetic behavior could be due to several factors. There may be one or more significant low-temperature interactions that are unaccounted for, such as magnetic dipole interactions or exchange interactions. Alternatively, there may be systematic errors in the data collection methods or other losses. New measurements are required to understand if the remaining discrepancy between the model and data is a systematic effect or a fundamental feature of the salt.

ZFS is also significant in other alums such as CPA, which has an effective ZFS D parameter that is greater in magnitude than that of CCA, resulting in a greater reduction in predicted heat capacity at reduced temperature [6, 44, 45]. Though out of the scope of this work, further exploration of ZFS parameters for different alums would be beneficial for improved material characterization and selection for the lowest temperature CADR stages. A summary of completed and future CCA model development milestones are provided in Table 12.

This research is also dedicated to the design and development of a complete proof-of-concept AMRR system using GGG as the refrigerant with a ^{3}He-^{4}He working fluid. Though the utilization of the magnetocaloric effect for low temperature refrigeration is not novel, the combination of this technique and the exploitation of exceptional near Kelvin helium properties to provide distributed sub-Kelvin cooling with no moving parts is truly unique. The AMRR system

designed and developed in this work successfully provided distributed cooling to below 1K and is therefore the first demonstration of this type of system.

Future work includes finding and mitigating the parasitic heat leak, validating the system model, and optimizing the system. The joints in the right AMR regenerator should be redone and tested for superfluid leaks prior to reintegration with the system loop. Once the regenerator is shown to be leak tight, the AMRR system can be rebuilt and new load curves should be produced. The updated power curves will more accurately reflect the capabilities and performance of the system and can be used for model validation. After a robust system model has been developed, work can begin on system optimization. There are a variety of parameters that should be examined, including but not limited to cycle timing and field swings, regenerator material, and magnet design. Many of the cycle parameters have already been discussed at length in the AMRR results chapter, but a validated system model will make it easier to examine this parameters space more efficiently. A future iteration of the system could use GLF as the refrigerant in the regenerators, which would allow the system to provide cooling to lower temperatures than with the GGG. Also, future iterations could include redesigned magnets with more intricate winding geometries to counteract the edge effects seen at the ends of basic solenoids. Once optimized, this system could be used on space-flight missions to precool lower temperature CADR stages or for distributed cooling over large detector arrays, offering an improvement over current systems and making new types of cryogenic refrigeration configurations possible. Major AMRR milestones are provided in Table 12.

Table 12. A summary of research milestones.

Project	Milestones
CCA	Developed Python model based on complete spin Hamiltonian
	Examined effects of different splitting parameters on thermodynamic properties – specifically hyperfine and ZFS
	Examined differences between developed model and other current models – isolated paramagnetic spin and Brillouin
	Used least-square regression to fit the model to experimental data sets for two different salt pills
AMRR	Designed remaining system components relative to existing SMP – namely the regenerator canisters and magnets and CHX
	Constructed the remaining AMRR components
	Installed AMRR components and suspension in the cryostat
	Designed helium mix fill procedure
	Mixed ^{3}He-^{4}He gas mixture
	Developed LabView control program for magnets, heaters, and data collection
	Filled and tested AMRR system
	Analyzed experimental data to characterize system

References

[1] P. Shirron, *Chloe Gunderson NSTRF Progress Report,* 2018.

[2] P. Debye, "Einige bemerkungen zur magnetisierung bei tiefer temperatur.," *Annalen Der Physik,* vol. 386, pp. 1154-60, 1926.

[3] W. F. Giauque, "A thermodynamic treatment of certain magnetic effects. A proposed method of producting temperatures considerably below 1 degree absolute.," *Journal of American Chemistry Society,* vol. 49, pp. 1864-70, 1927.

[4] P. Shirron, D. Wegel, M. DiPirro and S. Sheldon, "An adiabatic demagnetization refrigerator for continuous cooling at 10 mK and below," in *AIP Conference*, 2006.

[5] T. D. Black, "Magnetic Measurements on Chrome-Cesium Alum below 1 K," Rice University, 1961.

[6] J. Owen and K. D. Bowers, "Paramagnetic resonance II," *Reports on Progress in Physics,* vol. 18, pp. 304-73, 1955.

[7] N. Rando, D. Lumb, M. Bavdaz, D. Martin and T. Peacock, "Space science applications of cryogenic detectors," in *Advanced Transition Radiation Detectors for accelerator and space applications*, Bari, Italy, 2003.

[8] N. Rando, "Cryogenics in Space," in *Observing Photons in Space*, New York, NY, Springer, 2013, pp. ISSI Scientific Report Series, vol 9.

[9] J. Baselmans, J. Bueno, S. J. C. Yates, O. Yurdoseven, N. Llombart, K. Karatsu, A. M. Baryshev, L. Ferrari, A. Endo, D. J. Thoen, P. J. de Visser, R. M. J. Janssen, P. Hargrave and M. Griffin, "A kilo-pixel imaging system for future space based far-infrared observatories using microwave kinetic inductance detectors," *Astronomy & Astrophysics,* vol. 601, no. A89, 2017.

[10] P. M. Echternach, B. J. Pepper, T. Reck and C. M. Bradford, "Single photon detection of 1.5 THz radiation with the quantum capacitance detector," *Nature Astronomy,* no. 2, pp. 90-97, 2018.

[11] Figueroa Group, "The Ideal Microcalorimeter," Experimental Cosmology and Astrophysics Laboratory, MIT, 2014. [Online]. Available: http://web.mit.edu/figueroagroup/ucal/ucal_basics/index.html. [Accessed 20 3 2020].

[12] D. McCammon, "Thermal Equilibrium Calorimeters -- An introduction," in *Cryogenic Particle Detection*, vol. 99, Berlin, Springer, 2005.

[13] L. Duband, J. Duval, N. Luchier and T. Prouve, "SPICA sub-Kelvin cryogenic chains," *Cryogenics,* vol. 52, pp. 145-151, 2012.

[14] NASA, "2020 NASA Technology Taxonomy," 2020. [Online]. Available: https://www.nasa.gov/sites/default/files/atoms/files/2020_nasa_technology_taxonomy.pdf. [Accessed 20 March 2020].

[15] C. E. Group, "Cryocoolers for space applications," University of Oxford, [Online]. Available: http://www2.eng.ox.ac.uk/cryogenics/research/cryocoolers-for-space-applications. [Accessed 20 March 2020].

[16] A. E. Jahromi, "Development of a Proof of Concept Low Temperature Superfluid Magnetic Pump with Applications," PhD dissertation at University of Wisconsin-Madison, 2015.

[17] T. Tirolien, P. Camus, G. Vermeulen, A. Volpe, S. Triqueneauz, A. Benoit, J. Butterworth and S. d'Escrivan, "Status of the Closed-Cycle Dilution Refrigerator Development for Space Astrophysics," *Journal of Low Temperature Physics,* vol. 176, pp. 5-6, 2013.

[18] M. Sauvage, K. Okumura, U. Klaas, T. Muller, A. Moor, A. Poglitsch, H. Feuchtgruber and L. Duband, "Operations and performance of the PACS instrument 3He sorption cooler on board of the Herschel space observatory," *Exp Astron,* vol. 37, pp. 397-431, 2014.

[19] L. Duband, L. Clerc, E. Ercolani, L. Guillemet and R. Vallcorba, "Herschel flight models sorption coolers," *Cryogenics,* vol. 48, pp. 95-105, 2008.

[20] C. Day, "Basics and Applications of Cryopumps," *CAS - CERN Accelerator School : Vacuum in Accelerators,* pp. 241-274, 2007.

[21] Cryogenics and Fluids Branch, "Introduction to Liquid Helium," NASA Goddard Space Flight Center, 11 9 2014. [Online]. Available: https://cryo.gsfc.nasa.gov/introduction/liquid_helium.html. [Accessed 13 8 2020].

[22] P. Wolfle and D. Vollhardt, The Superfluid Phases of Helium 3, Mineola, New York: Dover Publications, Inc., 1990.

[23] S. V. Sciver, Helium Cryogenics, New York, NY: Springer, 2012.

[24] D. Papoular, G. Ferrari, L. P. Pitaevskii and S. Stringari, "Increasing Quantum Degeneracy by Heating a Superfluid," *Physical Review Letters,* vol. 109, 2012.

[25] G. Chaudhry, "Thermodynamic properties of liquid 3He-4He mixtures between 0.15 K and 1.8 K," PhD dissertation at Massachusetts Institute of Technology, 2009.

[26] R. Radebaugh, "Thermodynamic properties of 3He-4He solutions with applications to the 3He-4He dilution refrigerator," NBS Tech note 362:19, 1967.

[27] R. de Bruyn Ouboter, K. W. Taconis, C. le Pair and J. M. Beenakker, "Thermodynamic properties of liquid 3He-4He mixtures derived from specific heat measurements between 0.4K and 2K over the complete concentration range," *Physica,* vol. 26, pp. 853-888, 1960.

[28] T. Alvesalo, P. Bergland, S. Islander, G. Pickett and W. Zimmermann Jr., "Specific Heat of Liquid He3/He4 Mictures near the Junction of teh lambda and Phase-Separation Curves. I," *Physical Review A,* vol. 4, pp. 2354-2368, 1971.

[29] V. K. Pecharsky and K. A. Gschneider Jr., "Magnetocaloric effect and magnetic refrigeration," *Journal of Magnetism and Magnetic Materials,* vol. 200, pp. 44-56, 1999.

[30] P. Wikus, E. Canavan, S. T. Heine, K. Matsumoto and T. Numazawa, "Magnetocaloric Materials and the Optimization of Cooling Power Density," *Cryogenics,* 2014.

[31] P. J. Shirron, "Applications of the Magnetocaloric Effect in Single-Stage, Multi-Stage and Continuous Adiabatic Demagnetization Refrigerators".

[32] P. Schiffer, A. P. Ramirez, D. A. Huse and A. Valentino, "Investigation of the Field Induced Antiferromagnetic Phase Transition in the Frustrated Magnet: Gadolinium Gallium Garnet," *Physical Review Letters,* vol. 73, no. 18, pp. 2500-2503, 1994.

[33] C. A. Beevers and H. Lipson, "The crystal structure of the alums," *Proceedings of the Royal Society A: Mathematical, Physical and Engineering Sciences,* vol. 148, pp. 664-80, 1935.

[34] D. B. Cole, X. Wang, L. Qin, N. J. Planavsky and C. T. Reinhard, "Chromium Isotopes," *White W.M. (eds) Encyclopedia of Geochemistry. Encyclopedia of Earth Sciences Series. Springer, Cham.,* 2018.

[35] M. Macariou, "What are Atomic Orbitals?," 9 2 2021. [Online]. Available: https://chemistrymadesimple.net/episode/4/.

[36] D. d. Klerk, "Adiabatic Demagnetization," in *Encyclopedia of Physics: Low Temperature Physics II*, Springer, 1956, pp. 38-209.

[37] J. M. Luttinger and K. C., "Crystalline stark splitting and microwave resonance absorption in paramagnetic salts," *Physical Review,* vol. 73, no. 2, pp. 162-72, 1948.

[38] G. Danilov, "ESR and ENDOR investigations of Cr3+ impurities in alpha, beta, and gamma alums," University of Ottowa, 1971.

[39] C. Hagmann, D. Benford and P. Richards, "Paramagnetic salt pill design for magnetic refrigerators used in space applications," *Cryogenics,* vol. 34, pp. 203-16, 1994.

[40] O. E. Vilches and J. C. Wheatley, "Techniques for using liquid helium at very low temperatures," *Review of Scientific Instruments,* vol. 88, pp. 570-2, 1952.

[41] A. Leclerc, "Determination and analysis of the 53Cr3+ fine and hyperfine structure parameters in hydrated crystals from electron sin resonance studies," University of Ottowa, 1977.

[42] C. Kittel, "On the gyromagnetic ratio and spectroscopic splitting factor of ferromagneticsubstances," *Physical Review,* vol. 76, pp. 743-8, 1949.

[43] A. Manoogian and A. G. Danilov, "Electron-nucledar double resonance of Cr3+53 in gallium alums II," *Physical Review B,* vol. 6, pp. 4103-11, 1972.

[44] B. Blearney, "Paramagnetic resonance spectra of five chromic sulphate alums at low temperatures," *Proceedings of the Royal Society of London. Series A. Mathematical and Physical Sciences,* vol. 204, no. 1077, pp. 203-16, 1950.

[45] R. P. Hudson, "Properties of the Cr+++ Ion in the Paramagnetic Alums at Low Temperatures," *Physical Review,* vol. 88, no. 3, pp. 570-572, 1952.

[46] L. J. F. Broer, *Physica,* vol. 9, p. 547, 1942.

[47] D. A. Shea and D. Morgan, "The Helium-3 Shortage: Supply, Demand, and Options for Congress," Congressional Research Service, 2010.

[48] A. Cho, "Helium-3 Shortage Could Put Freeze on Low-Temperature Research," *Science,* pp. 778-779, 2009.

[49] S. H. Harrison, M. W. Henley, K. Kuhlman, G. L. Kulcinski, J. F. Santarius and L. A. Taylor, "Lunar Helium-3 Fusion Resource Distribution," NASA Solar System Exploration, 2017.

[50] H. London, G. Clarke and E. Mendoza, "Osmotic Pressure of 3He in Liquid 4He, with Proposals for a Refrigerator to Work below 1 K," *Physical Review,* vol. 128, pp. 1992-2005, 1962.

[51] F. Miller and J. Brisson, "A simple method for the analysis of sub-Kelvin refrigerators that use a dilute superfluid 3He-4He mixture as a working fluid," *Cryogenics,* vol. 41, pp. 311-318, 2001.

[52] C. Ebner and D. Edwards, "The low temperature thermodynamic properties of superfluid solutions of 3He in 4He," *Physics Reports,* vol. 2, pp. 77-154, 1971.

[53] J. M. Baker and B. Bleaney, *Proceedings of the International Conference on Low Temperature Physics,* 1955.

[54] C. M. O'Brien, "Antiferromagnetic state in the chrome alums," *Physical Review,* vol. 104, no. 6, pp. 1573-9, 1956.